Photo-induced electron transfer reactions in liquid crystals

Photo-induced electron transfer reactions in liquid crystals

A dissertation

by

Pakorn Pasitsuparoad

Supervisor
dr hab. Gonzalo Angulo, prof. IChF PAN

International Doctoral Studies
Institute of Physical Chemistry
Polish Academy of Sciences
ul. Kasprzaka 44/52, 01-224, Warsaw, Poland

Warsaw, July 2020

Abstract

This work aims to describe anisotropy effects on chemical reactions imposed by the structure of liquid crystals. Photo-induced electron transfer reactions of two kinds, namely intramolecular and intermolecular electron transfers, are studied in order to observe the influence of the medium with and without material diffusion. The first kind is studied using a donor covalently linked to an acceptor molecule in many solvents. Two elementary models, based on the Generalized Smoluchowski equation and on the Generalized Langevin equation are applied to explain the time evolution of the fluorescence emission during the adiabatic charge transfer. Once well characterized an attempt to study the same system in liquid crystals is performed. On the other hand, the intermolecular electron transfer reactions are studied using the florescence quenching in the excited state. The charge shift and charge separation reactions are investigated in two different chemical systems. The second reaction has molecules resembling the moieties in the intramolecular electron transfer study. Steady state and time resolved measurements are performed to track the reaction kinetics. The reactions are first conducted in isotropic media at different temperatures and viscosities to extract the electron transfer parameters which are independent of the solvent. A set of diffusion-reaction models with different levels of anisotropy has been developed as well as a numerical method to solve the corresponding partial differential equations. Only the model which introduces anisotropic diffusion and reactivity gives physically meaningful values for all parameters entering the reactivity. It is therefore shown how to adapt reaction-diffusion models able to accommodate any sort of reactivity to complex environments.

Streszczenie

Celem niniejszej pracy jest przedstawienie wpływu anizotropii, wynikającej ze struktury ciekłych kryształów, na reakcje chemiczne. Zbadane zostały fotoindukowane reakcje przeniesienia elektronów, wewnątrzcząsteczkowe i międzycząsteczkowe, w celu określenia wpływu na nie dwóch rodzajów ośrodków, z i bez dyfuzji materiału. Reakcje wewnątrzcząsteczkowe były badane w wielu rozpuszczalnikach przy użyciu dawcy kowalencyjnie związanego z cząsteczką akceptora. W celu wyjaśnienia zmiany czasu emisji fluorescencji podczas adiabatycznego przeniesienia ładunku zastosowano dwa podstawowe modele bazujące na uogólnionym równaniu Smoluchowskiego i uogólnionym równaniu Langevina. Po dokładnym scharakteryzowaniu tych reakcji podjęto próbę zbadania podobnego systemu reakcji w ciekłych kryształach. Międzycząsteczkowe reakcje przeniesienia elektronów zostały natomiast badane za pomocą wygaszania fluorescencji w stanie wzbudzonym. Reakcje przesunięcia ładunku i separacji ładunku zostały zbadane w dwóch różnych układach chemicznych. Druga z tych reakcji dotyczy cząsteczek przypominających grupy z badania wewnątrzcząsteczkowego przeniesienia elektronów. W celu śledzenia kinetyki reakcji przeprowadzono pomiary czasowo-rozdzielcze oraz pomiary stanu ustalonego. Reakcje zostały najpierw przeprowadzone w środowiskach izotropowych charakteryzujących się rożnymi lepkościami oraz w różnych temperaturach, aby wyodrębnić parametry przenoszenia elektronów, które są niezależne od użytego rozpuszczalnika. Opracowano ponadto zestaw modeli reakcji-dyfuzji o różnych poziomach anizotropii, oraz metodę numeryczną w celu rozwiązania odpowiednich równań różniczkowych cząstkowych. Jedynie model, który wprowadzał anizotropową dyfuzję i reaktywność, pozwolił na otrzymanie wartości, o znaczeniu fizycznym, dla wszystkich parametrów wchodzących w zakres reaktywności. W związku z tym pokazano, w jaki sposób dostosować modele reakcji-dyfuzji, tak aby mogły być one zastosowane do dowolnego rodzaju reaktywności w złożonych środowiskach.

Acknowledgments

First of all, I would like to express my gratitude to my advisor prof. dr hab. Gonzalo Angulo for the continuous support of my study and related research, for his patience, motivation, and immense knowledge. His guidance helped me to carry on and to accomplish this study. Through it I have learned and acquired much essential knowledge and skills in science.

It was my pleasure and honor to work with prof. Alejandro Cuetos, dr Alessandro Patti and dr Arnulf Rosspeinter. I really appreciate their help, comments and advice. Their skills and insight have improved this work dramatically as well as my understanding in this study.

Moreover, I would like to thank the colleagues from the Laser Center and Fluence who always take care of the optical set-up problems namely, prof. Czesław Radzewicz, dr Tomasz Kardaś, dr Michał Nejbauer, dr Marcin Pastorczak, dr Paweł Wnuk, dr Piotr Skibiński and dr hab. Yuriy Stepanenko.

My gratitude also goes to dr Joanna Piechowska for the synthesis of PeDMA in this work. Her support on organic chemistry is charming and skillful.

My sincere thanks also goes to the members of the Photochemistry and Spectroscopy Department for supporting in the measurements and sharing constructive comments.
Another gratitude also goes to prof. William E. Schiesser for sharing the MATLAB code. The MATLAB codes for MOL calculations were inspired and developed based on his codes about the diffusion problems.

The author would like to thank LAMMPS and LAMMPS community. LAMMPS is an open software and very powerful. There are many packages and works done using LAMMPS. More information, please visit to url: `http://lammps.sandia.gov`.

My sincere thanks also goes to dr Agnieszka Wiśniewska for the measurements of temperature dependent viscosity and absorption. The measurements of POM were accommodated by dr inż. Andrzej Żywociński. I would like to thank dr Katarzyna Krupa for her valuable knowledge of Polish language.

Last but not the least, I would like to thank my family: my mother, sister and wonderful girlfriend for supporting me spiritually throughout this study.

This work was supported by the National Science Centre within the SONATA-BIS Grants 2013/10/E/ST4/00534.

Part of this work was supported by Center for the Computational Science at Interdisciplinary Center for Mathematical and Computational Modeling, University of Warsaw within the G72-17 computational grant.

Part of this work was also supported by Erasmus Plus Programme of the European Union.

List of Abbreviations

ΔG	Standard Gibbs energy of the electron transfer reaction
$E(D^+/D)$	Oxidation potential of a donor which is the quencher
$E(A/A^-)$	Reduction potential of a acceptor which is the fluorophore
E_{00}	Zero vibronic transition energy between the ground state and the excited state
V_σ	Coupling matrix element for distance dependence reactivity
w	Electron transfer reactivity
S	Huang-Rhys factor from the Displaced Harmonic Oscillator model, $S = \lambda_q/\hbar\omega$ where λ_{qm} and ω are the reorganization energy and frequency of the quantum mode, respectively.
$\tau_L(T)$	Solvent relaxation time
F	Faraday constant
e	Electron charge
T	Temperature in Kelvin
n_D	Refractive index of a given solvent
ϵ	Dielectric constant of a given solvent
η	Viscosity of a given solvent
σ	Contact distance
λ_s	Reorganization energy, it consists of inner-shell and outer-shell reorganization energy, λ_i and λ_o
k_B	Boltmann constant
N_A	Avogado number, 6.02x10^{23} mol^{-1}
MW	Molecular weight in g mol^{-1}
PeDMA	3-(p-N,N-dimethylaminophenyl)perylene
Pe	Perylene from SigmaAldrich, 99.5%, CAS 198-55-0, MW 252.31 g/mol

DMpT	Dimethyl-p-toluidine from AlfaAesar, 99.0%, CAS 99-97-8, MW 135.21 g/mol
R6G	Rhodamine 6G chloride from Lamdachrome, laser grade, CAS 989-38-8, MW 479.02 g/mol
DMSO	Dimethylsulfoxide from AlfaAesar, HPLC grade, CAS 67-68-5, MW 78.13 g/mol
Gly	Glycerol from AlfaAesar, HPLC grade, CAS 56-81-5, MW 92.09 g/mol
DG	Dimethylsulfoxide and Glycerol mixture
x_1 or x_2	Molar fraction of glycerol or DMSO in DG mixtures, respectively x1 = 0 is for pure DMSO
5CB	4-Cyano-4'-pentyloxybiphenyl from TCI, 98.0%, CAS 40817-08-1, MW 249.36 g/mol
MBBA	N-(p-methoxybenzylidene)-p'-n-butylaniline
DNS	3,5-Dinitrosalicylic acid from SigmaAldrich, 98.0%, CAS 609-99-4, MW 228.116 g/mol
KOH	potassium hydroxide from SigmaAldrich, 98.0%, CAS 1310-58-3, MW 56.11 g/mol
nHx	normal hexane from SigmaAldrich, 99.9%, CAS 109-99-9
THF	Tetrahydrofuran from SigmaAldrich, 99.0%, CAS 110-54-3
Abs.	Absorption measurement
Ex.	Excitation measurement
Em.	Emission measurement
λ	Wavelength in nm
Pol.	Polarization state
A	Integrated absorbance from a specific band in a spectrum
BBOT	2,5-bis(5-tert-butyl-2benzoxazolyl)-thiophene from Lambdachrome, laser grade, CAS 7128-64-5, MW 430.56 g/mol
C6H	2,3,5,6-1H,4H-Tetrahydroquinolizino-[9,9a,1-gh]coumarin from Lambdachrome, laser grade, CAS 58336-35-9, MW 241.29 g/mol
C153	2,3,6,7-Tetrahydro-9-(trifluoromethyl)-1H,5H,11H-[1]benzopyrano[6,7,8-ij]quinolizin-11-one from SigmaAldrich, 99%, CAS 53518-18-6, MW 309.28 g/mol

DCM	4-dicyanomethylene-2-methyl-6-(p-dimethylaminostyryl)-4-Hpyran from Lambdachrome, laser grade, CAS 51325-91-8, MW 303.36 g/mol
D_0	Bulk diffusion coefficient
D_ρ	Diffusion coefficient parallel to the director of liquid crystals in nematic phase
D_z	Diffusion coefficient perpendicular to the director of liquid crystals in nematic phase
v_x and v_{xx}	First and second derivatives of the potentail with respect to variable x, index consists of r and θ.
n_x and n_x	First and second derivatives of the population density with respect to variable x, index x consists of t, ρ, z, r and θ.
$\Delta\theta$	Step size in θ
ΔL	Step size in r for the decadian logarithmic space
w_0	Reactivity at contact
L	Decay length of the coupling matrix element
$k(t)$	Time dependence reaction rate coefficient
$\kappa(t)$	Time integrated reaction rate coefficient from 0 to time t, $\kappa(t) = \int_0^t k(t')dt'$
N_r	Number of points in r domain
N_θ	Number of points in θ domain
m_{1k}	Band center of a given spectrum, the index k consists of A, X and F and stands for absorption, excitation and fluorescence measurements, respectively. It is calculated from first moment of the spectral shape.
$\sqrt{m_{2k}}$	Band width of a given spectrum, the index k consists of A, X and F and stands for absorption, excitation and fluorescence measurements, respectively. It is calculated from second moment of the spectral shape.
S	Order parameter
P_2	The second order of Legendre polynomial
A_i and τ_i	Amplitudes and lifetimes obtained multiexponential fitting for fluorescence decay curves
ϕ	Quantum yield of fluorescence
ISA	Industry Standard Architecture

TCSPC	Time Correleated Single Photon Counting
IRF	Instrument Response Function
S- or P-polarization	S-polarization means a state perpendicular to the optical table and P-polarization means the opposite.
FOG	Fluorescence Optically gated technique
MSD	Mean Squared Displacement
E(t)	Collisions happen at a given time bin
N_0	Total collisions during the reaction time window
$N(t)$	Survival population at a given time bin
ICM	Interdisciplinary Center for Mathematical and Computational Modeling, University of Warsaw
OD	Optical Density
PET	Photo-induced electron transfer
DC field	Direct current electric field
WAT	Wojskowa Akademia Techniczna or Military University of Technology
DMA	N,N-dimethylaminophenyl
POPOP	1,4-Di[2-(5-phenyloxazolyl)]benzene
τ_0	Fluorescence lifetime of the dye without quencher
c	Quencher concentration in Molar
R_q	Quenching radius
$\frac{Em(c)}{Em(0)}$	Integrated area ratio of emission spectrum at quencher concentration c Molar divided by without quencher
$\frac{OD(c)}{OD(0)}$	Absorbance ratio at the excitation wavelength at quencher concentration c Molar divided by without quencher
pdepe	A solver function for one dimension parabolic and elliptic partial differential equations

Contents

Chapter 1

Introduction

The understanding about the chemical reactions in isotropic and homogeneous media like solid, liquid and gas phases is well established[1, 2, 3, 4, 5]. Although there have been some reports about chemical reactions in anisotropic media like argon matrices, micelles, cell membranes or even liquid crystals, LCs[6, 7, 8, 9, 10]. There are no detailed and systematic studies about the effect of the anisotropic environment on the kinetics of diffusion assisted bimolecular chemical reactions in general and specially in the latter. This is an important knowledge gap because many reactions of biological or technological interest take place in these or similar complex environments[11, 12, 13]. The thermotropic liquid crystal is a good candidate for modeling the anisotropic media because they show anisotropic and isotropic phases. Moreover, the molecular alignment of LCs can be controlled by means of temperature or electric fields. There were several efforts to use the anisotropy of LCs in applications including kinetics control of anisotropic reactions, optical devices, display devices, polymer synthesis or regiochemical controlled synthesis[14, 15, 16, 17, 18, 19, 20, 21, 10, 22, 23]. The idea to study chemical reactions in anisotropic media has been around for some time. However, to our knowledge only Wasielewski and co-workers have reported studies of intra-molecular electron transfer reactions in 4-Cyano-4'-pentyloxybiphenyl, 5CB[24, 25, 26]. The report discussed only the kinetics at short times and the coupling motions of LCs with charged species with the intention to develop photorefractive materials through doping of the LCs. This coupling interaction was also observed in the photophysical studies of the photophysics of neutral dyes in LCs[27, 28]. However, important questions about the effect of the medium anisotropy in chemical reactions assisted by diffusion in LCs still remain unexplored.

The selection of a chemical reaction to study the anisotropy effect is important. There are several logical choices for this study including electron transfer, proton transfer or energy transfer, all of them susceptible of being influenced by diffusion. The electron transfer is the best studied reaction in chemistry. The theories and experiments about the electron transfer have

been developed for several decades[29, 30]. Moreover, the electron transfer reaction can be investigated by means of light. Light is the fastest way to trigger the start of chemical kinetics. Therefore, the photo-induced electron transfers, PETs, have been widely employed to study kinetics. On the other hand, the study of bimolecular reactions in solutions is a challenging problem because many processes occur after the triggering like solvent and vibrational relaxation[31, 32, 33].

Regarding the role of diffusion in bimolecular reactions, over the years many theories based on the Smoluchowski approach [34] have been put forward [35, 36] which can be combined with electron transfer. For example, Wilemski and Fixman proposed a method to include distance-dependence for the reactivity, an essential characteristic of electron and energy transfer, into the Smoluchowski model[37].Since then, the theory has evolved to a degree of sophistication that allows for considering many different scenarios, like complex reaction schemes, reversibility or any kind of reactivity[38]. Nevertheless, in most cases the solvent is treated like an homogeneous and continuous isotropic environment. The microscopic pictures of the solvent properties have been introduced including the hydrodynamic effect and the solvent structure. The hydrodynamic effect is significant when the reactants approach as they start to feel each others influence on the surrounding solvent molecules[39, 40, 41]. This effect reduces the diffusion coefficient in the short range. In anisotropic media it is expected that the diffusion coefficient follows the viscosity tensor of the medium. Thus, as it has been shown in a number of occasions the diffusion coefficients in LCs must contain several components, specially in the smectic and nematic phases[42, 43, 44]. The solvent structure appears as a consequence of the molecularity of the solvent[45]. On the other hand, the solvent in the microscopic picture is no longer continuous and homogeneous. The solvent molecules are particles with volume. Therefore, a probability of finding another solvent molecule is a distance dependence function. This effect increases the chance of reactants to meet at the short distance. In anisotropic media this correlations between solvent molecules are no longer centrosymmetric, imposing a potential to the movement of reactants that depends on the angle of their approach. Both of these effects have not yet been taken into account in the theory of diffusion assisted reactions in LCs. In this thesis we make an adaptation to take them into account. Moreover, we have developed a numerical method for solving the partial differential equations associated to this problem. Electron transfer depends also on the properties of the solvent, specifically on its dielectric properties. LCs in the ordered phases also show anisotropy in its refractive index, dielectric constant and dielectric relaxation time[46, 47, 48]. We have included this effect through recent theoretical considerations[49, 50]. An alternative approach to explain the experimental findings is to perform molecular dynamics simulations of the reaction, without using reaction-diffusion models. We have implemented this in an open code software package (LAMPPS) with the idea to go from simple homoge-

neous solvents to LCs. Our attempts in this direction have been truncated by the enormous computational cost of the approach and the success of the reaction-diffusion model. We propose the conditions needed to perform these simulations reducing the time needed.

From an experimental point of view the difficulty about the study of bimolecular reactions in solutions lies in the time scales of the kinetics measurements. These reactions may occur over several timescales from few picosecond to several tens of nanoseconds. Therefore, a combination of fast time resolved techniques and stationary methods is required to describe the chemical reactions in solutions. In addition the theory to explain them needs to have a clear definition for the observable quantities: fluorescence intensities as a function of time and quencher concentration, in this case. In fact we profit from the measurement of the fluorescence of strong emitting dyes as it provides with large dynamic range and usually good signal to noise ratios. We will describe in detail the experimental methods followed in this work including sample preparation, setup calibrations, and data treatment with a special accent on the coherence between different experimental sources. Eventually, our focus is on explaining all measurements with the same theoretical models.

In order to vary the phase of the thermotropic liquid crystals one can try to change the temperature or using an electric field. In this thesis both methods have been implemented, although only the former has worked properly. In the latter case the stability of the chemicals was compromised. This seems to be a general problem in LCs[51, 52]. The different phases have been characterized by means of optical methods to asses the degree of order in them, and how the reactants, at least one of them, orients respect to this order imposed by the solvent.

The general strategy of the work relies on the knowledge of the electron transfer reactions studied in the LCs. We have studied two of these reactions, a charge shift and a charge separation reaction first in homogeneous isotropic solvents varying their viscosity and at the same temperatures as those used to change the LCs phases. Thus using the already established models we extract the electron transfer parameters to be used in the rationalization of the kinetics in the LCs.

An additional comparison experiment relates to unimolecular electron transfer reactions. As we have a covalently linked molecule formed of two moieties like the molecules used in the charge separation case, we try to observe the influence of the medium with and without material diffusion. Besides, most of the reported reactions in LCs are unimolecular, so this measurements also serve as a reference point[53, 25, 26]. As in the previous case, the study of this reaction requires additional experiments in usual solvents. The rationalization of these results lead us to apply the Generalized Smoluchowski equation and the Generalized Langevin equation because the reaction showed evidences of being controlled by the dielectric relaxation dynamics of the media. This is a consequence of a strong adiabaticity of this reaction, in contrast to the non-

adibatic electron transfer seen for the equivalent freely diffusing case.

This work is organized as follows. In the second chapter, the related theories about diffusion-reaction in condensed media, photo-induced electron transfer, liquid crystal structures and properties and electron transfer reaction-diffusion model adapted to LCs are explained in chapter 2. Then, the chemicals, experimental techniques and the setup calibrations are describe in chapter 3. The results obtained from the study of the unimolecular and bimolecular electron transfers are discussed in chapter 4. The conclusion of this study is in chapter 5. The numerical method mentioned above, the molecular dynamics simulation using LAMMPS and the problems of dyes under electric field are stated in Appendix.

Chapter 2

Theory

In this chapter, the basic kinetics of chemical reactions to explain the experimental findings are presented. The first and second sections describe the influence of diffusion in chemical reactions in isotropic solutions as well as the relationship between models and observables. The chemical reactions studied in this work are of electron transfer, therefore a short introduction to the electron transfer models is explained for bimolecular and unimolecular reactions. The electron transfer models describing the unimolecular reactions are based on two treatments including the generalized Langevin equation GLE and the generalized Smoluchowski equation GSE. Then the relation of the macrosocpic anisotropic properties and the molecular alignment in nematic liquid crystals is explained. Finally, a model to incorporate the anisotropic effect to the reaction-diffusion reactions and the electron transfer probability is explained.

2.1 Diffusion assisted reactions in solutions

The understanding about how diffusion affects chemical reactions in solution, has been developed for several decades. In 1918, Smoluchowski developed a model to rationalize coagulation in colloidal solutions[34]. The theory was based on the then recently discovered physics of Brownian motion[54, 55, 56]. The model developed by him, later renamed target model, is illustrated in fig. 2.1. In its application to chemical reactions, one of the two freely diffusing reactants is in a very large excess (like in photochemical experiments). The other one, is assumed to be immobile and is seen as a target of radius equal to the sum of the radii of both. Therefore, there is no interaction between different targets. Around this target the excess reactants move like independent point particles with a diffusion coefficient equal to the sum of those of both reactants. Moreover, the reaction is assumed to happen only at the contact and it is infinitely fast making disappear the point particles.

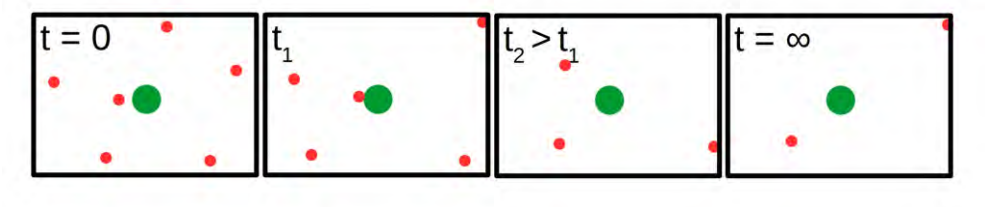

Figure 2.1: From the left to the right panels show the reactant distribution at the beginning t = 0, the reaction t and the steady state t = ∞; a green particle is the target and red particles are the diffusants.

A convenient way to represent the evolution of the reaction is to plot as a function of distance the normalized concentration of the diffusing particles with respect to the target $n(r,t)$. In fig. 2.2, this quantity is shown for the Smoluchowski model as presented above.

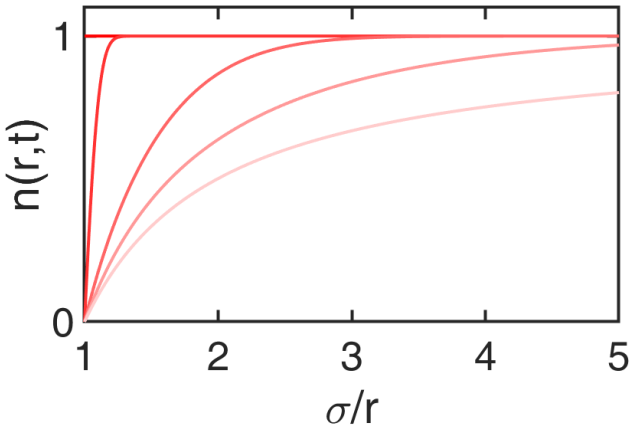

Figure 2.2: A pair correlation function according the Smoluchowski model; The correlation function at the beginning is one everywhere and it decreases with time until the steady state is reached.

The most important outcome of this theory is that the reaction rate constant is indeed a time dependent coefficient:

$$k(t) = 4\pi\sigma^2 D\left(1 + \frac{\sigma}{\sqrt{\pi D t}}\right) \tag{2.1}$$

which at long times becomes $k_\infty = 4\pi\sigma D$, where D is the mutual diffusion coefficient for the reactants and σ is the closest approach distance, equal to the sum of the radii of the two reactant species.

There are many assumptions in the Smoluchowski theory which are not realistic in describing chemical reactions in solutions. For example, the reactivity

is not necessarily infinite and may depend on the distance: both electron and energy transfer probabilities decrease with interparticle distance[57, 58]. The solvent is treated as a continuum, although its molecules are often not much smaller than the reactants. This introduces excluded volumes that restrict the movement of reactants[45, 59]. In addition, the diffusion of reactants is also affected by the hydrodynamic effect: when a particle moves in a solvent, it drags it and modifies the density around it, in such a way that when two of them approach they start feeling each other much before colliding[40]. As a consequence the mutual diffusion coefficient reduces with decreasing the inter-reactant distance.

These three effects can be introduced into the Smoluchowski model for the reactants pair distribution function through the modification of the diffusion operator and including a sink term in what now becomes a reaction-diffusion partial differential equation:[36, 60]

$$n_t = \hat{L}(r)n(r,t) - w(r)n(r,t) \tag{2.2}$$

where $w(r)$ is the reaction probability, which can take any form and $\hat{L}$ is the diffusion operator. For a centrosymmetric case this diffusion operator in three dimensional problems including the hydrodynamic effect and an interaction potential between the reactants reads

$$\hat{L}(r) = \frac{1}{r^2}\frac{\partial}{\partial r} r^2 D(r) e^{-V(r)/k_B T} \frac{\partial}{\partial r} e^{V(r)/k_B T} \tag{2.3}$$

where $D(r)$ is the distance dependent diffusion function proposed by Northrup and Hynes:[41]

$$D(r) = D_0 \left(1 - 0.5 \exp\left(- \frac{r-\sigma}{\sigma} \right) \right). \tag{2.4}$$

The bulk diffusion coefficient D_0 can be defined by the Zwanzig model to include dielectric friction felt by charged molecules:[61]

$$D_0 = \sum_i \left(\frac{k_B T}{\zeta_{v,i} + \zeta_{D,i}} \right) \tag{2.5}$$

where index i stands for the solute, $\zeta_{v,i}$ represents the hydrodynamic friction coefficient under slip boundary conditions:[62]

$$\zeta_{v,i} = 4\pi\eta r_i \tag{2.6}$$

and $\zeta_{D,i}$ represents the dielectric friction coefficient

$$\zeta_{D,i} = \frac{3}{4}\frac{z_i^2}{r_i^3}\frac{(\epsilon - n_D^2)}{\epsilon(1+2\epsilon)}\tau_D \tag{2.7}$$

where ϵ is the dielectric constant, n_D is the refractive index, η stands for the bulk dynamic solvent viscosity, r_i and z_i for the radius and charge of the diffusing molecule and τ_D is the Debye dielectric relaxation time of the solvent[63]. The dielectric friction vanishes for neutral diffusants. In addition, $V(r)$ is the interaction potential between the reactants. The potential associated to the solvent structure is defined as $V = -k_B T \ln(g)$ (from now on in this work for the sake of simplicity in the equations we will express the potential as $v = V/k_B T$). This potential can be measured in pure liquids and is proportional to the solvent structure g. The solvent structure is the probability of finding another solvent molecule at a given distance from a central one.

This partial differential equation needs auxiliary equations which are one initial condition and two boundary conditions to complete the problem. The initial condition is the reactants pair distribution function at start. Before the reaction is triggered, the reactants pair distribution function follows the interaction potential between the reactants and is given by

$$n(r,0) = e^{-v(r)}. \tag{2.8}$$

The inner boundary condition is reflective meaning that the flux across the boundary at the contact vanishes

$$4\pi\sigma^2 D(r)\left(\frac{\partial n(r,t)}{\partial r} + n(r,t)\frac{dv(r)}{dr}\right)\bigg|_{\sigma} = 0. \tag{2.9}$$

The outer boundary is set at infinite distance. Being one of the reactants in much lower concentration, it is assumed that there is an infinite source of diffusants. Therefore, this condition is:

$$n(\infty,t) = 1. \tag{2.10}$$

The solution of eq. (2.2) gives the reactants pair distribution function which depends on the distance and time. An integration of the reactivity multiplied by the population over the space gives the time dependent reaction rate coefficient as follows [36]

$$k(t) = 4\pi \int_{\sigma}^{\infty} w(r) n(r,t) r^2 dr. \tag{2.11}$$

This rate coefficient can be used to explain the population decay in the fluorescence quenching in solutions.

In our case, the fluorescence quenching in solutions is a bimolecular electron transfer reaction in the excited state. Once the fluorophore is excited, there are two pathways to release the energy – relaxing back to the ground state either emitting (radiative) or not (non-radiative) a photon or reacting with a quencher accepting or donating an electron. The emission is characterized by the sum of the radiative and non-radiative processes in absence of

quencher, $1/\tau_0$. The other deactivation channel, the one that opens in presence of quencher, by the rate coefficient $k(t)$.

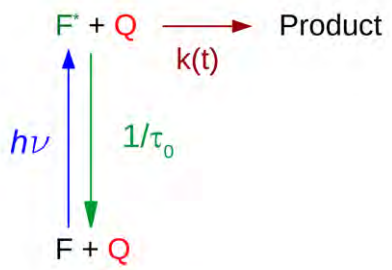

Scheme 2.1: Fluorescence decay processes in the presence of quenchers

The kinetic equation for the fluorophore concentration in the excited state in agreement with the scheme 2.1 is[36, 60]

$$\frac{d[F^*]}{dt} = \left(-\frac{1}{\tau_0} + [Q]k(t) \right)[F^*] \tag{2.12}$$

Assuming $[F^*] \ll [Q]$ it follows that $[Q]_0 = [Q]$, an integration of the above equation with the initial condition $[F^*] = [F^*]_0$ at $t = 0$ yields

$$[F^*](t) = [F^*]_0 \exp\left(-\frac{t}{\tau_0} - [Q] \int_0^t k(t')dt' \right). \tag{2.13}$$

The quencher concentration is replaced by c. The initial and time dependent fluorophore concentrations in the excited state is substituted by N_0 and $N(t, c)$, respectively. The equation 2.13 becomes

$$N(t, c) = N_0 \exp\left(-\frac{t}{\tau_0} - c \int_0^t k(t')dt' \right) \tag{2.14}$$

This is the kinetic equation for fluorescence quenching in solutions. The excited fluorophore population in eq. (2.14) can therefore be obtained from the reactant pair distribution function in 2.2. Therefore, the time resolved fluorescence measurements can be compared with the theory. The quantum yield is another observable which can be compared to the theory. This yield represents fraction of the excited state population that emitted light. For the fluorescence quenching study, the ratio of fluorescence quantum yield in presence and absence of quencher is given by the Stern-Volmer equation[64]

$$\frac{\int_0^\infty N(t, 0)dt}{\int_0^\infty N(t, c)dt} = \frac{\phi(0)}{\phi(c)} = 1 + \tau_0 c\kappa(c) \tag{2.15}$$

where $\kappa(c)$ is the concentration dependent Stern-Volmer rate constant and the $\frac{\phi(0)}{\phi(c)}$ can be obtained from steady state measurements of fluorescence, or by time integrating time resolved measurements encompassing the full kinetics.

2.2 Photo-induced electron transfer reactions

2.2.1 Non-adiabtic electron transfer

Non-adiabatic electron transfer can be viewed as just an electronic density redistribution either within a molecule (intramolecular electron transfer) or between two (intermolecular electron transfer). In order to link the thermodynamics of the reaction, which can be assessed by the electrochemical properties of the reacting system, with its kinetics an Arrhenius like theory is needed. More precisely, a connection between the activation energy (the energy of the transition state) and the free energy of the reaction is required. In order to do so a potential energy surface PES providing with the energy differences between the equilibrium states of the reactants and the products, and the metastable transition state has to be constructed. The first step in this task is to identify the reaction coordinate for electron transfer. It is tempting to identify it as the position of the electron, as if this is being transferred in a continuous way by shifting charge from one reacting center to another. However the reaction of our concern here is non-adiabatic. This means that the states admixture is negligible except in the transition state. In 1956, Marcus developed a model in which the reaction coordinate was identified as the polarization of the solvent, or more generally, of the low frequency harmonic modes of the solvent-reactants entity[65]. The fluctuations in this stochastic parameter, which depend chiefly on the orientation of the dipole molecules of the solvent, drive the reacting system to different energetic situations within its PES. Eventually the system reaches the transition state. At this point, and in agreement with the Born-Oppenheimer approximation, the electronic wavefunction may change in a time scale much shorter than the time scale of the nuclear configuration above mentioned. In other words, the electron can effectively jump from one of the reaction centers to the other, depending on the height of the barrier to be tunneled, which in turns is smaller the larger the coupling between the molecular orbitals of the reactants and the products as illustrated in the scheme 2.2. As a result the Marcus expression for the activation energy is:

$$\Delta G^{\ddagger} = \frac{\lambda}{4}\left(1 + \frac{\Delta G}{\lambda}\right)^2 \tag{2.16}$$

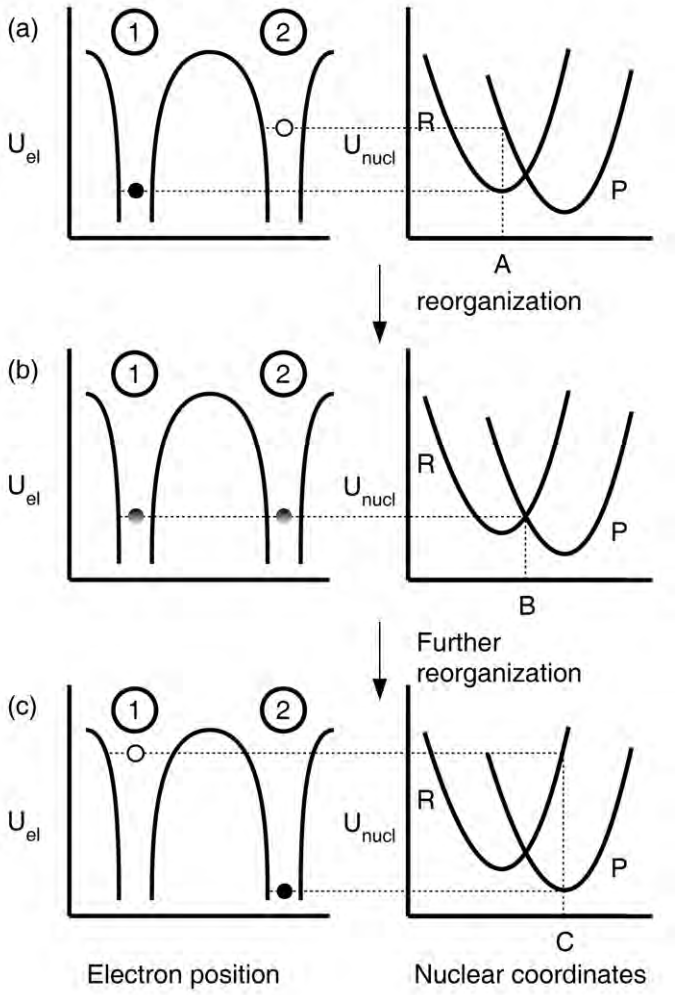

Scheme 2.2: (left column) Electronic potential energy curves and (right column) the corresponding nuclear potential energy curves. The electronic energies in the two wells are indicated on the left for three nuclear configurations A, B, and C for the reaction $red_1 + ox_2 \rightarrow ox_1 + red_2$. The levels in the wells are vertical ionization energies: the filled and open circles denote, respectively, ionization of the reduced state at its equilibrium nuclear configuration and the equilibrium configuration appropriate to oxidized state; the half-filled circles refer to ionization of the reduced state at the nuclear configuration appropriate to the intersection region. The level in well 1 is initially occupied in (a) and the level in well 2 in (c). The scheme is taken from Ref.[66]

where ΔG is the free enthalpy and λ is the reorganization energy. The free enthalpy is expressed in terms of the electrochemical potentials and the energy difference obtained from the zero vibronic transitions between the ground state and the first excited state (E_{00}, that can be obtained from the absorption and fluorescence spectra). The Weller equation[67] reads

$$\Delta G(r) = N_A e\big(E(D^+/D) - E(A/A^-)\big) - E_{00} - \frac{e^2}{2\pi\epsilon_0\sigma}\Big(\frac{1}{\epsilon_{ref}} - \frac{1}{\epsilon}\Big) + \frac{(z_c z_d - z_a z_b)e^2}{4\pi\epsilon_0\epsilon r} \tag{2.17}$$

where $E(D^+/D)$ is the oxidation potential for the donor, $E(A/A^-)$ is the reduction potential for the acceptor and $z_{a,b,c,d}$ are the charge of the reactants and products, respectively. The forth term accounts for the changes of solvent from the one in which the potentials were measured to the one in which the reaction takes place. The last term is the Coulombic interaction between the reactants and between the products. The reorganization energy comprises contributions from the internal changes in the structure of the reactants and the distance dependent solvent reorganization energy λ_s. In polar solvents, the former is usually negligible. The solvent reorganization energy accounts for nonequilibruim solvent polarization necessary to attain the transition state configuration. This separation of slow nuclear and fast electronic polarization of the electron mobility in polarizable media is characterized by the Pekar factor[68, 69]. Within the dielectric continuum models, the infinite response of the solvent polarization is approximated to be the square of the refractive index. If the size of the reactants is the same, the reorganization energy is given by

$$\lambda_s(r) = \frac{e^2}{4\pi\epsilon_0}\Big(\frac{1}{n_D^2} - \frac{1}{\epsilon}\Big)\Big(2 - \frac{\sigma}{r}\Big) \tag{2.18}$$

The equaiton 2.16 leads to a parabolic dependence of the logarithm of the rate constant with the free enthalpy. There are three important situations to be considered which are $\Delta G + \lambda > 0$, $\Delta G = \lambda$ and $\Delta G + \lambda < 0$. The first situation is called the normal region. The rate constant increases when the free enthalpy becomes more negative. The second situation is called the barrierless reaction as the activation energy becomes zero and corresponds to the largest rate constant. The third situation is at odds with the old chemical intuition dictating that the larger the spontaneity of the reaction, the fastest the reactions, and it corresponds to the Marcus inverted region.

As in the Marcus theory the coupling between reactants and products is small, the transmission coefficient for the crossing of the transition state can be expressed in terms of the Landau-Zener factor[70]. The probability of crossing is inversely proportional to the slope of the PES near the transition state. This means it is less likely for an electron crossing for a system at the steep PES because the system is more prone to continue in the same surface instead of jumping to the product's one. The expression was further developed by

many researchers to include the population of vibrationally excited product states and the finite dielectric response of the environment[71, 72]. The former effect is like summing up many channels of electron transfer corresponding to different vibrational states of the products. Therefore, as the vibrational quantum number changes, the Franck-Condon factor changes as well. The dielectric response of the solvent places a limit to the electron transfer because as seen before, the reaction is controlled by the solvent polarization. As it cannot be extremely fast, and it is loosely related to the rotational relaxation of the solvent, whenever the reaction becomes very fast the solvent movement becomes the bottleneck. The most comprehensive expression that remains tractable and contains relatively accessible quantities and parameters is[73]

$$w(r) = \sum_n \frac{1}{\tau_s} A_n \exp\left(- \frac{(\Delta G(r) + n\hbar\omega + \lambda_s(r))^2}{4k_B T \lambda_s(r)} \right) \tag{2.19}$$

$$\begin{aligned} A_n &= \begin{cases} \frac{(1-B_n)}{(2-B_n)}, & \text{normal region, } \Delta G + n\hbar\omega + \lambda_s > 0 \\ (1-B_n)B_n, & \text{inverted region, } \Delta G + n\hbar\omega + \lambda_s < 0 \end{cases} \\ B_n &= \exp\left(- \tau_s U(r) \exp(-S) S^n / n! \right) \end{aligned} \tag{2.20}$$

where $U(r)$ is defined as

$$U(r) = V_\sigma^2 \exp\left(- 2\frac{(r-\sigma)}{L} \right) \sqrt{\frac{\pi}{\hbar^2 k_B T \lambda_s(r)}}. \tag{2.21}$$

with the Huang-Rhys factor $S = \lambda_{qm}/\hbar\omega$, λ_{qm} and ω denoting the reorganization energy and frequency of the vibrational quantum mode linked to the reaction, respectively. L stands for the decay length of the coupling matrix element V_σ. The solvent relaxation time is expressed as:

$$\tau_s(r) = 4\tau_L \sqrt{\frac{\pi k_B T}{\lambda_s(r)}}. \tag{2.22}$$

where τ_L is the linear solvent relaxation time. It is related to the Debye relaxation time by $\tau_D = n_D^2/\epsilon$. For example, τ_L for the DMSO is 0.66 ps[74].

2.2.2 Adiabatic electron transfer

The previously mentioned electron transfer theory breaks down when the electronic coupling is large. Then the PESs are not the nonadiabatic states of the reactants and products. The electron transfer in this case is no longer a jump between different PESs. This situation is called adiabatic electron transfer. The nuclear and electronic coordinates are no longer separable. In order to describe the adiabatic electron transfer, a new reaction coordinate is needed. In

1940, Kramers proposed a model to explain the energy changes of the reacting system in the bottom of the PES coupling with movement over the barrier[75]. The movement in this model cannot directly be linked to a molecular translation or vibration but to a journey over different configurations of the reacting system with the surrounding medium[75]. This means the electronic distribution changes together with the surrounding polarization fluctuation. If we assume there is no other degree of freedom relevant or fast enough for the electron transfer such as solute translation or solvent translation, the polarization of the solute-solvent complex can be used for the reaction coordinate[70, 76]. In the Marcus theory for electron transfer reactions, these dynamical solvent effects were introduced through the dielectric relaxation time into the rate constant[70] or by considering the diffusion problem over the potential- or free-energy surface (PES, FES) with sudden jumps from the reactants' to the products' well.[77]. In the latter case, it is a dynamical theory based on the Smoluchowski diffusion operator for a one dimensional potential well. An alternative to theses models is to solve the time dependent Schrodinger equation in the presence of the solvent friction. The PES in this method is fully ab initio, therefore it costs long time to solve a specific case[78].

Most of the theories mentioned before try to obtain analytical solutions for the rate constant or at least a reaction-coordinate dependent rate coefficient[79]. One common idea of these theories is describing the reacting system under a potential shape with or without friction memory using the Generalized Langevin Equation GLE. On the other hand, the reaction rate coefficient can be described using a Generalized Smoluchowski Equation GSE, as the diffusion operator is time dependent. The GSE is a form of the generalized Fokker-Plank equation for a single coordinate diffusion problem under a harmonic potential[80]. One difference between GLE and GSE is the behavior of the reacting system at the short time. The response of dipole moment after light absorption is implusive not diffusive, as often observed from the experiments[81, 82, 83]. Within this difference, the short time kinetics is lost in the GSE case. Unfortunately, there are few studies in which the measured electron transfer dynamics are compared with the output from GLE simulations[84, 85, 86, 87].

The GLE consists of three main ingredients which are the PES, the friction felt by the reacting system and the fluctuation of the solute-solvent polarization. The last term is also called the noise term. This term is a function of a random variable. Therefore, a number of simulation trajectories is needed to obtain meaningful statistics. The motion equation can be formulated as

$$\ddot{z} = -\frac{1}{m_L}\frac{\partial V(z)}{\partial z} - \int_0^t \eta(t-\tau)\dot{z}d\tau + R(t) \tag{2.23}$$

where $\eta(t)$ denotes the friction term and $R(t)$ is the noise term. The random variable z can be normalized and takes the value 0 for the reactants' min-

imum and 1 for the products' minimum, in the potential energy surface V. The mass, m_L, is associated with the "heaviness" of the polarization of the medium and can be extracted from the rotational motion of the individual solvent molecules[88]. The integral term stands for the non-Markovian friction $\eta(t)$ against the movement of the system-associated particle. Be aware that in the present context, this friction is not purely mechanical but reflects the resistance of the dielectric to a change in the electric field associated with the charge redistribution in the solute, for example, those occurring during an electron transfer. This memory can be understood as an extended duration of the correlation function of the medium beyond the delta function response that characterizes pure Debye-solvents[63]. This friction has the same origin as the noise, which is the configuration fluctuation of the solute-solvent entity. Therefore, they are related through the second fluctuation-dissipation theorem[89]

$$\langle R(t)R(t+t')\rangle = \eta(t')\langle \dot{z}^2\rangle \tag{2.24}$$

To determine the PES in the excited state, one can use the quantum mechanical calculations. This is not an easy task. The PES in condensed phase has been shown to be equivalent to the FES[90]. A FES for a fluorescing system can be obtained from the study of the steady-state absorption and emission spectra in a variety of solvents. Thus having experimental data which can elucidate its shape is extremely advantageous. The friction, on the other hand, in the case of charge transfer reactions, is solely modulated by the solvent polarization and not by internal modes of the solute. It can be calculated from the dielectric relaxation spectrum of the solvent. Unfortunately, the THz dielectric spectroscopy is not available in this study. Another approach would be to somehow extract it from a reference measurement of a reaction for which the FES is well known assuming there are no additional components in the friction. This is for example the case of C153 for which it has been shown that a parabolic form for the FES reproduces nicely its emission behavior[88, 81]. As mentioned earlier, the GSE can also be tested for explaining these reactions. In this case a purely diffusive motion over the FES is considered with a $D(t)$ obtained from the same reference measurement of C153. The motion equation for GSE reads

$$\frac{\partial \rho(z,t)}{\partial t} = D(t)\frac{\partial}{\partial z}\left[\frac{\partial}{\partial z} + \frac{1}{k_B T}\frac{\partial}{\partial z}F(z)\right]\rho(z,t) \tag{2.25}$$

It describes the temporal behavior of the population distribution $\rho(z,t)$ along an arbitrary FES (or PES) $F(z)$.

The FESs are constructed using three diabatic states including (i) the electronic ground states $\mid g\rangle$, (ii) the locally electronically excited of the donor and acceptor pair $\mid l\rangle$ and (iii) the fully charge separated state of the donor cation and the acceptor anion $\mid c\rangle$. The matrix representation of the Hamiltonian $\mathbf{H}$ and the dipole moment matrix $\boldsymbol{\mu}$ in this diabatic basis are given as

follows[87, 91]

$$\mathbf{H}(\mu_s) = \begin{pmatrix} F_g(\mu_s) & 0 & J_{gc} \\ 0 & F_l(\mu_s) & J_{lc} \\ J_{cg} & J_{cl} & F_c(\mu_s) \end{pmatrix} \tag{2.26}$$

and

$$\boldsymbol{\mu} = \begin{pmatrix} \mu_g & \mu_{gl} & \mu_{gc} \\ \mu_{lg} & \mu_l & 0 \\ \mu_{cg} & 0 & \mu_c \end{pmatrix} \tag{2.27}$$

The $\mathbf{H}$ and $\boldsymbol{\mu}$ are assumed to be symmetric matrices and the diagonal elements, F_i in eq. (2.26), depend exclusively on the solvent polarization. Hence, the instantaneous effective dipole moment, μ_s, can be described within a continuum model for solvation following the work by van der Zwan and Hynes[92]

$$F_i(\mu_s) = U_i - \frac{B^{\mathrm{tot}}}{2}\mu_i^2 + \frac{B^{\mathrm{nuc}}}{2}(\mu_i - \mu_s)^2 + \delta_{0i}B_i^{\mathrm{el}}D. \tag{2.28}$$

This model accounts for the interaction of the permanent point dipole μ_i with polarizability α_i of state i placed in the center of a spherical cavity of radius a with a continuum dielectric environment, characterized entirely by its static and high frequency dielectric permittivities, ϵ and n_D^2, respectively. The first term on the right hand side of eq. (2.28) U_i accounts for the free energy of state i in the gas-phase, the second one for equilibrium solvation, and the third one for the non-equilibrium contribution to the free energy, due to orientational solvent relaxation. The fourth term accounts for the difference in the dispersion interactions between the solute and solvent between the excited states and the ground state[93]. The solvent response functions are given by[93, 92, 31]

$$\begin{aligned} B_i^y =& \frac{2}{a^3} \cdot \frac{f_x}{1 - 2(\alpha_i/a^3)f_x},\ f_x = \frac{x-1}{2x-1} \\ B_i^{nuc} =& B_i^{\mathrm{tot}} - B_i^{\mathrm{el}} \\ & (\mathrm{x} = \epsilon \rightarrow\ \mathrm{y} = \mathrm{tot}\ )\ \wedge\ (\ \mathrm{x} = n_D^2 \rightarrow\ \mathrm{y} = \mathrm{el}\ ) \end{aligned} \tag{2.29}$$

J_{ij} in eq. (2.26) denotes the electronic coupling elements between states i and j for all of which – in analogy to the treatment in Refs. [84] and [87] – are assumed to be equal.

Diagonalization of eq. (2.26) at each point along the solvation coordinate μ_s yields three adiabatic states, which we henceforth shall label as $\mid 0\rangle$, $\mid 1\rangle$ and $\mid 2\rangle$. Applying the same basis transformation to the dipole moment matrix yields the adiabatic permanent dipole moments (diagonal elements) and transition moments (off-diagonal elements). The construction of the FES from the experiments is discussed in chapter 4.

The $D(t)$ and $\eta(t)$ are assumed to be independent of the FES over which the solute evolves meaning independent of the nature of the solute and exclusively

a function of the solvent. The time dependent diffusion coefficient in the GSE can be obtained from the solvent relaxation dynamics $C(t)$ in a harmonic FES as follows:[88]

$$D(t) = -\frac{k_B T}{B^{\text{nuc}}} \frac{\dot{C}(t)}{C(t)} \tag{2.30}$$

Solving GSE in eq. (2.25) using the time dependent diffusion coefficient $D(t)$, one gets the time dependent excited state population distribution $\rho_1(z,t)$ which can be used to simulate the time resolved emission spectrum.

By using $C(t)$ measured from the experiments, the friction kernel $\eta(t)$ in the GLE can also be defined. According to Hynes[92], the solvent correlation function can be related to the properties of the stochastic variable for a pure harmonic potential well:

$$C(t) \approx \Delta(t) = \frac{\langle z(0)z(t)\rangle}{\langle z^2\rangle}. \tag{2.31}$$

The friction kernel in the time domain $\eta(t)$ is obtained using the Laplace transforming of the Langevin equation and fit the result in the time domain by the expression

$$\eta(t) = \omega_L^2 \gamma \delta(t) + \omega_L^2 \sum_i k_i \exp(-\lambda_i t). \tag{2.32}$$

This expression is suitable for deriving the set of equivalent ordinary differential equations ODEs in order to solve the GLE. The expression has two physical parameters which are ω_L and γ. ω_L is the frequency associated with the mass m_L. For chemical reactions, the particle which is moving over the potential energy surface is not mass, properly speaking. Rather it is related to the change of polarization of the environment, which enables the reaction. In other words, for an electron transfer reaction, the system is suffering energy fluctuations due to the thermal noise that provokes constant changes in the electric field of the medium. On the other hand, γ is the equivalent of the Debye linear solvent relaxation time. However, instead of taking this parameter from tables, as we are not dealing with Debye solvents, we adjust it in such a way that the obtained friction kernel reproduces the experimental solvent correlation function of C153. Finally, the values of ω_L, γ, $k_i s$ and λ_i are obtained and used to evaluate the GLE.

The evaluation of GLE is performed by splitting the GLE into a set o stochastic differential equations and then integrating the equations with time. The non Markovian process in the GLE is not explicitly present after the equation splitting. Each of the equations describes the Markovian evolution of

an auxiliary variable, driven by independent Guassian white noise,

$$\begin{aligned}\frac{dz(t)}{dt} =& v(t),\\ \frac{dv(t)}{dt} =& -\frac{1}{m_L}\frac{\partial F(z)}{z} - \omega_L^2\gamma v(t) + \sum_i w_i(t) + \omega_L^2\sqrt{\frac{\gamma k_B T}{\lambda_s}}\xi_0(t),\\ \frac{dw_i(t)}{dt} =& -\lambda_i w_i(t) - \omega_L^2 k_i v(t) + \omega_L^2\sqrt{\frac{\lambda_i k_i k_B T}{\lambda_s}}\xi_i(t).\end{aligned} \tag{2.33}$$

The variable $\xi_j(t)$, $j = 0 \ldots N$, denotes independent Gaussian noises with correlations

$$\begin{aligned}\langle \xi_j(t) \rangle =& 0,\\ \langle \xi_j(t)\xi_j(t+\tau) \rangle =& \delta(\tau)\end{aligned} \tag{2.34}$$

The number of auxiliary variables w_i corresponds to the number of exponential components in the friction kernel. The variables w_i have the dimension of "acceleration" of the z variable.

The initial condition for these equations is obtained from the fact that the system starts from an equilibrium Gaussian distribution. This is a projection of the population in the ground state onto the excited state. Under such conditions, the velocity is zero. The acceleration is equal to the derivative of the potential divided by the inertial mass of the solvent. Therefore, the sum of the initial vales for the other quantities ω_i is also zero. Moreover, the initial values of both at time zero are not compensated and equals to zero, $v(0) = 0$ and $\omega_i(0) = 0$. The initial distribution of the stochastic variable comes from the distribution of the system at rest in the ground state

$$\rho_1(z, 0) = \rho_0(z, eq) = N \exp\left(-\frac{F_0(z)}{k_B T}\right), \tag{2.35}$$

where N ensures area normalized population distributions.

In this work, eq. (2.33) is solved using the numerical integration scheme from Euler-Maruyama method together with the definitions of the initial conditions given above[94]. More detail for the equation derivations and parameter's values are to be found in the Ref. [95].

The results from the experiments and the simulations are compared using the spectral moments extracted from the time resolved spectra. The trajectories obtained from the simulations at different points at time zero are weighted taking into account the initial distribution in the excited state after excitation. Then the population evolution or histograms $\rho(\tilde{\nu}, t)$ are calculated. The time resolved emission spectra are simulated according to

$$I(\tilde{\nu}, t) \propto \tilde{\nu}^3 \int \rho_1(\tilde{\nu_0}, t)\mu_{10}^2(\tilde{\nu_0})L_f(\tilde{\nu} - \tilde{\nu_0})d\tilde{\nu_0} \tag{2.36}$$

where μ_{10} is the transition dipole moment of interest obtained from the calculation of the FES. The lineshape function L_f is a emission spectral lineshape of the reacting system in an apolar solvent in which no reaction is observed[96].

2.3 Liquid crystal structures and properties

Liquid crystals are materials which can flow like liquids and possess some anisotropic properties like solids. The molecules which can form an ordered structure between liquid and solid are called mesogens. The phases between liquid and solid are called mesophases[97]. Two types of liquid crystal mesophases must be differentiated namely thermotropic and lyotropic. If the phase transition appears as a result of changing the temperature, they are of the former kind, thermotropic. They are of interest for the basic researches as well as in display applications. The thermotropic mesogens are usually organic substances with molecular weights of 200 - 500 g mol^{-1} like cholesteryl nonate, MBBA or alkyl cyanobiphenyl. On the other hand lyotropic liquid crystals are concentration dependent phase transitions. The lyotropic mesogens are usually large and found in the biological environment. DNA, tobacco mosaic virus and synthetic polypeptides are examples of the lyotropic mesogens for water based solutions. According to the symmetry of the phases, Friedel[97] has proposed three mesophases namely nematic, smectic and cholesteric phases as shown in fig. 2.3. The direction of the principal axis in the arbitrary space is represented by the director, $\vec{n}$.

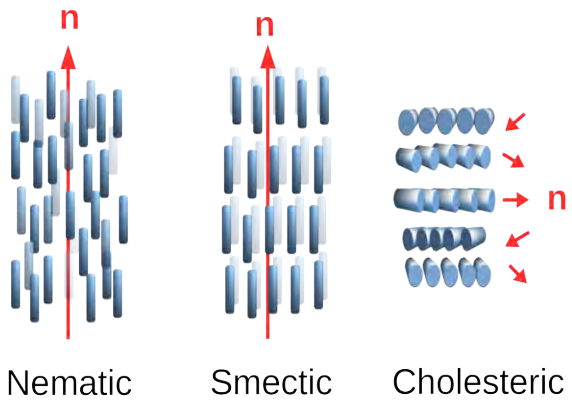

Figure 2.3: From left to right, the molecular alignment of nematic, smectic and cholesteric phases in liquid crystals

For the nematic phase, all molecules align in one direction which is parallel to the director. There is a cylindrical symmetry around the director. For

the smectic phase, the symmetry is higher than in the nematic phase. The molecules align in layers. This formation makes the liquid crystals in the smectic phase more viscous. The liquid crystals in the cholesteric is of interest for optical applications because the helicoidal structure induces periodic changes in the refractive index. On a local scale, the molecular formation is similar to the nematic phase. However, on a large scale the cholesteric director rotates as the layer number increases. The structure of a cholesteric liquid crystal is periodic with a specific spatial period.

Many experiments demonstrate that the anisotropy of nematics arises from the molecular alignment[46, 98, 99]. The thermotropic mesogens are usually dipolar molecules and treated as rod-like or spherocylindrical shapes[100, 101, 102]. Let us consider a Cartesian coordinate system with $\hat{n}$ representing the director of the nematic phase and $\hat{m}$ the molecular long axis vector. The orientation of the molecule can be described using the three Eulerian angles θ, ϕ, and ψ as shown in 2.3.

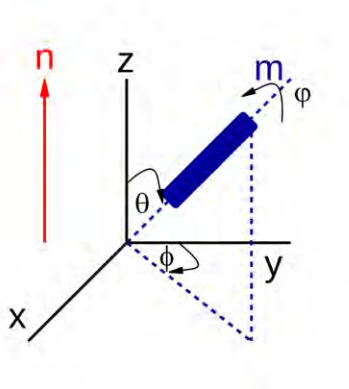

Scheme 2.3: The Euler angles required to describe the orientation of a molecule in a Cartesian coordinate

The angle ψ is the rotation around the molecular long axis and the angle ϕ is the rotation in the azimuthal direction. A simple way to characterize anisotropic media of this kind is the order parameter. It is a macroscopic quantity and as such an average over the whole population of solvent molecules. By tradition in the order-disorder problems, the unity defines the perfectly ordered phase and the zero defines the completely disorder phase. Then the components of a general tensor order parameter for a nematic LC are defined as[13]

$$S_{ij} = \frac{1}{2}\langle 3(\hat{m} \cdot \hat{i})(\hat{m} \cdot \hat{j}) - 1\rangle \tag{2.37}$$

where i and j are unit vectors. The three diagonal elements of the tensor are

given by

$$\begin{aligned} S_{xx} =& \frac{1}{2}\langle 3\sin^2\theta\cos^2\phi - 1\rangle \\ S_{yy} =& \frac{1}{2}\langle 3\sin^2\theta\sin^2\phi - 1\rangle \\ S_{zz} =& \frac{1}{2}\langle 3\cos^2\theta - 1\rangle \end{aligned} \tag{2.38}$$

The two components S_{xx} and S_{yy} vanish with the cylindrical symmetry around the z-axis as well as the off diagonal components. Hence, the order parameter in nematics results in

$$S = \frac{1}{2}\langle 3\cos^2\theta - 1\rangle \tag{2.39}$$

The orientation order of the LC molecules influences many physical properties including dielectric constant, refractive index, dielectric relaxation time and diffusion coefficient. The measured physical properties in nematics are characterized as the parallel and perpendicular values according to the symmetry. A variety of experimental methods can be used to obtain the order parameter. Let's take the self-diffusion coefficients as an example. Hess has developed a theory based on the highly ordered system of ellipsoids to a reference system of hard spheres, by affine transformation[103]. The principal results of the theory shows that the anisotropy of diffusion can be scaled with the imperfect orientational ordering ($S<1$). The ansiotropy diffusion relates to the order parameter S and the aspect ratio AR:[104]

$$\Delta \equiv \frac{D_\parallel - D_\perp}{D_\parallel + 2D_\perp} = S\left(\frac{AR^2 - 1}{AR^2 + 2}\right) \tag{2.40}$$

where AR is the ratio of the long to short axes of the LC molecules. The diffusion in this equation is the self-diffusion. For a guest-host system, the diffusion anisotropy is always lower. In addition, the averaged quantities or macroscopic properties in nematics are related to both components by

$$\langle\chi\rangle = \frac{\chi_\parallel - \chi_\perp}{\chi_\parallel + 2\chi_\perp} \tag{2.41}$$

where χ represents the physical properties of interest such as those mentioned above.

2.4 An electron transfer reaction-diffusion model for liquid crystals

In this section we show how to adapt the reaction diffusion equation show in section 2.1 and the electron transfer probability of section 2.2 to anisotropic

environments like nematic LCs. In the diffusion operator several modifications are necessary. In the electron transfer probability only the reorganization energy is modified in agreement with the angular dependent solvent molecular relaxation. Thanks to the cylindrical symmetry of the problem only two spatial dimensions are required.

2.4.1 Reaction-diffusion equation in anisotropic media

The anisotropic reaction-diffusion equation can written in terms of the asymmetric diffusion operator and the asymmetric potential. As we have seen in section 2.3 that there two perpendicular diffusion coefficients in nematics[105, 106]. According the cylindrical symmetry in nematics, D_ρ and D_z are assigned to $D_\perp$ and $D_\parallel$, respectively[107]. The operator in the cylindrical coordinate reads

$$\hat{L}(\rho,\phi,z) = \frac{D_\rho}{\rho}\frac{\partial}{\partial\rho} + D\rho\frac{\partial^2}{\partial\rho^2} + \frac{D_\rho}{\rho^2}\frac{\partial^2}{\partial\phi^2} + D_z\frac{\partial^2}{\partial z^2}. \tag{2.42}$$

The diffusion coefficient in this model follows eq. (2.5) with two viscosities depending on the direction, η_ρ and η_z. This simple operator is a good starting point for a programming check point. A MATLAB code and a numerical description are provided in section A.1.

This operator does not contain the effect of the potential. Additionally, in the target model the reacting molecules are considered spherical. Therefore, it is much simpler to consider the problem in spherical coordinates. A simple coordinates transformation for the diffusion coefficient tensor allows us to make this change. The potential of interaction can be easily written in any of the two coordinates systems, as we shall see later. We define the potential as $v = V/k_BT$ As in cylindrical coordinates, two variables of space are enough to fully describe the problem of nematics. The operator under these circumstances reads

$$\hat{L}(r,\theta) = \nabla\cdot\mathbf{D}\cdot(e^{-v}\nabla e^{v}) = \begin{pmatrix}\frac{\partial}{\partial r}\\ \frac{\partial}{\partial\theta}\end{pmatrix}\begin{pmatrix}D^A & D^B\\ D^B & D^A\end{pmatrix}\begin{pmatrix}\frac{\partial}{\partial r}+\frac{\partial v}{\partial r}\\ \frac{1}{r}\frac{\partial}{\partial\theta}+\frac{1}{r}\frac{\partial v}{\partial\theta}\end{pmatrix} \tag{2.43}$$

where D is the diffusion matrix. The coordinate transformation and variable definitions are given in table A.1. The two components of the diffusion matrix are defined as $D^A = D_\rho\sin^2\theta + D_z\cos^2\theta$ and $D^B = (D_\rho - D_z)\sin\theta\cos\theta$. The pair correlation function is now a function of the distance, angle and time, $n(r,\theta,t)$. In nematics, the potential associated to the solvent structure is also an angular dependent function $-\ln(g(r,\theta))$. A partial differential diffusion equation for an anisotropic diffusion problem under the anisotropic potential and reactivity is given by

$$n_t = \hat{L}(r,\theta)n(r,\theta,t) - w(r,\theta)n(r,\theta,t). \tag{2.44}$$

The initial condition is also modified as $n(r,\theta,0) = g(r,\theta)$. The reflective boundary at the contact is still valid. The equation for the flux density at a reflective contact is

$$\mathbf{D}\cdot\left(e^{-v}\nabla e^{v} n(r)\right)\Big|_{\sigma} = 0. \tag{2.45}$$

The outer boundary remains unchanged as $n(\infty,\theta,t) = 1$. The time dependent reaction rate coefficient for this problem is still a space integral as in the previous problem. The expression is

$$k(t) = 2\pi \int_{\sigma}^{\infty}\int_{-\frac{\pi}{2}}^{\frac{\pi}{2}} w(r,\theta) n(r,\theta,t) r^2 \sin\theta dr d\theta. \tag{2.46}$$

In order to solve this partial differential equation, we have used the Method of Lines[108] as described in section A.1 and section A.2. From $k(t)$ the observables defined above for the fluorophore population $N(t)$ and the quantum yield of emission can be obtained without further modifications.

2.4.2 Electron transfer probability in anisotropic media

Despite of the few experimental works on the intra-electron transfer reaction in liquid crsytal, none of them has considered the anisotropic effect on the reactivity[53, 25, 109, 110]. A series of theoretical works from Matyushov[49, 50] provide a solvation theory in these media. The theory treats the solute-solvent interaction potential given by the interaction of the solute charges with the solvent dipolar polarization. The solvation energy is then expressed through the polarization autocorrelation function of the pure solvent. The polarization autocorrelation function depends on the solvent rotation. The solvent reorganization energy in a continuum solvent response limit is given by[49]

$$\lambda(r,\theta) = \frac{1}{3}\lambda_{\parallel}(r) + \frac{2}{3}\lambda_{\perp}(r) + \lambda_A(r) \tag{2.47}$$

where the reorganization energy consists of the parallel, perpendicular and anisotropy components, $\lambda_{\parallel}$, $\lambda_{\perp}$ and λ_A, respectively. Each of the components is defined as

$$\begin{aligned}
\lambda_{\parallel,\perp}(r) &= \frac{e^2}{4\pi\epsilon_0}\left(\frac{1}{n^2_{D,\parallel,\perp}} - \frac{1}{\epsilon_{\parallel,\perp}}\right)\left(\frac{2}{\sigma} - \frac{1}{r}\right) \\
\lambda_A(r,\theta) &= \frac{e^2}{4\pi\epsilon_0}\left(\frac{1}{\epsilon_{\perp}} - \frac{1}{\epsilon_{\parallel}}\right) P_2(\cos\theta)\left(\frac{r^2-\sigma^2/2}{3r^3}\right).
\end{aligned} \tag{2.48}$$

where $P_2(\cos\theta)$ is the second order Legendre polynomial functions. This function is proportional to the molecular orientation distribution with the angle in the nematic phase. The ensemble average of this quantity is equivalent to the order parameter[13]. The $\lambda_A(r,\theta)$ vanishes in the isotropic phase because $P_2(\cos\theta) = 0$. Moreover, eq. (2.47) is reduced to eq. (2.18) which is the

standard reorganization energy for the Marcus equation. It is important to mention that this model concerns a charge separation reaction from a nonpolar state $D - A$ to a polar state $D^+ - A^-$.

A theoretical model for the charge shift electron transfer in nematics is not known. Recently, Matyushov has proposed a model explaining the electron transfer in nonpolar media[111]. The model indicates that the difference between the charge separation and the charge shift electron transfers lies in the induced reorganzation energy. The induced reorganization energy is quadratically proportional the solute charges. Therefore, a charge separation electron transfer like $D - A \rightarrow D^+ - A^-$ has higher reorganization energy than the charge shift electron transfer like $D - A^+ \rightarrow D^+ - A$. Therefore, we assume the reorganization energy for the charge separation and the charge shift electron transfer to relate by a multiplication factor.

It is true that the other electron transfer parameters could depend on the direction like the solvent relaxation time or the free enthalpy. In this work, we assume that the free enthalpy and the solvent relaxation time are angular independent because the only mode able to follow the reaction of the electron transfer is the fastest movement which is the translation along the molecular long axis of the solvent. The idea behind this assumption can be explained using fig. 2.4.

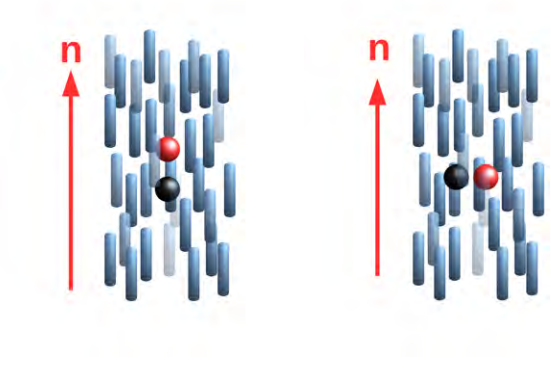

(**a**) (**b**)

Figure 2.4: Toy models representing a fluorophore (a red sphere) and a quencher (a black sphere) in nematogens (blue rods) (a) an electron transfer parallel to the director and (b) an electron transfer perpendicular to the director

For the electron transfer happening in the namatic phase, the only fast movement which can trigger the polarization fluctuation is the translation along the nematic director. The rotation parallel to the director does not produce

polarization changes. The other translations or rotations are not faster than the one mentioned before. There are two extreme situations to be considered for a pair of fluorophores and quenchers. In fig. 2.4a, the solvent polarization fluctuation affects along this solutes' axis. On the other hand, the second picture in fig. 2.4b gives the solvent fluctuation perpendicular to the solute axis. Therefore, according to this toy model, despite being only one relaxation time important in both situations, the effect of the solvent molecules movement is different energetically in each case, as the reaction electric field effect for the electron transfer is not the same. Thus the reorganization energy depend on the angle between the solute molecules axis and the nematic director.

Chapter 3

Experiments

The materials, experimental techniques, data treatments for steady state and time-resolved measurements are explained in this chapter. The first section describes the handling of fluorophores, quenchers and solvents. The second section describes the measurements, data handling and the equipment calibrations as well as sample characterizations.

3.1 Materials

3.1.1 Fluorophore and Quencher

3-(p-N,N-dimethylaminophenyl)perylene PeDMA was synthesized by dr Joanna Piechowska following the work reported by Banerji and co-workers [112]. Rhodamine 6G chloride R6G and Perylene Pe were used as received without further recrystallization. R6G was bought from Lamdachrome, laser grade, CAS 989-38-8. Pe was bought from SigmaAldrich, purity of 99.5%, CAS 198-55-0. Dimethyl-p-toluidine DMpT was used as a quencher without further purification from AlfaAesar, purity of 99.0%, CAS 99-97-8. The chemical structures of reactants are shown in fig. 3.1.

All these substances were selected because of several reasons – oxygen tolerance, short fluorescence lifetime, liquid crystal solubility and photophysical properties. The study of fluorescence quenching in solutions can be altered by the presence of additional and uncontrolled the oxygen quenching. This issue can be avoided by degassing the solutions or using the fluorophores which have short lifetimes, $\tau \leq 6$ ns. The lifetime shortening of R6G and Pe in ACN by the oxygen quenching were recorded. The lifetime reduction was less than 5%. Moreover, the fluorescence quantum yields are more than 0.9. The short lifetime and high quantum yield assure the feasibility of the excited state quenching and the fluorescence detection. The free enthaly of the electron transfer reactions is also important. These reactants were selected to show electron transfers in the normal region. The solubility of reactants in 5CB is also a major concern. For R6G and Pe the maximum attainable concen-

trations in 5CB are approximately 0.1 - 0.25 mM. These give the maximum absorbance about 0.15 - 0.23 in 0.1 mm path length. The liquid quencher was chosen because it is easier to prepare solutions in a controlled manner in 5CB. The highest quencher concentration is below 10% molar fraction of glycerol. Therefore, the nematic phase still exists at room temperature[113, 114]. The DG mixtures (vide infra) are transparent in the fluorophores and quenchers spectral windows, while 5CB has an absorption peak at 300 nm[115]. Moreover, samples in the nematic phase scatter light. The scattering effect increases with the sample thickness. Hence, the optical measurements were performed using the cells which have the path length of 0.1 mm.

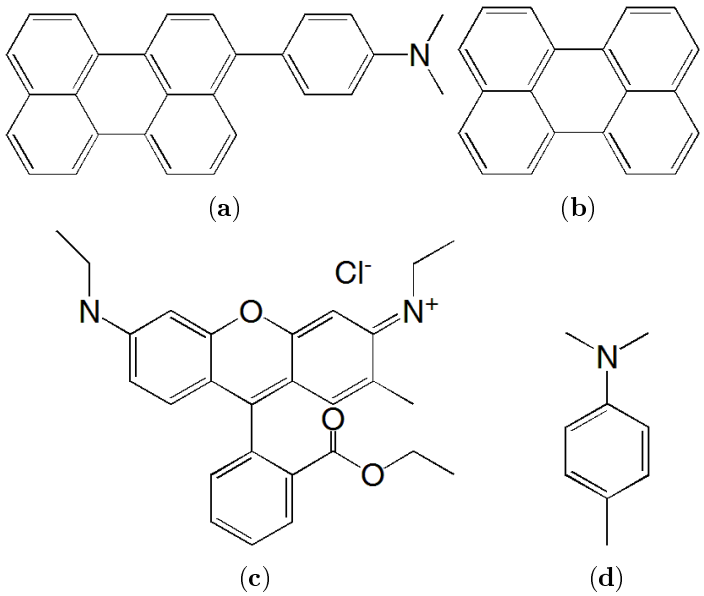

Figure 3.1: Molecular structures of (a) PeDMA, (b) Pe, (c) R6G and (d) DMpT

Table 3.1: Electrochemical potentials and photophysical properties of reactants

	R6G	Pe	DMpT
$E^{ox,red}$/V vs SCE	-0.9	-1.76	0.78
E_{00}/eV	2.21 - 2.24	2.78 - 2.81	
τ_0/ns	3.5 - 4.0	4.9 - 5.7	

The electrochemical and photophysical properties of reactants are summarized in 3.1 for electron transfer reactions. The electrochemical potentials of the reactants were measured in ACN at 20°C[116, 73]. R6G and Pe are electron acceptors which get reduced in presence of DMpT and light. The E_{00} values were estimated from absorption and emission spectra. The details of the E_{00} estimation are provided in section 3.2.4. The wide range of E_{00} listed

in table 3.1 is due to the different values obtained in DG mixtures and 5CB at temperatures between 293.15 K and 323.15 K. This difference is also manifested in the lifetimes. The lifetimes shown in table 3.1 are measured from the dyes without quenchers in DG mixtures and 5CB. Despite the original plans were to measure also in another LCs, 7CB and 8CB, the solubility of the dyes revealed to be too low to be practical.

3.1.2 Solvent properties

All solvents were used as received and purities are the highest available in the market. DMSO and glycerol were bought from AlfaAesar, HPLC grade. Both solvents were bottled under argon and tightly sealed. No smell could be detected from DMSO, which is indicative of the presence of sulfites degradation products.

The composition dependent and temperature dependent physical properties of the solvents including viscosity, refractive index, dielectric constant, density, solvent relaxation time and pair correlation function are described below. The viscosities of DG mixtures at different temperatures and molar fractions of glycerol were measured using Malvern Kinexus rotational rheometer[117]. The viscosity of DG mixtures was interpolated according to Nissan–Grunberg equation:[118]

$$\ln\left(\frac{\eta(x_1,T)}{\eta_0}\right) = x_1 \ln\left(\frac{\eta_1(T)}{\eta_0}\right) + x_2 \ln\left(\frac{\eta_2(T)}{\eta_0}\right) + x_1 x_2 a_1 \tag{3.1}$$

where a_1 is the coefficient given in table 3.2 to fit with the experimental data and $\eta_{1,2}(T)$ are the viscosity of the pure glycerol or DMSO at a given temperature, respectively. The η_0 is a reference quantity which is equal to 1 cP. The viscosities of pure solvents at different temperatures was taken from the literature[119, 120, 121]. For a pure solvent, the temperature dependent viscosity obeys the exponential function as following:

$$\ln\left(\eta_m(T)\right) = b_m T + c_m \tag{3.2}$$

where b_m and c_m are the coefficients obtained from the fitting to the literature[119, 120, 121]. The subscript 1 and 2 are for pure glycerol and DMSO, respectively. The coefficients are listed in table 3.2.

Table 3.2: Fitting parameters for macroscopic properties of DG mixtures

	a_1	a_2	b_1/K^{-1}	c_1	b_2/K^{-1}	c_2
η^*	-0.8532		-0.064	25.912	-0.013	4.565
$n_D^\dagger$	0.0084	-0.0015	-2.3730x10^{-4}	1.5432	-4.3551x10^{-4}	1.6607
$\epsilon^\dagger$	26.4	-22.4	0.17	93.85	-0.13	85.70
$\rho^\ddagger/\mathrm{g\ mL}^{-1}$	0.0235					

* This quantity is calculated using eq. (3.1) and eq. (3.2).
† This quantity is calculated using eq. (3.4) and eq. (3.3).
‡ This quantity is calculated using eq. (3.5).

The viscosities obtained from the experiments and eq. (3.1) are compared in fig. 3.2. The temperature dependent viscosity for DG mixtures is assumed to be correlated with the viscosities of the pure solvents. The coefficient was optimized to fit the experimental data.

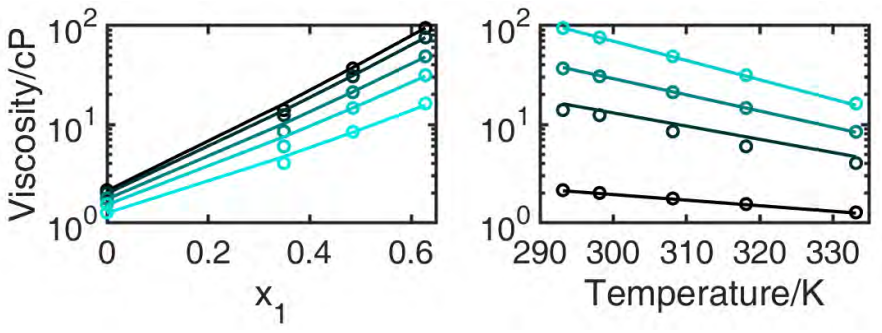

Figure 3.2: Viscosities of DG mixtures plots (left) as a function of glycerol molar fractions of glycerol and (right) temperatures obtained from (circle) the experiments and (line) the calculated data; the increasing temperature is from black to cyan colors in the left panel and the increasing glycerol molar fraction of glycerol is from black to cyan colors in the right panel.

For the refractive index and the dielectric constant, the assumption that the temperature dependent quantities can be evaluated from the pure solvent is applied. The refractive indices and dielectric constants of pure glycerol and DMSO from the experiments were taken from the literature[122, 123, 121, 124]. The temperature dependent of both quantities was correlated with linear functions $y_m(T)$ as following:

$$y_m(T) = b_m T + c_m \tag{3.3}$$

where y stands for the refractive index or dielectric constant and the m index stands for the pure glycerol as 1 or pure DMSO as 2. The b_1, c_1, b_2 and c_2 coefficients are the results from the linear fitting and given in table 3.2. Figure

3.3 shows the linear fittings of the pure solvents from the experiments and eq. (3.3) together with the regression parameter R^2.

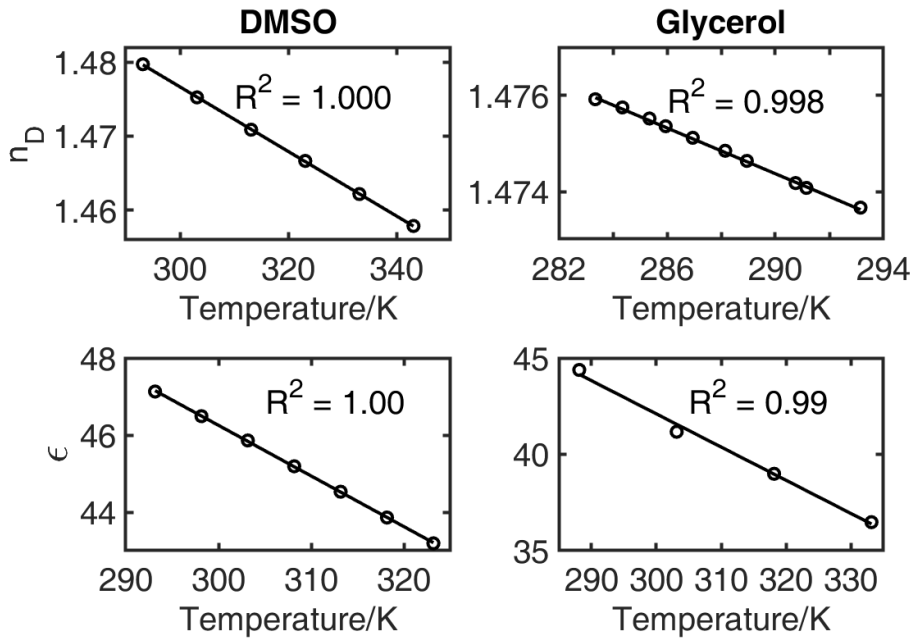

Figure 3.3: Refractive indices and dielectric constants of (left column) DMSO and (right column) glycerol obtained from the experiments marked as circles and eq. (3.3) marked as lines as a function of temperatures together with R^2 of the fitting

Knowing the temperature dependent functions of pure solvents, the refractive indices and dielectric constants for DG mixtures as a temperature function follow Kister–Redlich equation:[125]

$$y(x_1, T) = x_1 y_1(T) + x_2 y_2(T) + x_1 x_2 a_1 + x_1 x_2 a_2 (2x_1 - 1) \qquad (3.4)$$

where a_1 and a_2 were taken from a previous report of DG mixtures[74]. The assumption that the $n_D(x_1, T)$ or $\epsilon(x_1, T)$ of DG mixtures can be expressed in terms of the pure solvents and Kister–Redlich equation is well coherent with a recent work[126]. The plot of $n_D(x_1, T)$ and $\epsilon(x_1, T)$ are shown in fig. 3.4.

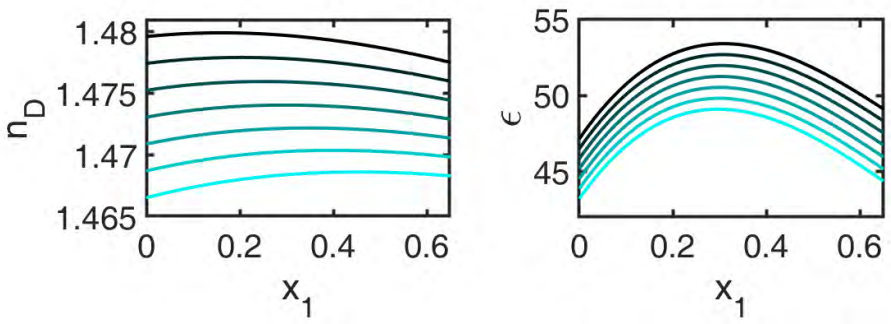

Figure 3.4: (Left) Refractive indices and (right) dielectric constants as a function of glycerol molar fraction obtained from the calcuation using eq. (3.4); the increasing temperature is from black to cyan colors.

The density ρ of DG mixtures is assumed to be invariant for this experimental temperature range because both densities are similar as well as the solvent diameters. Therefore, the Kister–Redlich equation can be reduced to be a function of molar fractions of glycerol as following:

$$\rho(x_1) = x_1\rho_1 + x_2\rho_2 + x_1x_2a_1 \tag{3.5}$$

where ρ_1 and ρ_2 are the densities of pure glycerol and DMSO which are 1.26 and 1.10 g mL^{-1} and the coefficient a_1 is given in table 3.2[74]. The solvent diameters of the pure glycerol and DMSO are similar which are 5.47 and 5.13 Å, respectively. The diameters of the DG mixture is also assumed to be independent of the temperature. The solvent diameter is approximated to be a linear combination of the molar fractions of glycerol. The formula is written as

$$\sigma_{solv.} = \sigma_1x_1 + \sigma_2x_2 \tag{3.6}$$

where σ_1 and σ_2 are the solvent diameters of glycerol and DMSO, respectively.

The pair correlation function $g(r)$ of the solvents is another important quantity. The function can be obtained from the Percus-Yevick approximation to the Ornstein–Zernike equation. The exact solution of the Percus–Yevick integral equation for hard spheres was first obtained in [127]. A MATLAB code to generate this function is taken from the chapter 8 in the book, Scattering of Electromagnetic Waves[128]. The code requires the solvent diameter $\sigma_{solv.}$ and the packing fraction as inputs. The packing fraction of a liquid is 0.4 - 0.5. The packing fraction of a liquid can be roughly estimated as $\frac{\rho}{MW}N_A\frac{\pi}{6}\sigma^3_{solv.}$. The packing fraction of the mixtures deviates less than 10% comparing to the pure DMSO. Moreover, a theoretical work of binary mixtures indicates a small difference of the packing fraction and $g(r)$ when the pure solvents have similar diameters and densities[129]. Figure 3.5 shows $g(r)$ for pure solvents obtained from the MATLAB code. The peaks and valleys of the generated curves are well in agreement with the x-ray and neutron scattering studies[130].

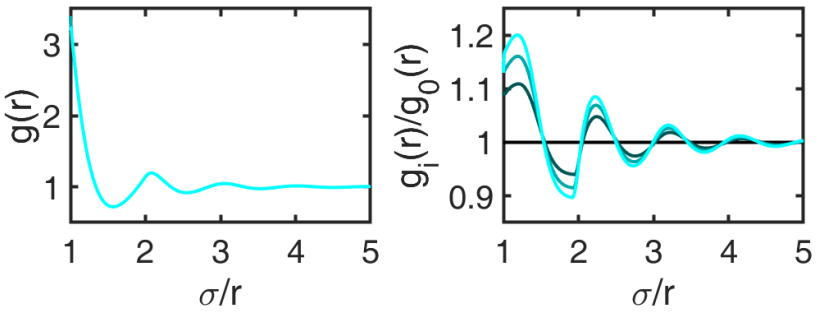

Figure 3.5: (left) The radial distribution function of DG mixtures; the data were calculated using the MATLAB code; the packing fraction is 0.4 and the solvent diameters are 5.13, 5.25, 5.31 and 5.35Å; (right) the ratio of $g(r)$ compared to the one obtained from the pure DMSO (black line); the increasing solvent diameter is from black to cyan colors.

The longitudinal dielectric relaxation time τ_L is another ingredient entering the electron transfer reactivity, eq. (2.19). This quantity is taken from a study of the C153 solvation dynamics in DG mixtures[74]. The results show a correlation of τ_L and η in the following form:

$$\tau_L = t_{l1} \ln\left(\frac{\eta}{\eta_0}\right) + t_{l2} \tag{3.7}$$

where t_{l1} and t_{l2} are the fitting parameters which equals to 0.552 and 0.603 ps, respectively. The reference viscosity η_0 is 1 cP. The fitting of the experiments with eq. (3.7) is shown in fig. 3.6 as well as the fitting quality.

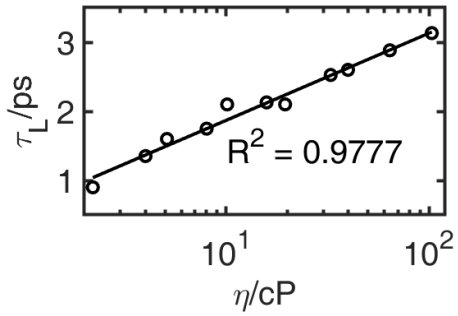

Figure 3.6: Dependence of τ_L from C153 in DG mixtures as a function of η (circle) measured from the fluorescence time resolved techniques[74] and (line) calculated from eq. (3.7)

4-Cyano-4'-pentyloxybiphenyl or 5CB was bought from TCI, purity 98.0%, CAS 40817-08-1. The compound was used without further purification. The as received compound color is white at room temperature and becomes clear

above 40°C. This is coherent with the specification from the supplier. The color is white because the color mainly comes from the light scattering. The nematic to isotropic transition temperature T_{NI} of the as received compound was measured using thermogravimetric analysis combined with differential scanning calorimeter model Calvet 111 from Setaram. The T_{NI} is 307.9 K, while the literature value is 308.2 K[98]. According to the transition temperature, it is reasonable to assume that the 5CB purchased is of high purity. Moreover, the absorption spectrum shows no sign of the impurity absorption in the range 300 - 800 nm[131, 132]. The physical properties of 5CB at different temperatures were collected from the literature[98, 46, 48] and listed in table 3.3.

Table 3.3: Density, refractive index, dielectric constant and viscosity of 5CB at different temperatures

Temperature/K	ρ/g mL^{-1}	n_D	ϵ	η/cP
293.15	1.0280	1.72/1.53	20.0/6.0	28/52
303.15	1.0175	1.70/1.54	17.1/7.5	20/30
313.15	1.0050	1.59	11.4	21.14
323.15	1.0003	1.58	11.4	14.33

Note: Properties in the nematic phase are represented as the parallel/perpendicular values.

In order to calculate the electron transfer reactivity in LCs, we need to know the solvent relaxation time τ_L and the pair correlation function $g(r, \theta)$ additionally to the above listed properties. It is not trivial to define the solvent relaxation time in LCs because dielectric spectroscopic measurements show multiple components over several time scales[133, 134, 135]. The relaxation times reported by several groups diverge from few picoseconds to few tens of nanoseconds depending on the techniques[109, 134, 136, 47]. In view of the lack of congruence in the reported values, the relaxation time in this study is set as a free parameter.

The pair correlation functions in liquid crystals can be obtained from the solution of the Ornstein–Zernike equation or the Monte Carlo simulations. Unfortunately, there is no analytical solution to the Ornstein–Zernike equation for the nematic liquid crystals. We performed the MC simulations in the NVT ensemble to obtain the correlation functions in the nematic and isotropic liquid crystals. The NVT ensemble is a canonical ensemble where the particle number, volume and temperature of the system are constant. In the simulations, the molecular shape of 5CB was modeled as hard prolate spherocylinders with elongation of 1.64 nm and diameter of 0.36 nm[137]. The cubic simulation box contains 2500 spherocylindrical particles N. The box size was adjusted to obtain the densities ρ in the nematic and isotropic phases, 1.01 g mL^{-1} at 293.15 K and 0.90 g mL^{-1} at 323.15 K, respectively. These values are in

agreement with the phase diagram calculated by Bolhuis and Frenkel for hard spherocylinder fluids[137].

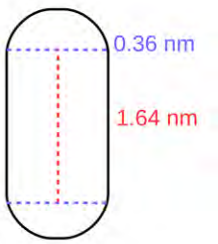

Figure 3.7: A spherocylinder model for MD simulation to generate the 5CB potential in the nematic and isotropic phases

As an initial configuration, the particles were seated parallel to each other in the hexagonal lattice. All of the lattice points were not fully occupied because it was adjusted to the given density. First, one million MC cycles were performed to equilibrate the system. Each MC cycle consisted of N attempted displacements of randomly chosen particles. The maximum displacement was adjusted to obtain an averaged acceptance of approximately 40%. During the equilibration, the nematic order parameter was monitored. The order parameter was calculated using a standard procedure of diagonalizating the order parameter tensor[138]. After the equilibration, the order parameter did not change out of the typical statistical fluctuations and the lattice was completely melted. The average order parameter in the nematic and isotropic phases were 0.736 ± 0.001 and 0.060 ± 0.001, respectively.

The evaluation of the pair correlation function $g(r, \theta)$ are performed using the equilibrated configuration. The simulation procedures follow the one in the equilibration step. One million MC cycles were employed to generate the statistical average pair correlation of the system. The pair correlation function is defined as

$$g(r,\theta) = \frac{1}{N\rho 2\pi r^2 \cos\theta} \left\langle \sum_{i}^{N} \sum_{j \neq i}^{N} \delta(r_{i,j} - r)\delta(\theta_{i,j} - \theta) \right\rangle \tag{3.8}$$

where $r_{i,j}$ and $\theta_{i,j}$ are the coordinates of the vector position from i to j in the spherical coordinates. In the simulation the Dirac delta function is replaced by unity in a small range of width $l/(2n_{hist})$ around r, with l being the size of the simulation box and n_{hist} being the number of divisions used in the histogram set to 200. $g(r, \theta)$ was evaluated and accumulated in an histogram with n_{hist} divisions during the simulation.

The potential surfaces obtained from the MC simulations in the nematic

and isotropic phases are shown in fig. 3.8. The potential surface in the nematic phase is clearly angular dependent. It shows short range correlation at $\theta = 90°$ or in the plane perpendicular to the director, while the long range correlation appears at $\theta = 0°$. On the other hand, the potential surface in the isotropic become more homogeneous. There is a small fraction of the short range and angular correlations. This remaining angular dependent in the isotropic phase leads to non zero value of the order parameter. The potential surface in the nematic phase is represented at three angles and three distances as shown in fig. 3.9.

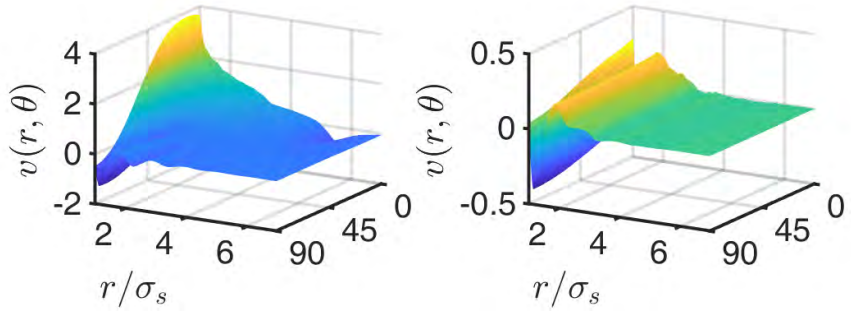

Figure 3.8: The potential surfaces calculated from the pair correlation function of the hard prolate spherocylinders in (left) the nematic phase and (right) the isotropic phase; σ_s denotes the solvent diameter.

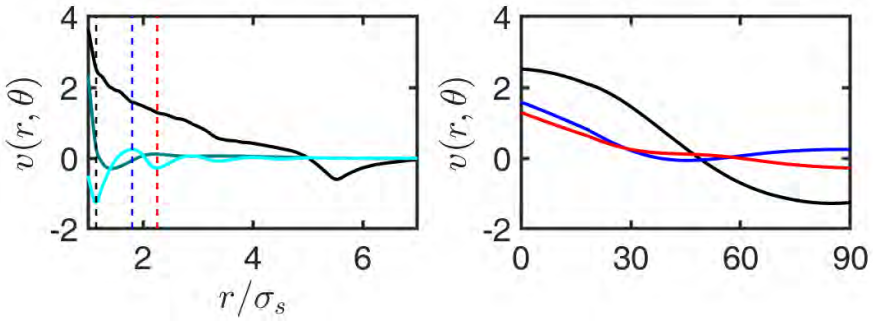

Figure 3.9: The potential curves as a function of (left) distance at a given angle and (right) angle at a given distance; the angles in the left panel are 0, 45 and 90°, black, green and cyan lines, respectively; the distances in the right panel are σ, σ + solvent radius and σ + solvent diameter, black, blue and red, respectively; the dash lines in the left panel mark the chosen distance; σ_s denotes the solvent diameter.

The potential as a function of the distance in the plane perpendicular to the director has the first minimum above the solvent diameter because of the small

disorder. The second minimum in the potential marks the second shell of the solvent molecules. The potential as a function of the distance increases and reaches the maximum in the plane parallel to the director. At this angle, the potential function shows the first minimum at 5.5 times σ_s. This number corresponds to the aspect ratio of the solvent shape, $(1.64 + 0.36)/0.36 = 5.55$. The angular dependent potential curve has the maximum difference at the first solvent shell and the difference decreases with the distance. The potential surface becomes homogeneous after 7 times σ_s. This potential surface is implemented into the calculation by assigning the first solvent shell as the contact distance and imposing into the space coordinate of the diffusion-reaction equation.

3.1.3 Sample preparation

The sample preparation for the fluorescence quenching study in DG mixtures was performed according to the scheme 3.1. First, DMSO and glycerol were weighted and mixed. A portion of this DG mixtures was kept to perform blank measurements. Second, the mixture and dye were combined to have a stock solution with optical density of 0.2 in 0.1 mm quartz cuvette. The quartz cuvette model 20C from Starna is a demountable cell with 0.1 mm path length. Third, the stock solution was weighted and divided into four portions. Three portions were mixed with three specific pure quencher volumes to have three different quencher concentrations, namely cq7, cq13 and cq18. The first portion is called cq0 because it does not contain the quencher. The other three solutions differ by the quencher concentrations and the increasing number represents the increasing quencher concentration. This division method is implemented to control the dye concentration for all solutions, while quencher mixing does not change the dye concentration. Fourth, each quencher concentration was weighted and mixed with the cq0 solution. This step generates 18 solutions with quenchers and one solution without quencher, 19 solutions in total. The final solutions have OD of 0.2 at the maximum absorbance. The sample preparation in 5CB is a bit different because the solubility of dyes is low. A few mg of dyes was added to 5CB at 323.15 K. The solution was stirred and heated up to 50°C over 2 - 3 hours. The hot solution was filtered two times with PTFE filters, pore size of 0.20 µm from CarlRoth. From this stock solution, the quencher mixing follows the procedure in scheme 3.1. For PeDMA in 5CB samples, the solution was prepared with the same method as described before but without adding quenchers.

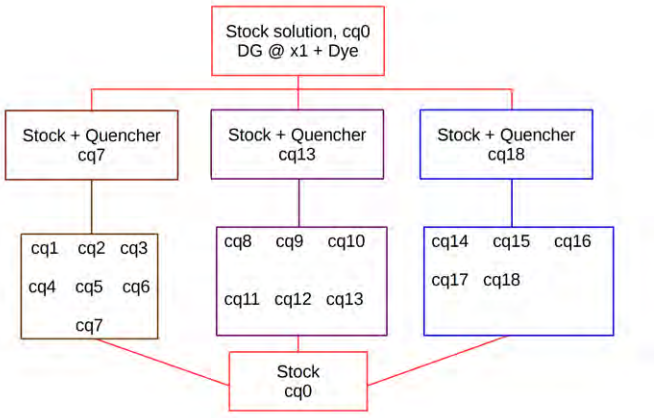

Scheme 3.1: A diagram explaining quencher concentration mixing for dyes in DG mixtures

To study the spectroscopic properties of samples, the solution was filled in a quartz cuvette. The samples from DG mixtures were prepared at room temperature, while the samples from 5CB solutions were prepared at 323.15 K and left to be cooled at room temperature. The demountable cuvette consists of one grooved window which determined the path length and another flat window. When closing the cuvette with the solution inside, the grooved window was fixed and the flat window was moved. The director and molecular alignment in nematic phase were investigated in using Polarized Optical Microscope POM and polarized absorption spectroscopy which are described later in this chapter. All spectroscopic measurements of dyes in DG mixtures and 5CB were measured in the same cuvettes. There was no sealing or degasing of the samples or solutions. The effect of the oxygen quenching is estimated to be less than 5% as mentioned earlier in section 3.1.1.

3.2 Measurements and equipment calibrations

3.2.1 Polarized optical microscope, POM

The polarized light microscopy is a technique used to determine the optical axis or the director of uniaxial materials like the nematic LCs. The technique works with the fact that the nematic LCs has birefringence. The birefringence describes a situation when a ray of light traveling through a material gets separated in two of perpendicular polarizations. To determine the optical axis of the birefringence material using the crossed polarizing microscope, let us consider the situation in fig. 3.10. The polarizer (P) is oriented in an east-west direction and the analyzer (A) is oriented in the north-south direction. The optical axis of the birefringence material (red rectangle) is the long axis of the

sample. The axis aligns parallel to the direction of the polarizer in the left panel. In the left panel, light passes through first the polarizer and then the sample. The polarization after the polarizer is parallel to the optical axis, and thus only a small portion arrives to the analyzer. This gives a dark image when viewed from the eyepieces which is located behind the analyzer. The same observation occurs when the sample is isotropic. On the other hand, a bright image is obtained when the sample is rotated at 45° as the right panel. The light after the polarizer is decomposed into two polarization according to the ordinary (o) and extraordinary (e) refractive indices. The amount of light passed to the analyzer is a sum of these vectors (R). By taking the image of LCs at different angles using POM, one can determine the nematic director.

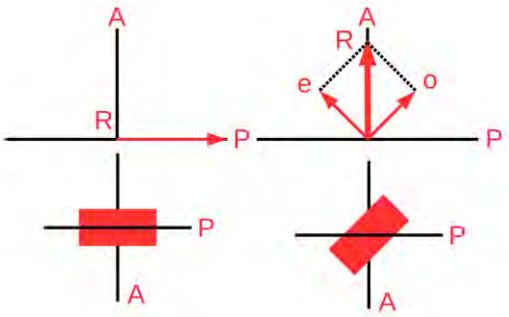

Figure 3.10: A birefringence specimen under the crossed polarizing light microscope; (left) the optical axis is parallel to the polarizer and (right) the optical axis is rotated 45°; the red rectangle represents the birefringent material; P and A denote the polarizer and analyzer; o and e denote the ordinary and extraordinary refractive indices; R is the sum vector of polarizations after the material.[139] NOTE: Light propagates normal to the plane of this page, and the detector is placed behind it. The upper panels show the polarization direction after the sample, in red. The black lines represent the polarization directions of P and A.

The images of LC samples were taken using a camera Nikon Eclipse E400 and a digital data conversion unit. The samples of R6G in 5CB in 0.1 mm cuvettes were photographed in the nematic and isotropic phases at different angles to assign the director. The results shown in fig. 3.11 indicates that the director of the samples is parallel to the long axis of the cuvette. The molecular alignment of 5CB on the quartz substrate was reported to be quasi-planar in the bulk[140]. The planar alignment is a state of the alignment when the molecular long axis is parallel to the substrate surface.

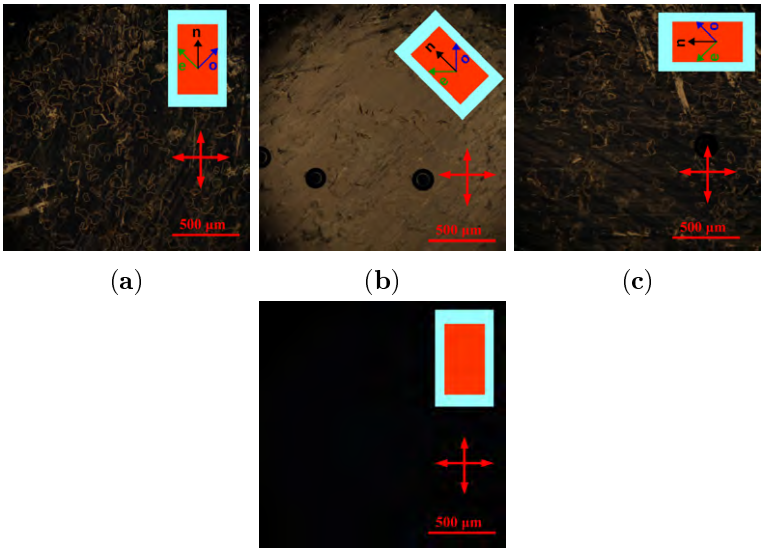

(**a**) (**b**) (**c**)

(**d**)

Figure 3.11: POM images of the sample in the nematic phase when (a) the cuvette's long axis is parallel to the polarizer, (b) the cuvette is rotated 45° from the polarizer and (c) the cuvette is rotated to be perpendicular to the situation in (a); (d) the sample is heated to get to the isotropic phase.

3.2.2 Steady State Absorption

The absorption spectra of samples at controlled temperatures were measured using Shimadzu UV 2700 and a Quantum Northwest temperature controller LUMA40. The LUMA40 is a user customized Peltier-based temperature-controlled cuvette holder with four optical ports as shown in fig. 3.12. It has a simple base which is compatible for an optical breadboard. It is compatible with a standard 1 cm cuvette size. Four optical ports permit many configurations for fluorescence measurements. The Peltier based temperature controlling system works from -15 to +105°C with water as a coolant. This model has a windowed jacket with dry gas purging allowing to work down to -40°C. Moreover, the system can be extended to a wider temperature range, -50 to +150°C. The certified product guarantees the temperature accuracy of 0.3°C and the temperature reproduciblity of 0.07°C. A magnetic stirring is another useful feature for this model. The maximum stirring speed is 2500 rpm.

Figure 3.12: A photograph of the LUMA40; there are four rectangles optical ports, two connectors for the water flow, one connector for dry gas inlet and an electrical communication port at the bottom right.

The 0.1 mm cuvette was combined with 1 cm cuvette adapter to be used in LUMA40. Two calibration measurements were performed to verify the temperature inside the samples and the thermal equilibrium time for the samples. The optical method for monitoring temperature in spectrophotometric analyzers was employed. The method tracks the absorbance of the 3,5-Dinitrosalicylic acid DNS in KOH solution at 480 nm[141]. Therefore, a reference measurement of DNS in KOH solution was first performed using Shimadzu UV 2401PC and temperature controller TCC240A CE. This instrument as a reference is calibrated annually. The temperature readouts in this calibration were taken after 10 minutes when there is no fluctuation of the readouts. A correlation of setting and actual temperatures for the LUMA40 using the absorbance-temperature function from the reference measurements is shown in fig. 3.13. The correlation of setting and actual temperatures obeys a linear function as following:

$$T_{set} = mT_{actual} + C \tag{3.9}$$

where m and C are the coefficients of the fitting which are 1.02 and -4.95 K, respectively. The difference between the setting and actual temperatures is less than 1.5 K in the experimental temperature range used in this work (293.15 - 323.15 K). Hence, there is no correction applied to the setting temperature. Another calibration is to find a thermal equilibrium time for the measurements. The absorbance of the DNS in KOH solution at 480 nm was recorded as a function of time. The absorbance was subtracted with the initial absorbance and normalized by the maximum absorbance. This time dependent quantity is called $A(t)$. The time traces in fig. 3.13 shows $A(t)$ for different setting temperatures. Each curve recording started from 15°C below the setting temperature. The curve for 45°C has a delay on the start time. From the results, it takes approximately 5 minutes to reach 90% of the maximum absorbance for all setting temperatures.

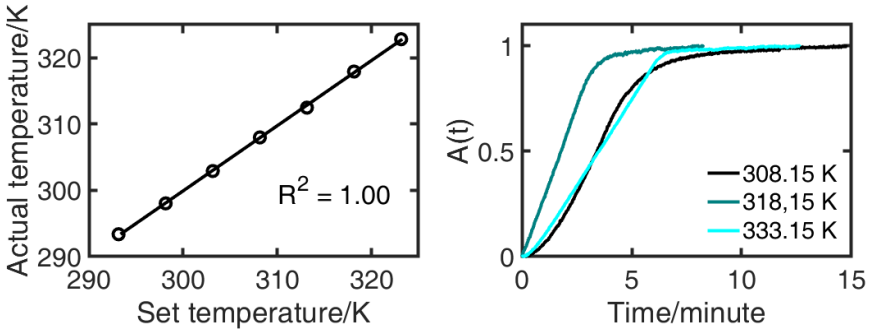

Figure 3.13: LUMA 40 calibrations for (left) the actual and setting temperature correlation and (right) time traces obtained from three setting temperatures

The wavelength position from the monochromator was also calibrated using a holmium glass filter from Hellma. The holmium glass filter spectrum was measured as a reference spectrum with the slit width of 0.5 nm. This filter is used as a reference because of its narrow bands and reliability. The absorption spectrum and the correlation function between the reference peak positions and the measured peak positions are shown in fig. 3.14. The result indicates the difference of 0.45 nm. This is within the slit width of the measurement. Therefore, there is no need to correct the result of the absorption measurements.

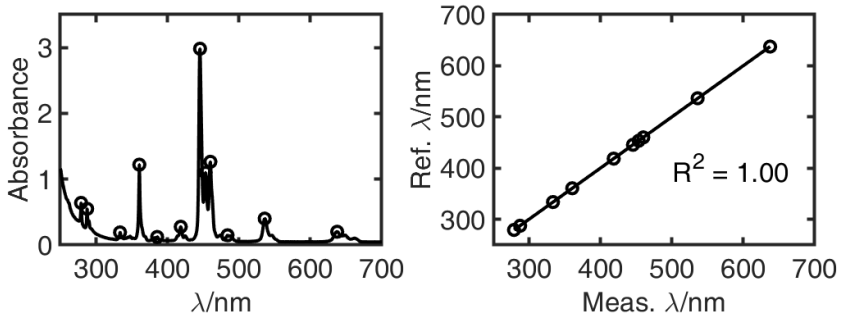

Figure 3.14: (left) The absorption spectrum of the holmium glass filter and (right) the linear correlation function of reference and measured absorption peaks; Circles represent absorbance peaks and the line indicate the correlation function.

The absorption spectra were obtained in the range of 350 - 800 nm with a monochromator slit width of 1 nm. The absorption spectra of dyes in DG mixtures were measured against air as well as the DG mixtures without dyes. All of the spectra were processed after the measurements. The spectra of dyes in DG mixtures were simply subtracted with the corresponding spectra of DG mixtures. The spectra were converted into the transition dipole moment spectrum. The TDM representation was obtained using a description from the literature[142]. The absorption spectrum was multiplied by the wavelength in nm to get the TDM spectrum. The TDM representation against energy is a proper representation to estimate the photophysical properties of fluorophores because it allows direct comparison with the fluorescence emission spectra.

The absorption spectrum of dyes in LCs shows anisotropy, meaning sensitivity to the polarization state of light. Therefore, two identical polarizers were installed in the light path of the sample and the reference[143]. Two components of the absorption anisotropy are parallel and perpendicular absorption, $A_{\parallel}$ and $A_{\perp}$, respectively. The $A_{\parallel}$ spectrum was measured by setting the polarizers parallel to the director in the nematic phase and the $A_{\perp}$ spectrum was measured when the polarizers were rotated 90° with respect to the parallel measurement. The spectra of dyes in LCs were also measured against air as mentioned earlier. The absorption of the samples in 5CB consists of the 5CB absorption band around 300 nm and a portion of light scattering in the nematic phase. It was found that this additional dispersion in the absorption spectra in nematic LCs could be well reproduced using the function

$$A(\lambda) = a_1 \exp\left(- \frac{(\lambda - a_2)}{a_3} \right) + a_4 \tag{3.10}$$

where a_1 - a_4 are free parameters for the fitting. The fitting of the background absorption is performed where there is no dye absorption. For example, the R6G absorption band in the nematic phase is in the range of 440 - 600 nm. The background absorption fitting range in this case is composed of the regions 420 - 440 nm and 600 - 700 nm. The fitting results shown in fig. 3.15 indicate the validity of this background subtraction method. The background absorption spectra of 5CB with and without dyes are not the same. This is due to the addition of dyes decreases the order.

The parallel and perpendicular absorption spectra were taken to calculate the order parameter S_A of dyes in LCs[143]. The equation reads

$$S_A = \frac{A_{\parallel} - A_{\perp}}{A_{\parallel} + 2A_{\perp}} \tag{3.11}$$

where $A_{\parallel,\perp}$ is an integrated area of the dye absorption band for parallel or perpendicular measurements, respectively. The order parameter S_A represents

the average angle of the transition dipole moment of dyes with respect to the polarized light.

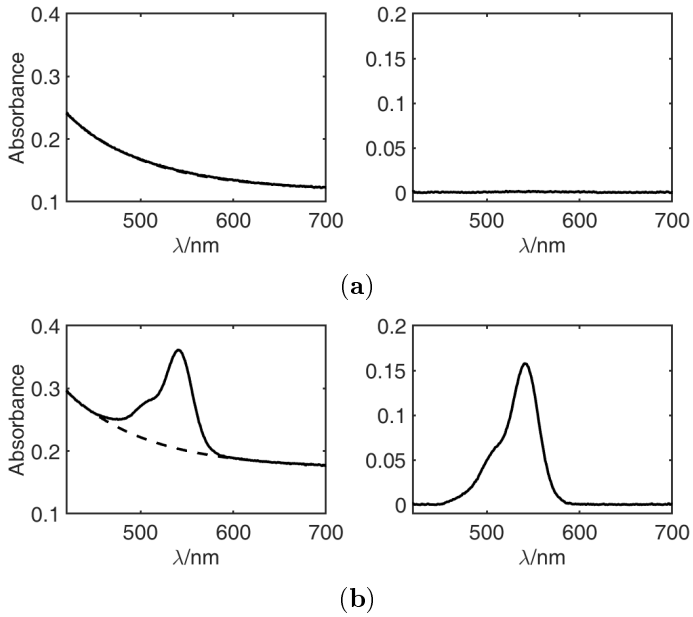

Figure 3.15: (left panel) Absorption spectra (line) and background fitting (dash) of (a) nematic 5CB at 293.15 K and (b) R6G in nematic 5CB at 293.15 K, (right panel) absorption spectra after subtraction of (a) nematic 5CB at 293.15 K and (b) R6G in nematic 5CB at 293.15 K

3.2.3 Steady State Fluorescence

The emission spectra of samples at controlled temperatures were measured using Horiba Fluorolog 3 and Quantum Northwest temperature controller LUMA40. Fluorolog 3 is a commercial spectrofluorometer which has a big sample chamber. The sample in 0.1 mm cuvette together with LUMA40 was combined with an adapter to fit in the sample chamber. It was placed at the focal plane for the Front Face (FF) configuration. The FF configuration collects the emission from the sample front as shown in scheme 3.2. The position of the focal is measured by finding the position of the sample which gives the maximum emission intensity. The excitation beam is polarized at the polarizer (P1) and reflected at the flat mirror (M1) to the parabolic mirror (M2). The excitation beam is focused in the center of the sample. The emission beam is collected using the parabolic mirror (M3) from the same focal plane at θ = 22.5° with respect to the excitation beam. This emission collection angle determined experimentally gives the same value as provided by the supplier in the manual. The emission is directed from the M3 to the flat mirror (M4) and

reflected to the polarizer (P2). The polarized emission after the P2 is recorded in the detection compartment module which is not shown here.

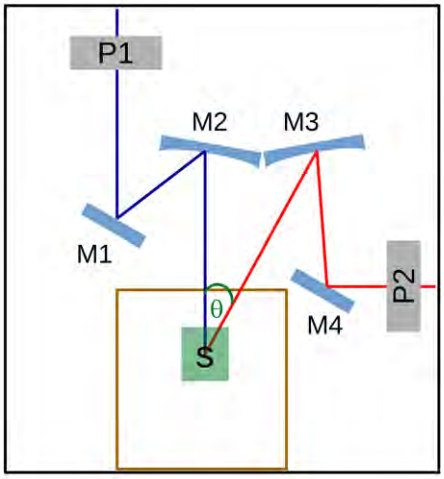

Scheme 3.2: A scheme of the sample compartment module in the Fluorolog3 for the front-face configuration consisting of 2 polarizers (gray rectangles), 4 mirrors (blue rectangles) and one sample holder (opaque green)

Table 3.4: Measurement conditions for emission and excitation spectra using Fluorolog 3

	PeDMA in 5CB		Pe in DG/5CB		R6G in DG/5CB	
	Em.	Ex.	Em.	Ex.	Em.	Ex.
Ex. λ/nm	400	250 - 600	400	250 -600	500	250 - 600
Slit/nm	3	2	1 - 2	2	4 - 6	2
Pol./Degree	0	0	0	0	0	0
Em. λ/nm	390 - 850	550	390 - 650	500	490 - 750	580
Slit/nm	2	2 - 3	2	2 - 3	2	5 - 6
Pol./Degree	54.74	54.74	54.74	54.74	54.74	54.74

The emission and excitation spectra of samples were collected according to the parameters listed in table 3.4. Three calibrations were performed to verify the reproducibility of the measurements including monochromator calibration, wavelength sensitivity and polarization anisotropy. The emission and excitation spectra were corrected only for the wavelength sensitivity after recording. The monochromator correction is neglected because the monochromator calibration shows the deviation smaller than 0.16 nm, 10% of the slit width. For the monochromator calibration of Fluorolog3, 4 spectra were collected with slit

width of 0.2 nm. The measurements were conducted according to fig. 3.16a. Two excitation spectra with fully open emission slit were collected – with and without Spectralon. The Spectralon is placed in the sample holder in 3.2. Spectralon is a fluoropolymer which has high diffuse reflectance over the ultraviolet, visible and near-infrared regions of the spectrum. The material can be formed into any shapes or coated on any surfaces. The shape of the Spectralon in this calibration is a prism. These two spectra were used to calculate absorbance and locate the peak positions. The same setting were applied for measuring emission spectra with and without Spectralon. The peaks positions obtained from excitation and emission spectra were plot to find the correlation in fig. 3.16b. The differences are also less than wavelength resolution. Therefore, there is no need for the correction.

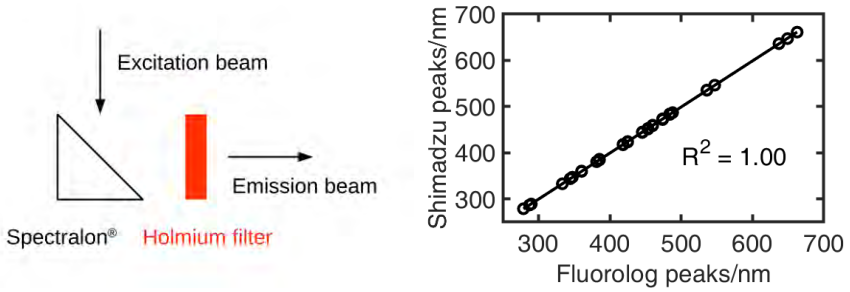

(**a**) (**b**)

Figure 3.16: (a)Measurement setup for Fluorolog3 monochromator calibration and (b) linear correlation function of peak positions from Shimadzu UV2700 and and Fluorolog 3

For the wavelength sensitivity calibration in the emission detection, a set of secondary emissive standards were measured according to the literature[144]. The secondary emissive standards are Tryptophan, α-NPO, TPB, Coumarin 153, DCM and LDS 751 solutions. The recorded spectra ranging from 300 nm to 800 nm were processed with respect to the provided standard emission spectra. Finally, an emission correction curve was generated and used to correct the emission spectrum. For the wavelength sensitivity calibration in the excitation detection, a concentrated solution of Rhodamine B was measured according the operation manual from Horiba[145]. The excitation spectrum of the concentrated Rhodamine B was measured at the emission wavelength of 650 nm. The excitation correction curve was applied to the excitation spectrum. Both correction factor the emission and excitation detections are shown in fig. 3.17.

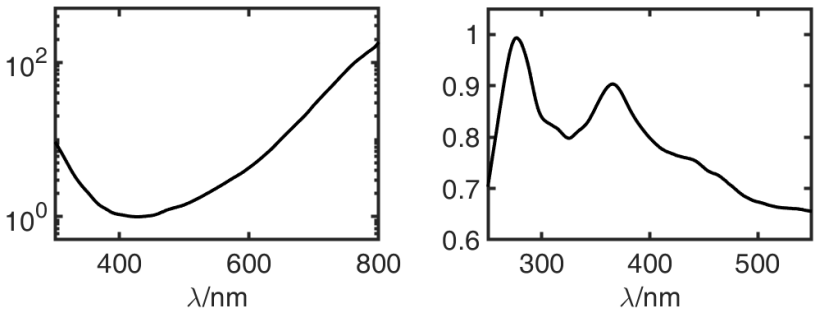

Figure 3.17: Correction factor curves for (left) the emission detection and (right) excitation detection for the Fluorolog 3 spectrofluorometer

3.2.4 Spectral characteristics

The absorption, emission and excitation spectra in this study were obtained as a function of wavelength because the detection system uses a diffraction grating. In order to extract E_{00}, it is better to transform the experimental data to the transition dipole moment representation TDM[142]. The average of the maximum absorption position and the maximum emission position of the spectra in the TDM representation defines E_{00}. For further analysis, the first and second moments of the absorption and emission spectra are defined as follows:[146, 147]

$$\begin{aligned} m_1 &= \int \tilde{\nu} S(\tilde{\nu}) d\tilde{\nu}, \\ m_2 &= \int (\tilde{\nu} - m_1)^2 S(\tilde{\nu}) d\tilde{\nu}, \end{aligned} \tag{3.12}$$

where $S(\tilde{\nu})$ is the area normalized spectrum of interest. m_1 corresponds to the average spectral position, while m_2 is the spectral variance. Hence, $\sqrt{m_2}$ is the spectral width. The first and second moments are employed to represent the spectral properties instead of the conventional peak and width.

3.2.5 ns-Time Resolved Fluorescence

ns-Time resolved fluorescence decays were obtained from TCSPC measurements. The home-made TSCPC setup consisted of (i) picosecond pulsed laser diodes from PicoQuant, model LDH-P-C-375 and LDH-P-C-520, (ii) a picosecond pulsed laser driver from PicoQuant, model PDL 800-D, (iii) a double grating monochromator, model CM110 from Spectral Products, model cm-110, (iv) a photomultiplier tube model PMC-100 from Becker and Hickl and (v) a single photon counting card from PicoQuant, model Time harp 100. The excitation frequency was 10 MHz and the power was controlled using a variable ND filter wheel from Thorlabs, model NDC-50C-2M. The laser diode was placed at 5.5°

to the main axis to avoid reflections of the excitation into to the detector. The polarization was set to S-polarization. The polarization state of the source was determined by the reflected light from a piece of borosilicate glass. The reflection of S-polarization vanishes at the Brewster angle. A Glan-Taylor polarizer was set to magic angle and placed after the sample. A longpass filter was placed before the monochromator to remove scattered excitation. The fluorescence decay was selected at the maximum emission wavelength with a band width of 1.2 nm. The scheme is shown in scheme 3.3. IRF was measured by collecting scattered photons at excitation wavelength in the LUDOX solution. The FWHMs of the IRFs measured from LDH-P-C-375 and LDH-P-C-520 are 0.31 and 0.66 ns, respectively.

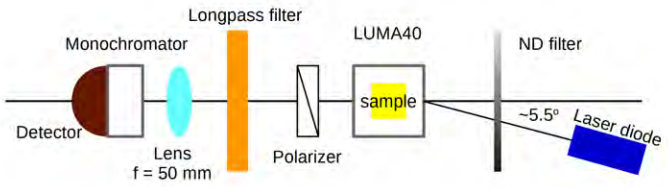

Scheme 3.3: TSCPC setup scheme to measure samples at a controlled temperature in LUMA40; the excitation is S-polarization and the emission is collected at the magic angle; the excitation angle is not drawn to scale.

3.2.6 fs-Time Resolved Fluorescence

The measurements of fs-time resolved fluorescence were performed using a setup described by Wnuk and co-workers[148]. The setup consists of several modules including a seed laser, a two-stage regenerative amplifier, two tunable non-collinear optical parametric amplifiers NOPAs, an Andor spectrometer and a Hamamatsu EM-CCD camera. The seed laser is generated using a Ti:Sapphire oscillator centered at 795 nm. This seed laser is amplified with a high power laser of 18 W at 532 nm. The compressed amplified beam (795 nm, 4W and 5kHz) is used to generate the excitation and gate beams in NOPAs. The tunable excitation wavelength range is 475 - 790 nm and the polarization is set to the magic angle (54.74°). The gate wavelength is fixed at 1020 nm. The fluorescence from the sample is converted in a 0.2 or 2.0 mm BBO with the gate beam. The different incident angles of the beams with respect to the BBO surface convert different parts of the fluorescence spectrum. The output signal is detected with the spectrometer and camera.

The Fluorescence Optically Gated technique FOG takes benefit from the optical non linear processes to gate the fluorescence reaching a time resolution of $<$ 100 fs. The basic idea of FOG technique as shown in scheme 3.4 is

explained as follows. A short excitation pulse (blue line) produces a broad fluorescence (green line) in the sample. Another short pulse with a longer wavelength than the excitation is the gate pulse (red line). The gate pulse gets reflected by mirrors in the delay stage generating the delay time (τ_{delay}) to meet the fluorescence pulse in the non linear crystal, BBO. If both pulses meet in the crystal with an appropriate angle also known as the phase matching condition, sum frequency photons are generated only during the time when the gate pulse is present in the crystal thus keeping the time resolution within the pulse width. The generated photons form an upconverted pulse (magenta line).

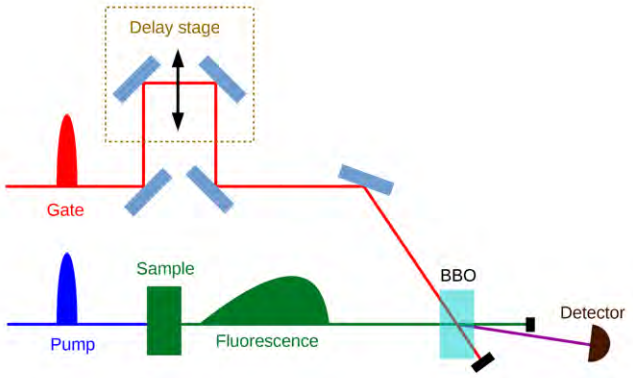

Scheme 3.4: A scheme of the time resolved fluorescence upconversion setup

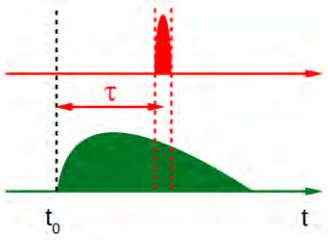

Scheme 3.5: A piece of the fluorescence pulse at the delay time τ_{delay} is upconverted into a higher frequency pulse

The time trace of the fluorescence evolution is recorded as shifting the delay time in the gate pulse as shown in scheme 3.5. The delay stage in this setup is 50 cm long which gives a maximum delay time of 1.7 ns. The IRF for this technique is determined by the cross correlation measurement of the excitation and the gate pulses. The best IRF for this setup is 80 fs.

Regarding the optical technique, there are several limits in the detection system such as mirror transmittance, wavelength range of the spectrograph, second harmonic of the gate and sensitivity of the CCD camera. According to the sum frequency generation using the gate wavelength of 1020 nm, the detectable emission wavelength range is 380 - 800 nm including the limits mentioned before. The crystal thickness also governs the pulse duration of the upconverted pulse. There are two BBO crystals in this study which give the IRF of 80 - 720 fs depending on the measurement conditions. The phase matching condition is the crucial requirement to detect the upconverted photons from the fluorescence. The time resolved FOG measurements of the fluorescence quenching at different temperatures and quencher concentrations were performed under the same conditions. The intramolecular electron transfer study at different temperatures were performed as mentioned in table 3.5.

Table 3.5: Measurement conditions for FOG

	PeDMA in 5CB	Pe in DG or 5CB	R6G in DG or 5CB
Ex. λ/nm	400	400	500
Polarization/degree	magic angle	S	S
Excitation filter	ZUL422	ZUL422	ZUL530
Gate λ/nm	1020	1020	1020
BBO thickness/mm	0.2	2.0	2.0
Up-converted filter	ZUS450	ZUS385	ZUS450
IRF/fs	220 - 240	700 - 720	380 - 390

Note: ZUL – longpass filter and ZUS – shortpass filter

In order to control the uncertainty of the FOG measurements, the measurement conditions for the intramolecular and intermolecular electron transfer studies are strictly controlled and summarized in table 3.5. The fluorescence decays for the fluorescence quenching were recorded at a narrow wavelength range and using a thick BBO crystal to maximize the upconverted signal. The excitation power was 0.1 - 0.3 mW measured before the sample. The excitation beam size is $\leq$ 1 mm^2 in the sample. The sample was placed in the LUMA40 to control the temperature. The LUMA40 was attached to a automatic translation stage. The computerized translation stage consists of two stepper motorized actuators (model ZST213B), two step motor drivers (model KST101) and one 3-Axis translation stage (model RB13M/M) from Thorlabs. The speed and displacement were controlled to produce a Lissajous movement of the samples in order to avoid photobleaching. The Lissajous movement covers area of 3x6 mm^2. This small area is limited by the optical window of LUMA40. The sample movement was set to be perpendicular to the excitation beam and the emission was collected by a Schwarzschild objective with a numerical aparture of 0.52. The output beam after the objective was shaped using an iris to have a constant image shape at the BBO. Later the fluorescence

beam was gated in the BBO crystal and the upconverted signal was detected using a CCD camera from Hamamatsu.

In the case of the intramolecular electron transfer study, it is necessary to collect the whole spectrum with the shortest time resolution. For example, the kinetics of PeDMA in THF happens from 100 fs[95] and the steady state emission spectrum covers 450 - 750 nm. Therefore, two calibrations were performed including that of the monochromator wavelength and wavelength dependent sensitivity in the detection system. First, the monochromator wavelength was calibrated using mercury-argon lamp (model HG-1) from Ocean Optics. The mercury-argon lamp output was coupled with a fiber optics (model ML92L) from Thorlabs which transmits 250 - 1200 nm. The fiber optics output was directed to the entrance of the spectrograph. The spectrum of the mercury-argon lamp has many sharp lines from 250 nm to 950 nm. Hence, the spectrum recordings were performed in small wavelength windows using the grating type 1 in the Andor monochromator, 150 grooves/mm, slit width of 100 nm. The pieces of spectra were combined into a whole spectrum. The peak positions of the measured spectrum as shown in fig. 3.18 were correlated with the reference data provided by the supplier. A linear correlation of the measured and reference peak positions gives a coefficient of 1 and a offset of 14.65 nm with the fitting quality R^2 of 1.000

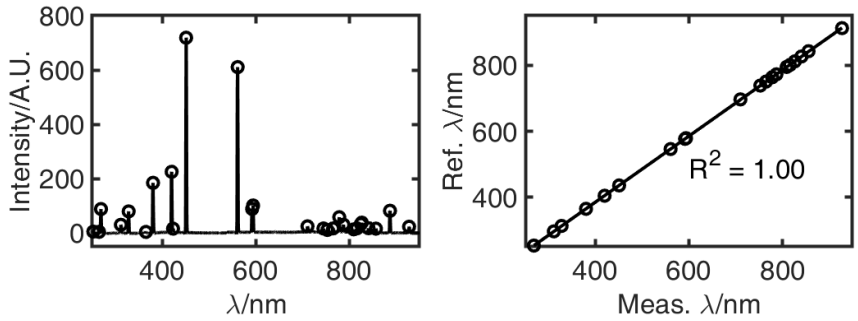

Figure 3.18: (left) A spectrum of Hg-Ar lamp with peak position marked as circle and (right) a linear correlation between the measured data and reference data

Second, the wavelength sensitivity in the detection system was calibrated using a set of secondaty emissive standards including BBOT, C6H, C153 and DCM according to the reference[95]. The long time spectra of the standards were taken at the delay time of 250 ps where there were no difference between this spectrum and the spectrum at the end of the delay stage, the delay time of 1.2 ns. The correction curve was generated similar to the procedures mentioned in the reference[144]. The correction curve was measured before each of the sample measurements.

In order to acquire the PeDMA kinetics in 5CB, the measurement was performed using the condition mentioned in table 3.5 and followed three consecutive steps as follows (i) the measurement of 4 standard spectra, (ii) the measurement of PeDMA and (iii) the measurement of 5CB. The total time of the measurement is 4 - 6 hours. The measurement of the 5CB is necessary because the second harmonic generation was intense and the position lies within the sample spectrum. The most time consuming measurement is the sample measurement.

The sample measurement suffers from many problems such as low dye content, excitation scattering in the nematic phase, high photobleaching in the nematic phase, second harmonic generation of the gate and therefore low signal to noise ratio. About the dye content in 5CB, increasing the dye content decreases the molecular order in the nematic phase and leads to the dye segregation. Increasing the illumination area while moving the sample can reduce the photobleaching problem. As discussed earlier about the small movement area of 18 mm^2, there is no indication on the area needed to avoid this problem. One has to consider that the dye lies in the tight nematic phase and it is not likely to diffuse away. Moreover, increasing the sample displacement also risks the sample plane to be not perpendicular to the excitation beam. Increasing the fluorescence before the BBO crystal can reduce the second harmonic generation of the gate as well as increase the signal to noise ratio. All of the improvement proposed here are beyond the capability of this setup. A new scheme of the measurement is needed to overcome the photostability and signal conversion problems.

Chapter 4

Results and Discussion

Two kinds of the electron transfer reactions are studied in this work : intramolecular and intermolecular. Both kinds of the electron transfer reactions are performed in DG mixtures as well as liquid crystals at different temperatures. The study of the intramolecular electron transfer reactions employs a donor covalently linked to an acceptor molecule. The theoretical predictions in terms of the GSE and GLE are compared with the experiments. This is discussed in the first section. In the second section, the intermolecular electron transfer reactions are studied using one donor and two acceptors. One pair of the donor and acceptor is similar to the intramolecular electron transfer study. The diffusion-reaction kinetics is studied based on the fluorescence quenching. The reactions in DG mixtures are used as a reference study to extract the electron transfer parameters. In LCs three different reaction-diffusion models with increasing level of anisotropy are compared to the experiments. Their capabilities are discussed.

4.1 Intramolecular electron transfer

Most of the results published about reactions in liquid crystals, are about intramolecular reactions (besides some reports of reactions between the solute and the LC itself)[23, 25, 26, 149]. Therefore, a good comparison in the present work would be to start by studying a reaction between moieties similar to those employed in the intermolecular study. We count on such a molecule: perylene covalently linked to DMA. This molecule has been studied in Ref. [112] and more recently in Ref. [95]. We summarize here some of the results presented in the latter work and the attempt to expand the study to LC.

The following steps need to be performed in a study of this kind:
1. Identification of the reaction: the best way to determine if there is an electron transfer reaction is by means of transient absorption. As presented in the mentioned publication, depending on the solvent, PeDMA shows either only a

transient absorption band corresponding to the local excited state of perylene, like in cyclohexane, or a continuously moving band in between the previous band and the one of the perylene free radical anion. (see fig. 4.1 adapted Ref. [95]).

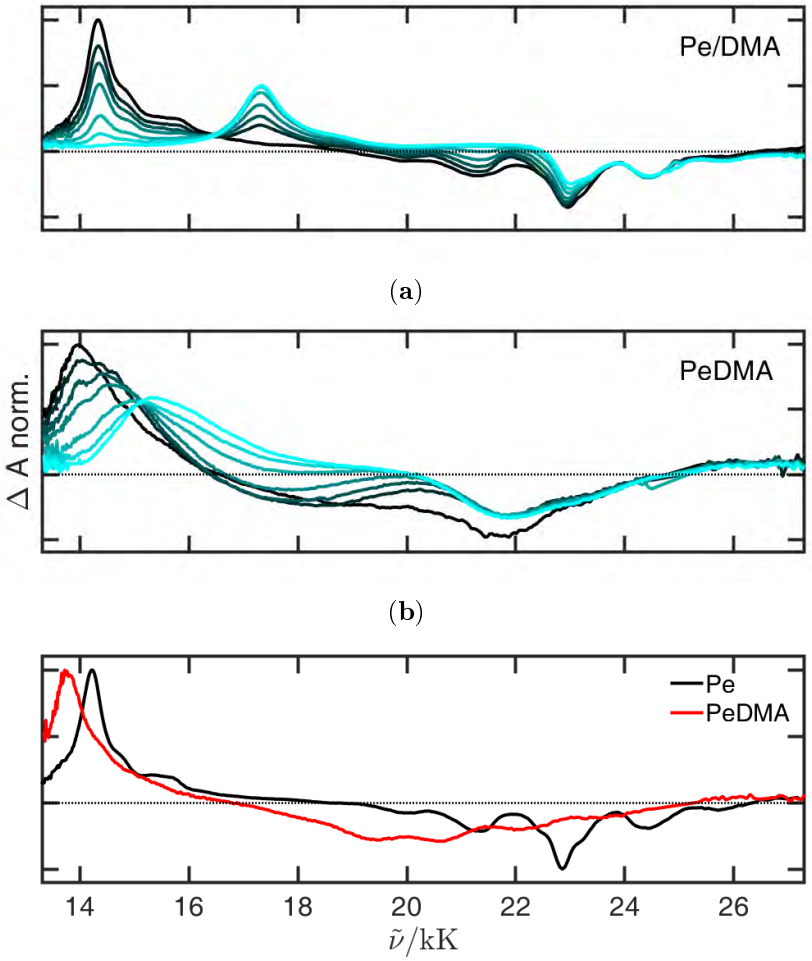

Figure 4.1: Transient absorption spectra of (c) Pe and PeDMA in cyclohexane after 5 ps; transient absorption spectra at a given time of (b) PeDMA in DMSO and of (a) Pe and DMA (0.8 M) in acetronitrile; the corresponding times in (a) are 0.5, 5, 10, 20, 50, 100 and 500 ps as indicated by the color from black to cyan, respectively; the corresponding times in (b) are 0.2, 0.5, 1, 2, 5, 10 and 50 ps as indicated by the color from black to cyan, respectively;

Interestingly, no isosbestic point can be identified in this spectral evolution, in contrast to the clearly observed in the reaction between the freely diffusing perylene and DMA. This indicates that in the intramolecular reaction there is a charge shift from DMA moiety to perylene very likely with a coupling between the states much larger than in the intermolecular reaction.

2. Construction of the potential energy surface. This is done by measuring the steady state solvathochromism of PeDMA in a sufficiently large set of solvents. Some of these spectra are shown in fig. 4.2. The absorption band shifts to the red with increasing the solvent polarity but much less that the emission spectra which go from a perylene like spectrum in low polar solvents with a small Stokes shift, to a very broad red shifted spectrum in highly polar solvents.

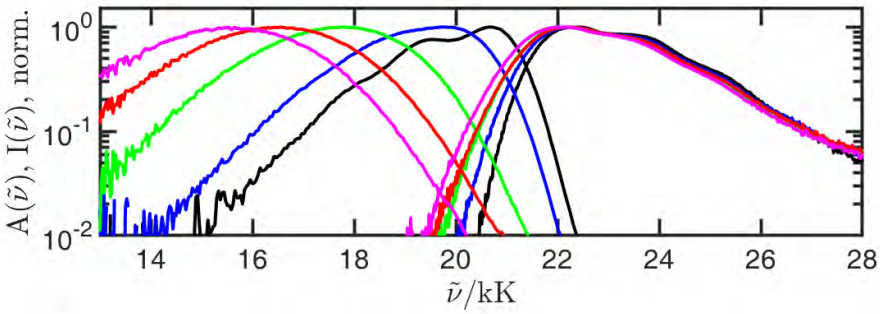

Figure 4.2: Normalized absorption and fluorescence spectra of PeDMA in 5 selected solvents (black: n-hexane; blue: n-butyl ether; cyan: tetrahydrofuran; red: butylronitrile; magenta: dimethylformamide)

In the mentioned publication, and as explained in the theoretical part, from the position and shape of the absorption and emission of fluorescence bands, the required parameters for the construction of the surface were obtained. The results are shown in scheme 4.1 and table 4.1. It is worth mentioning that the coupling for this intramolecular reaction is of 1.3 kK, or 160 meV, which is about 6 times k_BT, in other words the reaction is clearly adiabatic. Therefore the Marcus theory is inapplicable and one needs a Kramers like treatment as presented in the theory chapter.

Table 4.1: PeDMA-parameters establishing in solvents of arbitrary ϵ and n_D

	State-specific		
	$i = g$	$i = l$	$i = c$
μ_i/D	3.26	5.8	33.2
μ_{ig}/D		4.8	-2.2
U_i/hc/kK	0	22.9	27.0
	Common		
J/hc/kK	1.3		
α/Å^3	71		
a/Å	7.76		
$2D/hca^3$/kK	3.9		

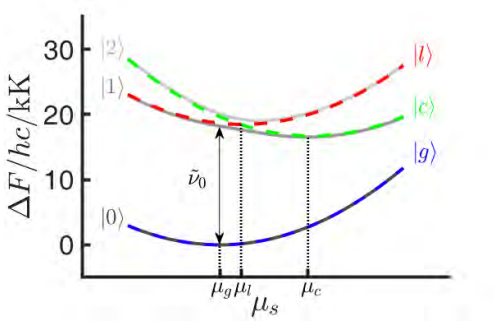

Scheme 4.1: Energy scheme depicting the relevant diabatic (dashed blue, red, and cyan lines) and adiabatic (dark and light gray) states and quantities. Note that the ordinate has been set to zero by subtracting $(U_g - \frac{1}{2}B_g^{\mathrm{tot}}\mu_g^2 + B_g^{\mathrm{el}}D)/hc$

3. Determination of the friction. The two models presented in the theory part require the knowledge of the friction kernel (GLE) or the diffusion coefficient over the FES (GSE) from an additional measurement. To this end a reference molecular system showing a remarkable solvation dynamics (and well studied [81]) with a known FES was measured. This system is coumarine 153, which is assumed to have parabolic FES in the first two singlet states. Having these FES, from the solvation dynamics one can obtain the mentioned quantities as described in the theoretical section. All the parameters related to them are to be found in the SI of the paper.

4. Recording of the spectral time evolution of PeDMA. In the original work this was performed by means of fluorescence up-conversion recording the full corrected spectra of the substance in many different solvents. In fig. 4.3 some examples in solvents ranging from low polarity (isopropyl ether) to high polarity (dimethylsulfoxide) are shown. Clearly the amplitude of the spectral changes increases with it. From these spectra the first and second moments

are extracted. These are the observables, instead of the full spectra, which are compared with the results of the simulations. As explained in the theoretical part, with assistance of the reference compound, the observable can be simulated with the two models without any fitting parameters associated specifically to the time resolved fluorescence measurements see fig. 4.4.

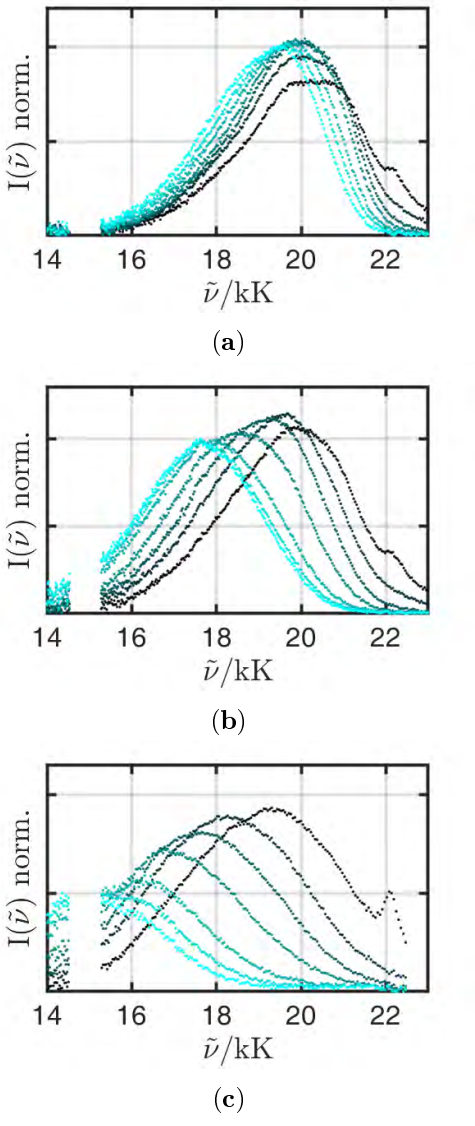

Figure 4.3: Time resolved emission spectra of PeDMA in (a) i-propyl ether, (b) tetrahydrofuran and (c) dimethylsulfoxide at a given time; the corresponding times are 0.2, 0.5, 1, 2, 5, 10 and 50 ps as indicated by the color from black to cyan, respectively.

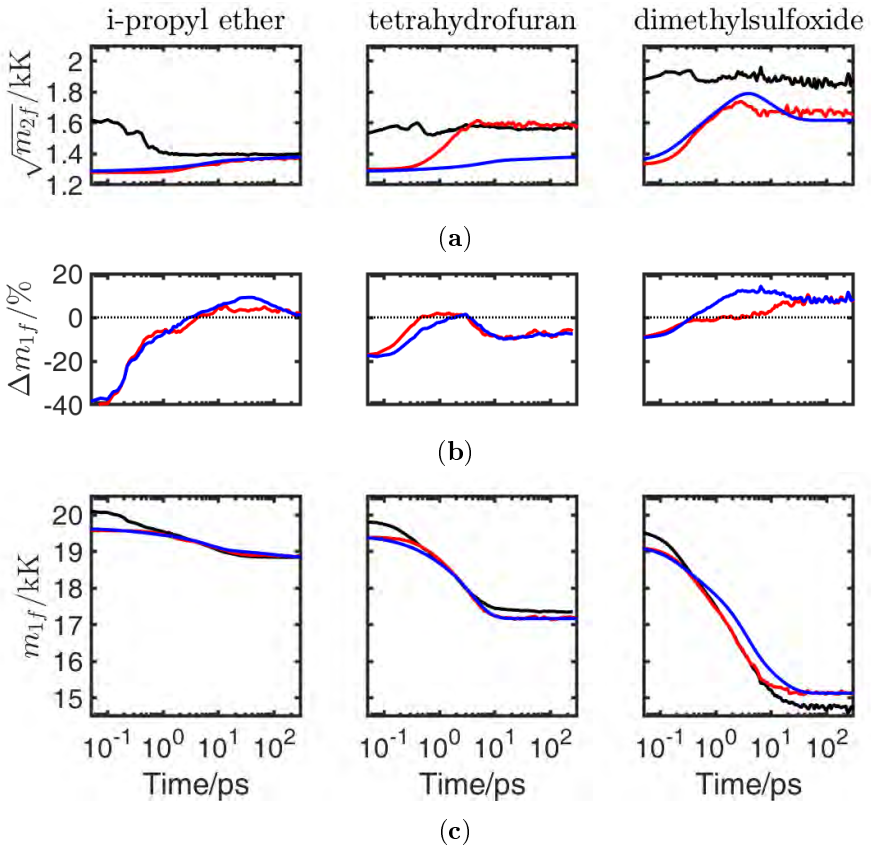

Figure 4.4: Comparison of the experimental and simulated (c) m_{1f} and (a) $\sqrt{m_{2f}}$ in three solvents. The experimental data denotes as black line. The simulated data obtained from GLE and GSE denote as red and blue lines, respectively. In addition, the relative difference of the simulated and the experimental m_{1f}, given by $\Delta m_{1f} = (m_{1f}^{sim} - m_{1f}^{exp})/(m_{1f}^{exp}(t=0) - m_{1f}^{exp}(t=\infty))$, is shown in (b).

The conclusion to which we arrived in the article is that both models are quite capable of reproducing the experimental results in most of the solvents, although the GLE showed better agreement with them. In a series of measurements in DMSO-Gly at large viscosities both models failed. This was interpreted as a failure attachable to the way the friction was extracted from the reference compound: having different hydrogen bonding abilities, PeDMA and C153 felt different frictions in H-containing solvents, like in rich Gly mixtures.

An interesting question rises about the large difference in the coupling matrix element for electron transfer in the intramolecular and intermolecular cases (as it was shown in [73] and we will see in this work later, the V_σ value obtained

for the bimolecular reaction between Pe and DMA is about 40 meV). It could be argued that the covalent bond is responsible for the difference. However, a single non-aromatic bond doesn't seem likely to couple strongly both aromatic moieties. The other possible explanation is that the configuration of the perylene DMA couple in the bonded case is special in the sense that favours a particularly large coupling. Some sort of chemical intuition imagines on the contrary, that the largest coupling should correspond to the sandwich like complex, rather than to the head-to-head one as it is the case in PeDMA, although it is known that the charge density in the DMA radical cation is quite large in the para position. In any case, this is beyond this work, but it is revealing an important clarification in the coupling obtained from the application of the Marcus expression in conjunction with the reaction-diffusion equation to the bimolecular quenching: the obtained coupling matrix element at contact is an average over a large number of configurations, and not the largest one.

In view of the above report, one could try to use the same strategy in LCs. First steady-state absorption and emission spectra were recorded.

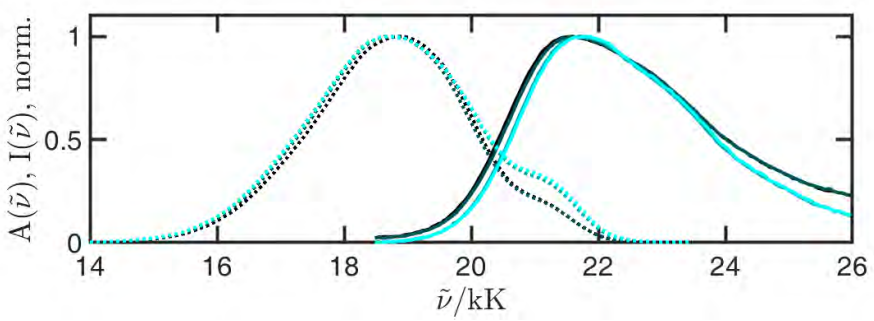

Figure 4.5: Normalized absorption and emission spectra of PeDMA in 5CB at four temperatures, 293.15, 303.15, 313.15 and 323.15 K, from black to cyan lines, respectively.

In the previous graph it can be seen that in 5CB the spectra resemble to those in THF, so the degree of charge transfer is medium, as corresponds to the average dielectric constant. With increasing the temperature, the absorption band center shifts to the higher energy as well as the band width decreases. On the contrary, the fluorescence band center slightly change with the temperature. The fluorescence band width gets significantly boarder at high temperature.

Time resolved emission was recorded by means of TCPSC and fluorescence up-conversion. A collection of the fit to the TCSPC can be found in table 4.2 (with all the details about the measurement and fit).

Table 4.2: Fluorescence decay fitting parameters of PeDMA in 5CB at different temperatures. The excitation wavelength is 400 nm and the polarization is S, 0°. The emission wavelength is 550 nm and the polarization is magic angle, 55°

Temperature/K	293.15	303.15	313.15	323.15
A_1	0.49	0.48	0.46	0.42
τ_1/ns	1.6	1.3	1.0	0.8
A_2	0.51	0.52	0.54	0.58
τ_2/ns	5.0	5.1	5.2	5.1
τ_{avg}/ns	3.3	3.3	3.3	3.3

A_i is the component ratio of the i lifetime.

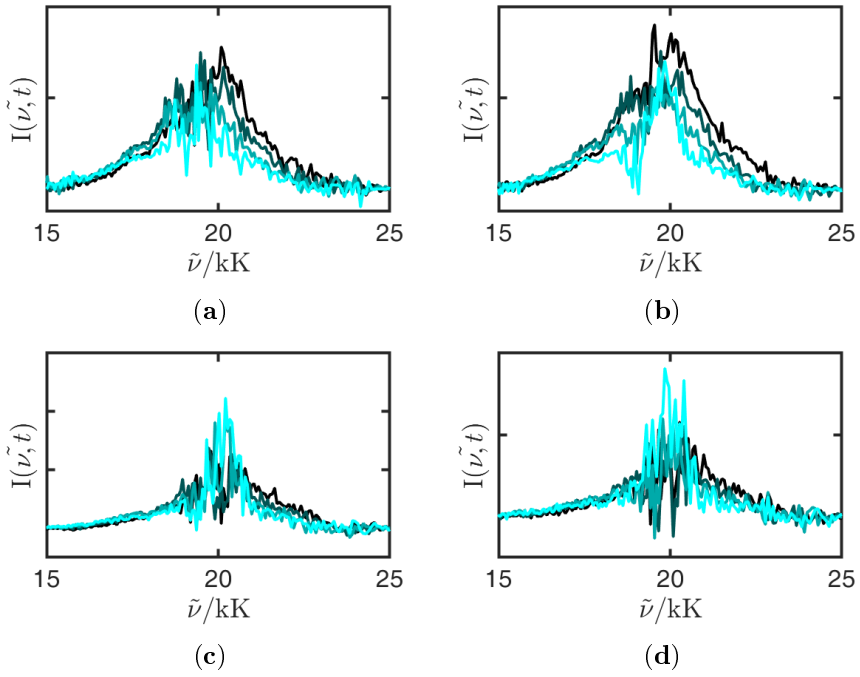

Figure 4.6: Decay associated spectra of PeDMA in 5CB at (a) 293.15 K, (b) 303.15 K, (c) 313.15 K and (d) 323.15 K at time of 0.8, 95, 490 and 1140 ps, from black to cyan, respectively.

The fits to the fluorescence decays give two lifetimes, one short and one long lifetimes. Both of them are too short for this compound. The obtained lifetimes are affected by the oxygen quenching. Moreover the average lifetimes are independent of the temperature. The lifetime in THF is 20 ns[112]. The spectra from the latter technique were corrected to remove the wavelength dependencies of the collection as described in the experimental chapter. The

attempts to perform these measurements lasted in between 4 to 6 hours due to the low signal from the sample. The reason is the relatively low solubility of PeDMA in 5CB. An additional complication comes from the slow degradation of the dye over time. The illuminated total area inside the thermostated sample is relatively small and in the LC the renovation of the dye by diffusion too slow. Unfortunately, these spectra are of a too low quality to performing any further physical studies on the intramolecular reaction. An improved system with a better S/N would be necessary.

4.2 Intermolecular Electron Transfer Reactions

Two different reactions were studied between an excited molecule acting as electron acceptor and a ground state species as donor. The fluorophores/acceptors are R6G and Pe, and the donor DMpT. In order to investigate the kinetics of these reactions the quenching of the fluorescence was monitored by means of steady state and time resolved techniques. Reactions were studied in isotropic and anisotropoic media, namely DG mixtures and 5CB. The measurements have been performed at four temperatures around the nematic-isotropic phase transition of 5CB, namely 293.15, 303.15, 313.15 and 323.15 K. In the first section we present the data in DG mixtures and the fit to them to extract the electron transfer parameters independent of the solvent. A good agreement between the experiments and the diffusion-reaction model is obtained. In the second section, the results in DG mixtures and LCs are compared without further theoretical explanations. Then, the electron transfer parameters obtained from the previous section are used to explain the results in the LC at all temperatures with three reaction-diffusion models, namely isotropic diffusion with centro-symmetric reactivity IC, anisotropic diffusion with centro-symmetric reactivity AC and anisotropic diffusion with asymmetric reactivity AA. Comparisons between three models are provided as well as discussion.

4.2.1 Determination of the electron transfer parameters in DG mixtures

Three electron transfer parameters were extracted from R6G-DMpT and Pe-DMpT fluorescence quenching including the contact distance of the reactant pair σ, the coupling matrix element V_σ and the decay length of the coupling matrix element L. The steady state absorption and fluorescence measurements were employed to quantify the quantum yield ratio $\phi(0)/\phi(c)$ and the zero vibronic transition energy between the ground state and the first excited state E_{00}. These two quantities, reactants' properties and the solvent properties in section 3.1.2 enter into the reaction-diffusion equation for the isotropic problem. The three electron parameters were obtained from the fitting of the model

to the experimental data at different viscosities and temperatures.

4.2.1.1 Characterizations of reacting systems in DG mixtures

The samples of R6G-DMpT and Pe-DMpT in DG mixtures were prepared as described in section 3.1.3. The steady state absorption and fluoresce spectra of samples at different temperatures were measured according to section 3.2.2 and section 3.2.3. The spectra in TDM representation were used to quantify the spectral properties including band center m_1, band width $\sqrt{m_2}$ and E_{00}. The transformation of the spectrum in wavelength representation to the TDM representation is explained in section 3.2.4. The absorption and fluorescence spectra of R6G in DMSO and Pe in DMSO are shown in fig. 4.7 and fig. 4.8. The fluorescence spectra of both were corrected for the wavelength sensitivity and the inner filter effect. The inner filter effect leading to reabsorption of the emitted light, occurs when the solution has a too high absorbance, typically over 0.1, in a spectral region common with the emission. This effect can be corrected by dividing a given spectrum with a factor $10^{-A(\lambda)}$[150] where $A(\lambda)$ is the absorbance of the sample in the fluorescence wavelength window. The R6G spectra do not show perfect mirror symmetry, in agreement with previous findings[151]. The peak position was used to calculate the zero vibronic energy $E_{00} = \frac{\tilde{\nu_a}+\tilde{\nu_f}}{2}$. A justification of the use of peak position instead of m_1 is that what is needed to calculate the free energy of the reaction is the average 0-0 transition energy. From the shape of the spectrum we can approximate that the position of the first peaks are proportional to the position of these transition, while the m_1 may contain deviations coming from the seemingly not obvious photophysics of this molecule.

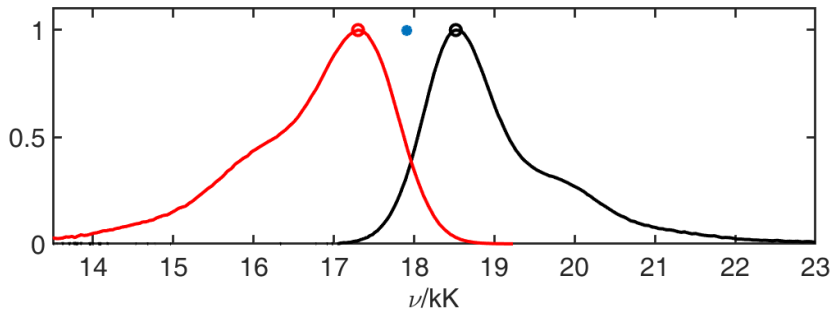

Figure 4.7: Normalized absorption and fluorescence spectra of R6G in DMSO at 293.15 K; the excitation wavelength is 500 nm; the opened circles mark the peak positions; the closed circle mark E_{00}.

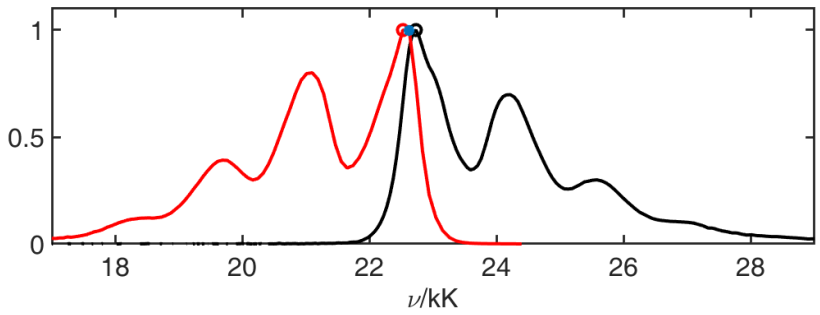

Figure 4.8: Normalized absorption and fluorescence spectra of Pe in DMSO at 293.15 K; the excitation wavelength is 400 nm; the opened circles mark the peak positions; the closed circle mark E_{00}.

The deviation from the mirror symmetry in both studied systems can be originated from several reasons such as the conformation changes in the excited state or the different coupling to the environment. The spectral changes due to the solvent polarization Δf is quantified using the first and second moments, band center and band width, respectively. The solvent polarization function is defined as [64]

$$\Delta f = f(\epsilon) - f(n_D^2) = \frac{\epsilon - 1}{2\epsilon + 1} - \frac{n_D^2 - 1}{2n_D^2 + 1}. \tag{4.1}$$

A plot of the spectral moments as a function of the solvent polarization for R6G in DG mixtures is shown in fig. 4.9. The absorption band center shifts to the higher energy while the fluorescence band center does not change with the increasing temperature. Moreover, the absorption band width also increases with the temperature while it remains constant for the fluorescence. This reflects the absorption spectrum broadening with higher temperature. The same temperature effect on the R6G absorption spectrum was reported[152, 153, 154, 155]. The origin of the effect is still unknown. The report indicates that the origin is not related to the solvent expansion, the hydrogen-bonding to the solvent nor the dye aggregation. On the other hand, adding glycerol shows a decreasing energy trend of the absorption and fluorescence band center while the band widths are not sensitive. The decreasing energy correlates well with the solvent polarization because R6G is a cationic molecule. The data points for pure DMSO are off the trend. This should be related to the hydrogen-bonding effect. Moreover, the R6G structure is flexible and have many moieties which can form hydrogen-bonding.

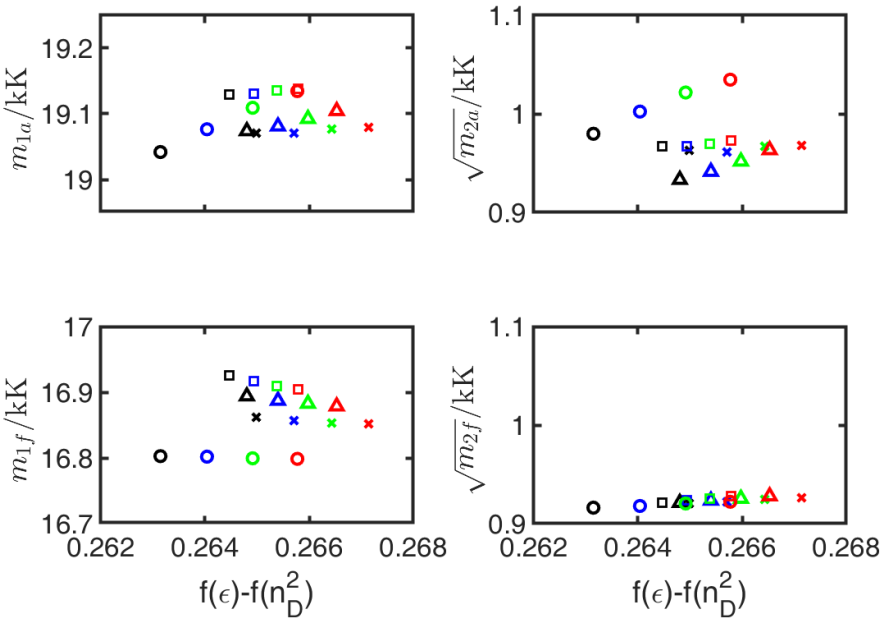

Figure 4.9: Band center and band width of R6G in DG mixutes absorption and fluorescence spectra at different temperatures and molar fractions of glycerol; black, blue, cyan and red colors stand for temperatures of 293.15, 303.15, 313.15 and 323.15 K, respectively; circle, cross, triangle and square stand for molar fractions of glycerol of 0.00, 0.35, 0.51 and 0.63, respectively.

In contrast with R6G solvatochromism, Pe is not sensitive to the temperature nor the molar fraction of glycerol changes. Pe is a neutral and rigid molecule. Therefore, the polarization function is not a good coordinate for the solvatochromism[156]. The Pe solvatochromism is better correlated with the refractive index function $f(n_D^2)$ because it is more sensitive to the dispersion force (solute polarizibility) and induction force (polarization of solvent by solute dipole). The refractive index function is the second term in eq. (4.1). In general, the spectral moments of Pe in DG mixtures are independent with the temperature and the molar fraction of glycerol. Only the absorption band center slightly increases with the higher temperature. This is originated from the decreasing of the refractive function[156]. The same effect should shift the fluorescence band center to the higher energy. Unfortunately, the fluorescence spectra suffers from the reabsorption effect. It is not clear to see the solvatochromic shift in this case, even after the correction for the inner filter effect.

The quencher addition could alter the absorption and emission spectral shapes. The absorption spectra of R6G in DG mixtures get narrower while the fluorescence spectra remain unchanged as the quencher concentration increases. On the other hand, the absorption spectra of Pe in DG mixtures remain un-

changed while the fluorescence spectra get narrower as the quencher concentration increases. The band narrowing could be explained by the changes of the solution refractive index. The refractive indices of DMSO and glycerol in table 3.2 are lower than DMpT ($n_D = 1.557$). Increasing quencher concentration increases the solution refractive index. Therefore, the energy gap between the ground and excited state increases[156].

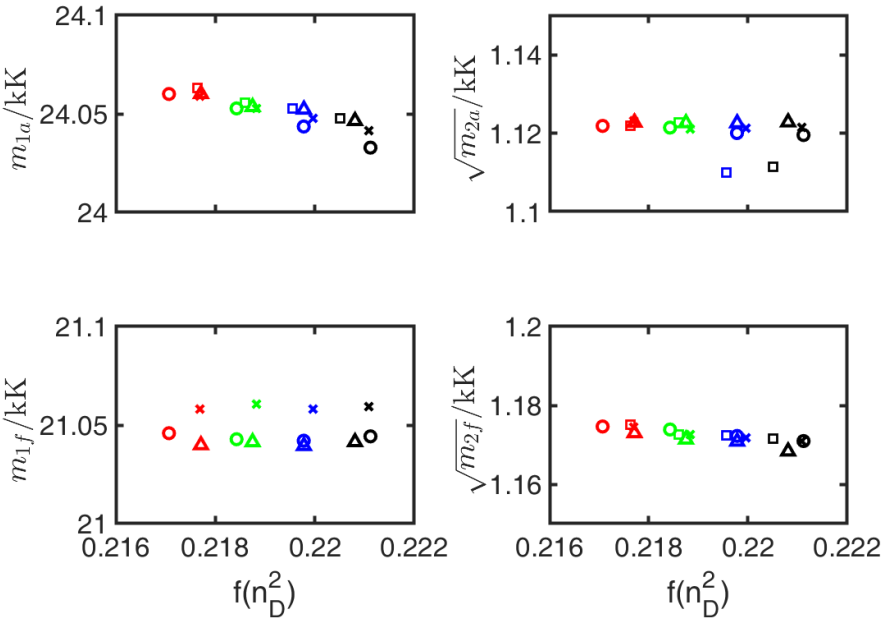

Figure 4.10: Band center and band width of Pe in DG mixtures absorption and fluorescence spectra at different temperatures and molar fractions of glycerol; black, blue, cyan and red colors stand for temperatures of 293.15, 303.15, 313.15 and 323.15 K, respectively; circle, cross, triangle and square stand for molar fractions of glycerol of 0.00, 0.35, 0.51 and 0.63, respectively. NOTE: The fluorescence band centers in the highest molar fraction of glycerol (square) are removed because the reabsorption correction cannot correct the spectra because the measured absorption spectra contains some background noise. The background noise comes from the dirty surface of the cuvette. The other quantities like band widths and peak positions are not affected.

However, despite all the former, the extract E_{00} values for different quencher concentrations, temperatures and solvent compositions are in a very narrow range if extracted from the peaks position and not from the m_1. The average E_{00} values for R6G and Pe in DG mixtures are 2.23±0.01 eV and 2.81 ±0.00 eV, respectively. These values are slightly lower than those in the literature[73, 157, 158]. The difference between this work and the references is

less than 0.04 eV or 1.6 times k_BT. This difference gives the deviation of the free enthalpy at the contact $\Delta G(\sigma) \sim 12\%$. The $\Delta G(\sigma)$ of R6G-DMpT and Pe-DMpT are $\sim$ -0.49 and -0.34 eV, respectively. The calculation of the free enthalpy $\Delta G(r)$ in eq. (2.17) takes a specific E_{00} value for each temperature and molar fraction of glycerol. Moreover, there is no sign of the ground state reactions for both studied systems and the spectra of the quencher doesn't overlap with that of the fluorophore.

4.2.1.2 Determination of the electron transfer parameters

Three electron transfer parameters – contact distance σ, coupling matrix element V_σ and decay length L – are extracted using the kinetic equation in eq. (2.15) and the reactivity in eq. (2.19) to fit with the steady state and time resolved fluorescence quenching results. Both experimental findings are related the theory through eq. (2.14). The relative quantum yield $\phi(0)/\phi(c)$ is extracted from the steady state experiments and the excited state population decay is extracted from both time resolved experiments.

The relative quantum yield $\phi(0)/\phi(c)$ is calculated from the absorbance at the excitation wavelength A and the integrated area of the fluorescence spectrum F. For the absorbance at the excitation wavelength below 0.1, the formula is given by

$$\frac{\phi(0)}{\phi(c)} = \frac{F(0)}{F(c)}\frac{A(c)}{A(0)}. \tag{4.2}$$

This quantity in eq. (2.15) and eq. (4.2) is a dimensionless function of the quencher concentration. A plot of the relative quantum yield against the quencher concentration is known as the Stern-Volmer plot or SV plot.

In order to compare the time resolved experimental results with the excited state population decay from the theory, a time dependent function is defined as[32]

$$R(t) = -\frac{1}{c}\ln\left(\frac{N(t,c)}{N(t,0)}\right) \tag{4.3}$$

where $\frac{N(t,c)}{N(t,0)}$ is the excited state population ratio in the absence and presence of the quencher. $R(t)$ function starts from zero value and decreases with time. Though, the definition of this quantity is straight forward to be applied to the experimental results, taking the ratio of the decay with quencher divided by the one without quencher, the extraction of this function from the experiment is prone to error because of the different rising times of the kinetics. To avoid this time zero mismatch, the decay curve is normalized to the unity. Then, the time at 50% of the rising edge is set to zero as shown in fig. 4.11.

The $R(t)$ function obtained from both time resolved measurements, FOG

and TCSPC, are in different time windows which are 0.1 ps - 1.2 ns and 0.4 - 38 ns. Be aware that the ns-time resolved measurements does not give the information from the beginning of the reaction. Therefore, a time matching between both experiments is needed. There is an overlapping region around 0.4 - 1.2 ns. We use this region to match both results. The difference between both experiments is a normalization factor of $N(t,c)/N(t,0)$. As the relationship between $N(t,c)$ and $R(t)$ is logarithmic, this normalization factor is a sum term for $R(t)$. The final R(t) is an average of all the measurements performed in each case (3 quencher concentrations in FOG and 18 in TCSPC).

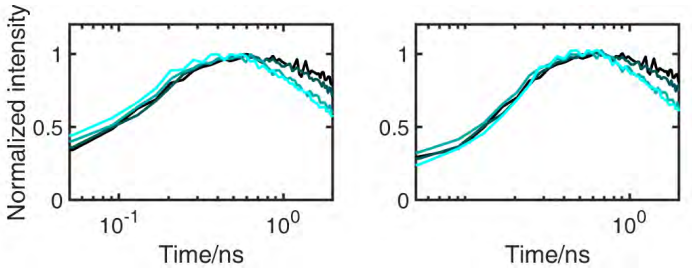

Figure 4.11: (left) Normalized fluorescence decays obtained from TCSPC measurements (right) after setting time zero at the 50% of the rising edge. The quencher concentration increases from black to cyan.

The relative quantum yields extracted from the steady state measurements and the $R(t)$ functions by the centrosymmetric differential encounter theory, see section 2.1 and the Marcus theory, see section 2.2.1. In the calculations, the distance and time limits are set large enough to reach the steady state: 10000 times σ and 10000 times τ_0, respectively. The calculations require the solvent properties in section 3.1.2 and the solute properties in table 3.1. The fitting results are shown in fig. B.9 and fig. 4.13. For the rest of DG mixtures at all temperatures see section B.3. The electron transfer parameters obtained from the fitting are summarized in table 4.3.

Table 4.3: A summary of the electron transfer parameters used in the fitting to the experimental results with eq. (2.15)

	R6G-DMpT	Pe-DMpT
σ/Å	8.5	8.9
$\hbar\omega$/eV	0.186	0.186
λ_q/eV	0.23	0.23
E_{00}/eV	2.21 - 2.23	2.81
V_σ/meV	26	40
L/Å	1.5	1.7

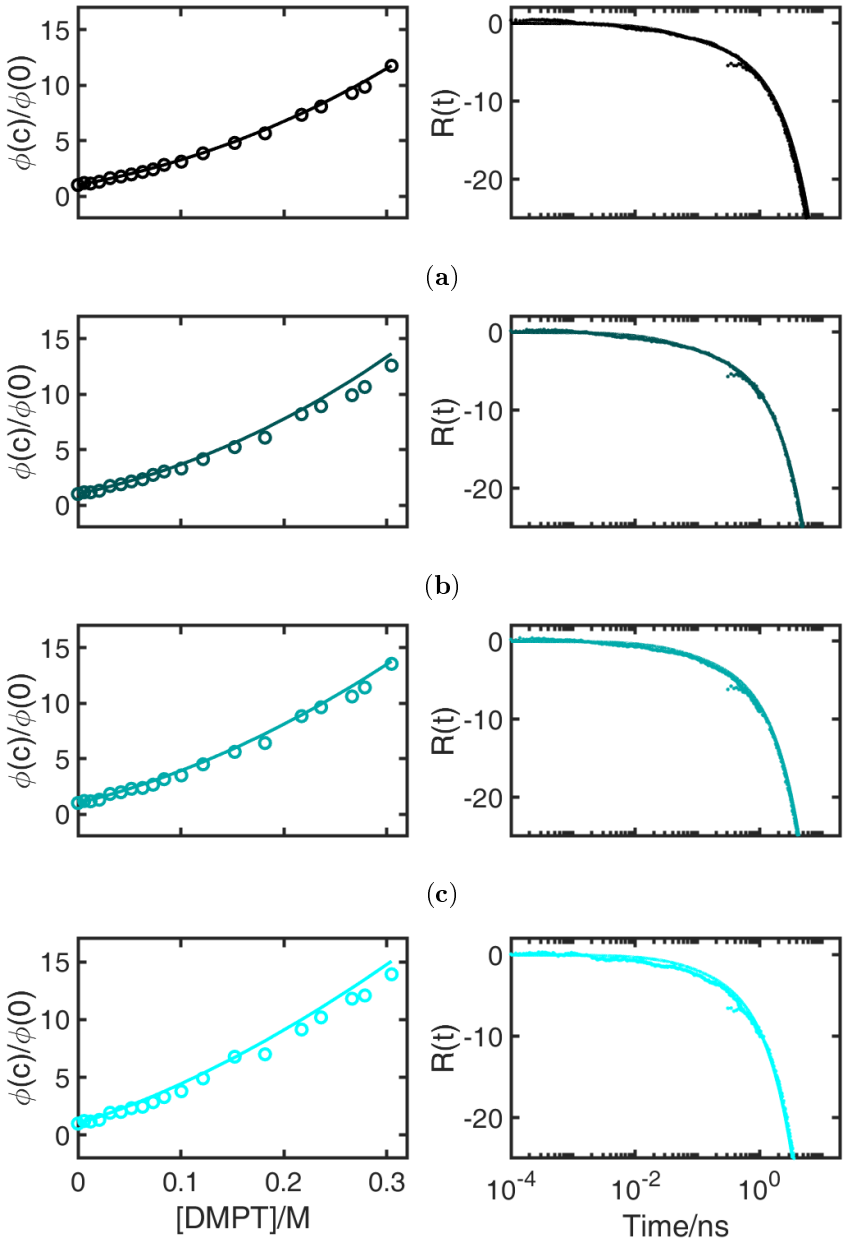

Figure 4.12: Comparison between (circle) experiments and (line) calculations using (left column) SV plots and $R(t)$ functions for R6G-DMpT quenching in DMSO at four temperatures, increasing temperature from black to blue.

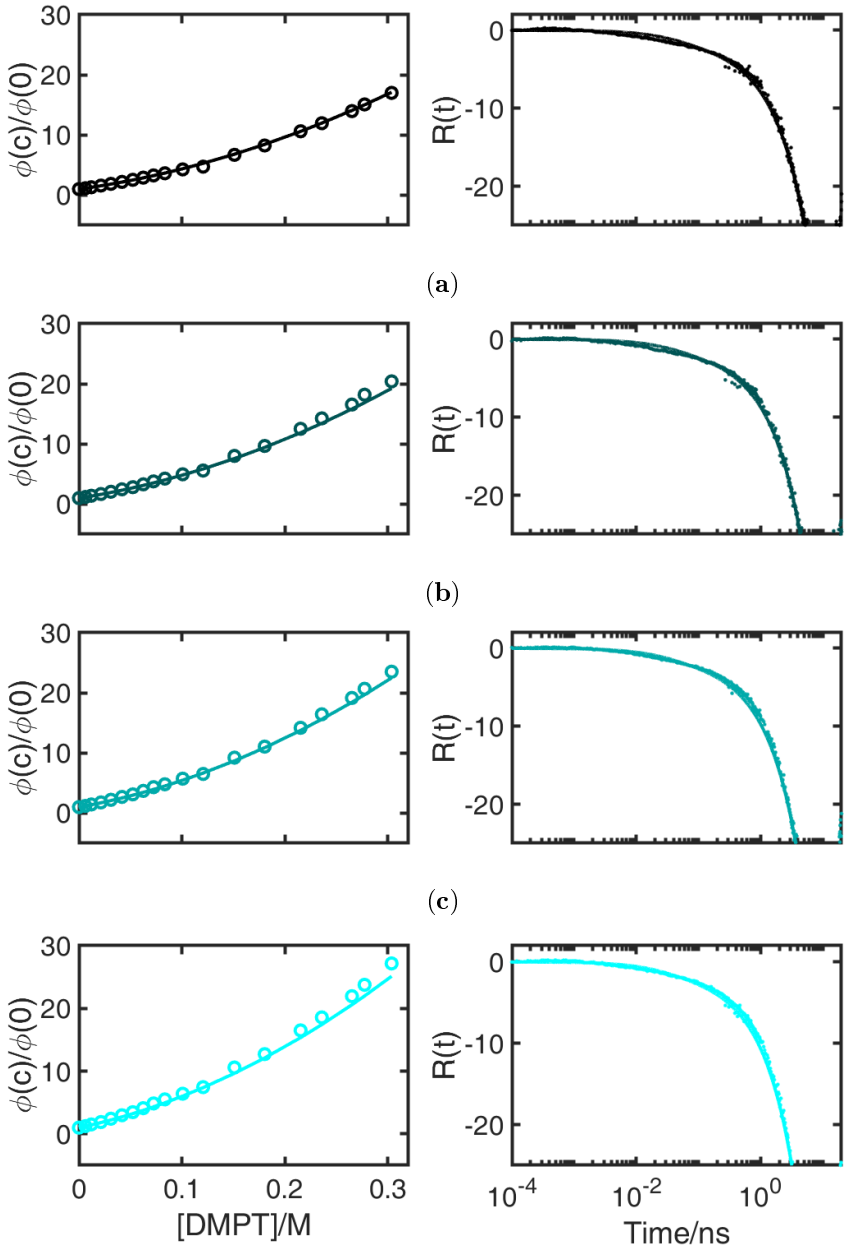

Figure 4.13: Comparison between (circle) experiments and (line) calculations using (left column) SV plots and $R(t)$ functions for Pe-DMpT quenching in DMSO at four temperatures, increasing temperature from black to blue.

All calculations agree well with the experiments. In some samples, there is a deviation of the solvent reorganization energy, less than 10%. This uncertainty could be originated from many parameters including refractive index, dielectric

constant, solvent relaxation time and electrochemical potential which are not measured in this work at all temperatures, but extrapolated from the known values. Moreover, the Marcus reorganization energy is a rough approximation as exemplified by the Matsuda's empirical expression[159] or further discussed by Matyushov[69, 160, 161]. The Marcus reorganization energy tends to be lower than the Matsuda's one as it is observed in this study.

There are three variables for the study of the reactions in DG mixtures, namely molar fraction of glycerol, temperature and quencher concentration. The increasing of the molar fraction of glycerol mainly increases the solution viscosity, while the other solution properties slightly change. On the other hand, the increasing temperature affects many solvent properties as described in section 3.1.2. The refractive index, dielectric constant and density change linearly with the temperature, while the viscosity changes exponentially with the temperature. Therefore, the changes in the temperature and molar fraction of glycerol mainly affect the solution viscosity. The observed quenching rate constant mainly depends on the solution viscosity. The diffusion coefficient is inversely proportional to the viscosity as described in eq. (2.5). When the diffusion coefficient gets smaller, this means the quencher molecules move slower to hit the target or the reaction happens less often. It is clear from the Stern-Volmer plot that the relative quantum yield deviates from linearity when the quencher concentration increases. This deviation can be explained by the kinetic equation in eq. (2.14). In order to have a linear relationship between the relative quantum yield and the quencher concentration, the quencher concentration has to be small. The derivation of this conclusion is shown in the literature[162]. The data points measured from both reacting systems become more scattered when the molar fraction of glycerol increases. Not all the samples were measured in the same cuvette. The experimental noise is therefore most likely related to the sample preparation rather than to the temperature control or the noise in the recording of the fluorescence. Nevertheless, for each of the reacting systems just three free parameters explain measurements at 18 quencher concentrations in 4 viscosities at 4 temperatures.

All fitted curves shown in fig. B.9 and fig. 4.13 and in section B.3 are the best fits using the parameters in table 4.3 to explain the experiential results. The sensitivity of each parameter including σ, V_σ and L to the reaction-diffusion model is discussed in Ref. [162] and [163]. According to the previous studies, these three parameters are strongly correlated. They can be compensated each other to explain the steady state results as the covariance matrix shows off-diagonal elements different from zero. For example, a small V_σ is compensated by a big L. However, the sensitivity of the fast time resolved experiments to the different parameters is different, meaning that it is possible to narrow down to a very small set of triads by considering both steady state and time resolved measurements. Therefore, a comprehensive study of the

reaction kinetics needs also the fast time resolved technique. Another set of electron transfer parameters involve the reactant structure. The C-H stretching quantum mode for organic fluorophores is applied in this calculation see table 4.3[32]. A single channel electron transfer is applied to couple with this vibration because the Huang-Rhys factor is close to one. This vibrational mode can be seen as average configuration of the reactants at the crossing point of two potentials.

The electron transfer parameters obtained in this work are coherent with previous reports. In the case of Pe-DMpT, the values of electron transfer parameters in this study are comparable to those obtained in the Ref.[32] and [73]. Only the reactant contact distance in this study is bigger by 12%. In the case of R6G-DMpT, the parameters are comparable with those obtained in previous studies using R6G-DMA and R3B-DMA[164, 165]. The reports give the values for the coupling element $\sim$ 25 - 37 meV, for the decay length 1 Å and the contact distance 6.9 Å. The small contact radius and short decay length are probably due to the lack of the solvent structure. It was shown in Ref. [163] that the lack of the short range potential can be compensated by these parameters.

Comparisons of the reaction kinetics between both systems are shown in fig. 4.14. According the electron transfer parameters, the quenching reaction of Pe-DMpT is faster. This is reasonable because the coupling matrix element and decay length are bigger. The comparison is shown in the $R(t)$ plot in DMSO. This difference in the static quenching is suppressed when the viscosity becomes large. The reaction is diffusion controlled as shown in the left panel of fig. 4.14.

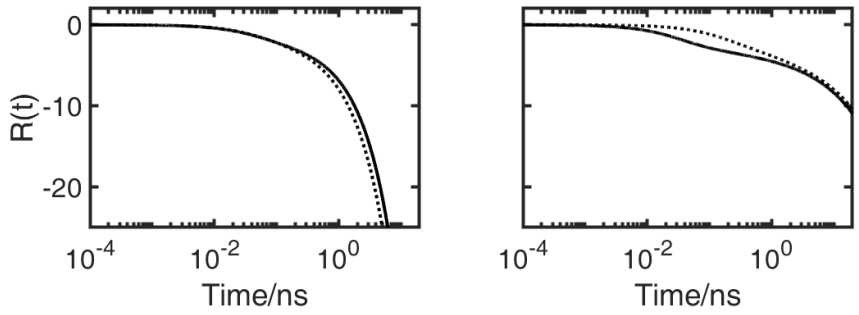

Figure 4.14: $R(t)$ of (line) R6G-DMpT and (dot) Pe-DMpT in (left) DMSO and (right) the highest viscosity at 293.15 K

The effects of the temperature and molar fraction of glycerol on the reaction kinetics are discussed in terms of the viscosity using the $R(t)$ function from the theory that reproduce best the experimental results. Comparisons

of $R(t)$ at different temperatures and molar fractions of glycerol are shown in fig. 4.15. The kinetics becomes slower when the viscosity increases. The slower kinetics can be seen by the extension of $R(t)$ function to the longer time. This slow kinetics is observed for both reacting studied systems.

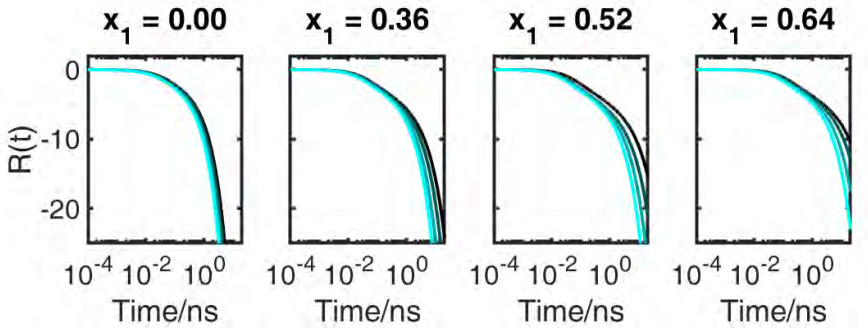

(**a**)

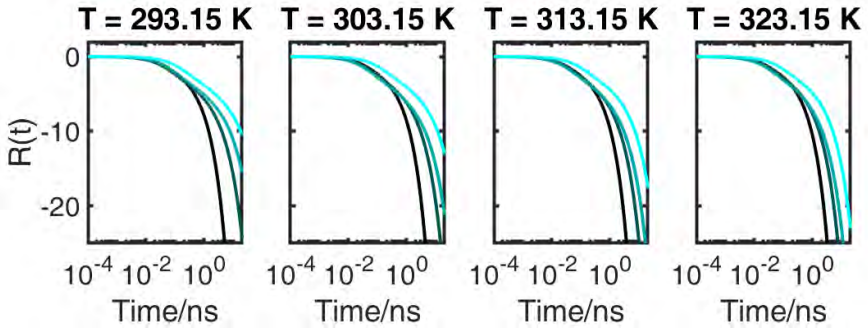

(**b**)

Figure 4.15: $R(t)$ obtained from the calculations of Pe-DMpT in DG mixtures at different temperatures and molar fractions of glycerol (x_1); From black to blue lines represent the (a) increasing temperature and (b) increasing molar fraction of glycerol.

Another validity test of the diffusion-reaction model can be done by further comparing the ns-time resolved data with the steady state data. The rate coefficient at long time can be approximated to follow the rate coefficient obtained from the Smoluchowski model in eq. (2.1) using a quenching radius R_q instead of the contact radius.. The convolution fitting of IRF and eq. (2.14) using the rate coefficient obtained from eq. (2.1) with the ns-time resolved results at the limit of the encounter diffusional time, $t \geq R_q^2/D$, gives a pair of $R_q - D$[162]. On the other hand, $R_q - D$ pairs can be estimated from the Stern-Volmer plots by taking the pair distribution function at infinite time that best reproduces

them. The quenching radius is calculated by

$$\begin{aligned} R_q =& \frac{k_\infty}{4\pi D} \\ k_\infty =& 4\pi \int_\sigma^\infty r^2 w(r) n(r,\infty) dr \end{aligned} \tag{4.4}$$

where $n(r,\infty)$ is the pair correlation function at the steady state and D is taken from the fitting input. In fig. 4.16, the $R_q - D$ pairs from the ns-time resolved and steady state results are in good agreement. The diffusion coefficients for Pe and R6G are different reflecting the differences in sizes and the dielectric friction present only for the latter.

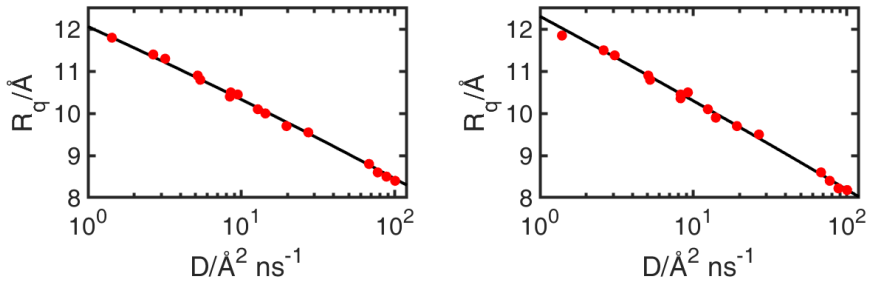

(**a**) (**b**)

Figure 4.16: Plots of quenching radii as a function of diffusion coefficients obtained from (line) steady state results and (circle) ns-time resolved measurements, (a) R6G-DMpT and (b) Pe-DMpT. All viscosities and temperatures have been used to construct this figure.

4.2.2 Fluorescence quenching in liquid crystals

In this section, the fluorescence quenching in liquid crystals studied by means of steady state and time resolved spectroscopic techniques is presented. The order parameter was extracted to quantify the anisotropy of the medium above and below the nematic-isotropic transition temperature using polarized absorption spectroscopy. The steady state absorption and fluorescence spectra were used to extract the E_{00} values. The fluorescence lifetimes were used to estimate the steady state quenching rate constants k_∞. The steady state rate constants are compared for the isotropic and anisotropic media. Then the three mentioned models in section 4.2 making use of the electron transfer parameters obtained from the study in DG mixtures were applied to explain the results. The performance of each of the models is discussed and a rationale provided to understand chemical reactions in anisotropic media.

4.2.2.1 Characterizations of reacting systems in liquid crystals

The anisotropy in dye-liquid crystals mixtures can be quantified by the order parameter S_A[143]. The order parameter was measured using the method described in section 3.2.2. The order parameter indicates the alignment of fluorophores in LCs. This clue can be used to set the excitation polarization. The polarized absorption measurements were performed for R6G and Pe in DMSO and 5CB at 293.15 and 323.15 K. These temperatures were selected as they are equally distributed around the transition temperature. The results are summarized in table 4.4. The order parameters of both in nematic phase is clearly higher than in the isotropic phase as well as in DMSO. The order parameters in the nematic phase of Pe is slightly higher than the one in R6G. This should come from the rigid structure of Pe without mobile moeity and the neutral electronic charge.

The smaller values obtained than the order parameter from the simulation in the nematic phase, 0.73 see section 3.1.2, may be due to several reasons: either the dyes are not perfectly aligned with the nematic director or the orientation of the liquid crystal with the polarization plane of light in the POM measurement is not perfect. In any case these results show that there is a preferred orientation of the dyes within the nematic LC. Despite the reports of existence of nematic domains above the transition temperature, these results do not show any hints of them. This does not mean they are not present. In fact, as provided in the experimental section the value of the order parameter obtained from the simulation in the isotropic phase is 0.06. This is a consequence of the short range order induced by the molecular shape of the mesogens[166]. Again, the much smaller value from the POM measurements of the dyes may mean any of the two things above exposed.

Table 4.4: Order parameters of R6G and Pe in DMSO and 5CB at 293.15 K and 323.15 K

Samples	Order parameter	
	293.15 K	323.15 K
R6G in DMSO	0.00±0.00	0.00±0.00
R6G in 5CB	0.21±0.00	0.01±0.01
Pe in DMSO	0.00±0.00	0.00±0.00
Pe in 5CB	0.26±0.00	0.00±0.00

The measured absorption and fluorescence spectra in LCs were processed to remove the background according to the procedures mentioned in section 3.2.2 and section 3.2.3. The spectra were transformed into TDM representation in order to get the E_{00} values in the same manner as mentioned in section 4.2.1.1. The E_{00} values for R6G in the nematic and isotropic phases are 2.21 and 2.22 eV, respectively. For Pe in the nematic and isotropic phases, the values are 2.78 and 2.79 eV, respectively. The values in LCs of both dyes similar to those found in the DG mixtures. The average dielectric constants and refractive indices do not change much with the temperature. On the contrary, the absorption and fluorescence band centers and band widths shift towards higher energies as the temperature increases while the polarization function decreases as shown in fig. 4.17 and fig. 4.18. This effect has been reported in the literature[167, 168, 136]. This blue shift is is at odds with the solvent polarization function calculated from the average values of the dielectric constants and the refractive indices. Comparing the solvatochromism of both dyes in DG mixtures, increasing solvent polarization function causes red shift[156]. A possible explanation for this is that the solvation energy in the nematic phase is anisotropic and it is much higher than the energy calculated from the average values. For example, the parallel dielectric constants in the nematic phase is 20, while the average value is 10.7.

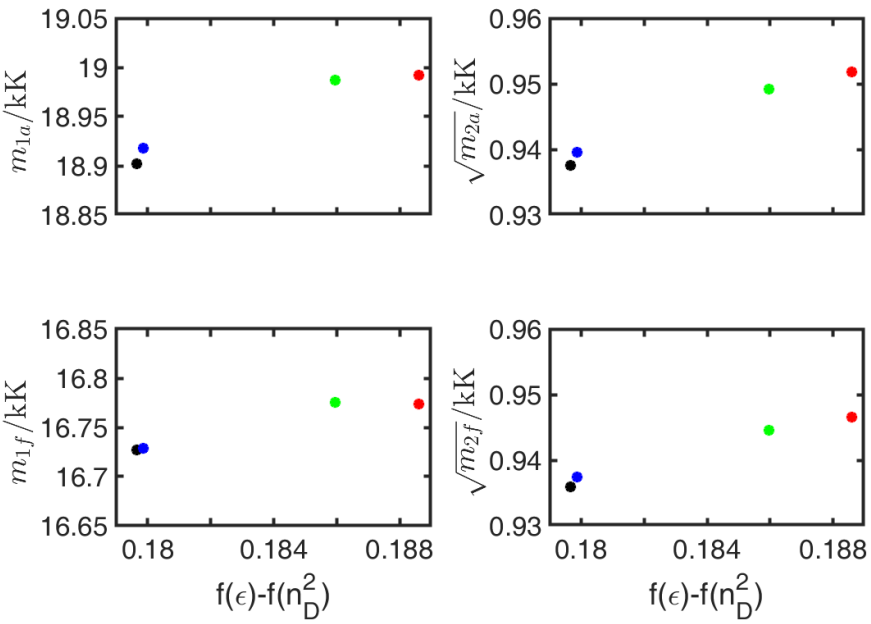

Figure 4.17: The absorption and fluorescence spectral moments of R6G in 5CB at 293.15, 303.15, 313.15 and 323.15 K, black, blue, cyan and red, respectively

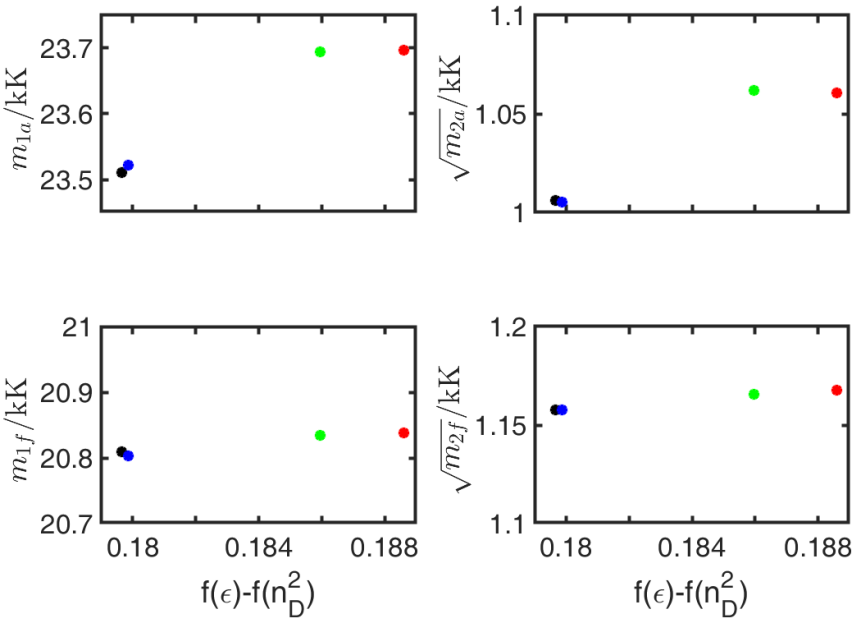

Figure 4.18: The absorption and fluorescence spectral moments of Pe in 5CB at 293.15, 303.15, 313.15 and 323.15 K, black, blue, cyan and red, respectively

The relative quantum yield equation in eq. (4.2) is modified to correct for the absorbance > 0.1. The relative quantum yield with the full expression for the absorbance reads

$$\frac{\phi(0)}{\phi(c)} = \frac{F(0)}{F(c)} \frac{\left(1 - 10^{-A(c)}\right)}{\left(1 - 10^{-A(0)}\right)}. \tag{4.5}$$

The fluorescence decays from the ns-time resolved measurements were fitted with the convolution of the IRF and a multi-exponential function. The steady state quenching rate constant k_∞ can be obtained from the slowest decay component of the fluorescence τ_{long}:[32]

$$\frac{\tau(0)}{\tau_{long}(c)} = 1 + k_\infty \tau(0) c. \tag{4.6}$$

We can use this quantity to compare the quenching reactions between liquid crystals and normal solvents.

The quenching results in DG mixtures at 293.15K and viscosity of 47 cP are selected as shown in fig. 4.19. The visocosity of 5CB at the perpendicular direction to the nematic director is 52 cP and 28 cP in the parallel one at the same temperature. While for R6G-DMpT the long decay times, and therefore the steady state rate constants, are almost identical in 5CB and in this DG

mixture, in the case of Pe-DMpT the quenching is faster in the later solvent. This difference in behavior may be related to the difference in nature of the electron transfer -charge shift in the R6G-DMpT case and charge separation in that of Pe-DMpT. There must be something intrinsically different in the way the LC responds to the charge redistribution in the intermolecular reaction. As we will see later, this may be taken into account by modifying the reorganization energy. This analysis of the quenching reactions is very crude. A more comprehensive shall be done using the three diffusion-reaction models.

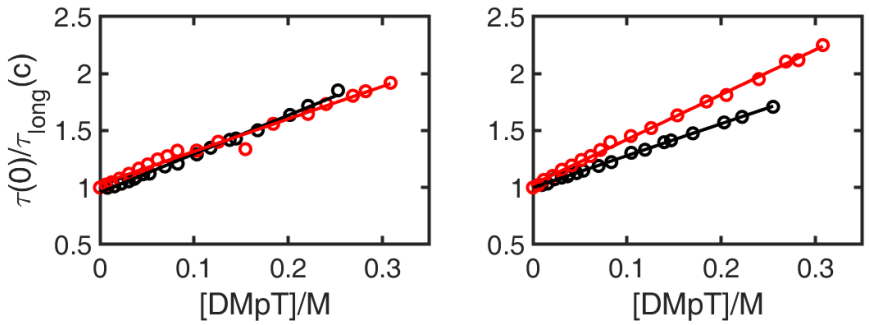

Figure 4.19: The Stern-Volmer representation of the slowest fluorescence decay (circle) obtained from (left) R6G-DMpT and (right) Pe-DMpT in (black) the nematic phase and (red) the DG mixture which has viscosity of 47 cP at 293.15 K; the line represents k_∞ obtained from eq. (4.6).

4.2.2.2 Comparisons of the diffusion-reaction models with the experiments

The three mentioned models were applied to explained the results from the steady state and two time resolved measurements. For all three models, three electron transfer parameters, zero vibronic transition energies, electrochemical potentials and solvent properties are fixed parameters. The electron transfer parameters are taken from the fluorescence quenching experiments in DG mixtures as described in section 4.2.1.2. The zero vibronic transition energy is estimated from the steady state spectra as mentioned earlier in section 4.2.2.1. The electrochemical potentials of the solutes and the 5CB properties are provided in the two sections of the experimental chapter which are section 3.1.1 and section 3.1.2. The distance and time limits are set large enough to reach the steady state as mentioned in the DG mixture experiments, section 4.2.1.2. There is one remaining parameter for the calculation of the electron transfer reactivity which is the solvent relaxation time τ_L. The solvent relaxation time τ_L is set as a free parameter. Even though there are many reports of this quantity using dielectric spectroscopy, Kerr effect transient optical grating and time resolve fluorescence spectroscopy[134, 169, 136], there is no clear indication for

the relaxation time which corresponds to the electron transfer in the nematic and isotropic phases. Moreover, most of the experiments were performed in the isotropic phase or few degree Celsius above the transition temperature. The relaxation dynamics of liquid crystals consists of multiple components as mentioned in section 3.1.2. Moreover, the solvent relaxation time is used to estimate the dielectric friction in eq. (2.5). These quantities enter into the three models differently depending on the definition of each model. The description of each model and the quantities related to the simulations are provided in the next paragraph.

The IC model is the isotropic diffusion with centro-symmetric reactivity model IC. The diffusion-reaction equation is defined in eq. (2.2). In this equation, the isotropic diffusion operator requires a diffusion coefficient and an interaction potential between the reactants. The diffusion coefficient is calculated from the Zwanzig equation in eq. (2.5) using average quantities of 5CB. The potential is taken from the MD simulations as described in section 3.1.2. The potential in the plane which is perpendicular to the the director or $\theta = 90°$ is taken because of the following reason. The packing order in this plane is higher than others and the molecular diameter of 5CB is similar to those of DG mixtures, 3.6Å. The isotropic reactivity $w(r)$ is evaluated by eq. (2.19). The isotropic reactivity is used as a reference point to estimate the anisotropic effect. The average solvent properties are applied for this calculation. The AC model is the anisotropic diffusion with centro-symmetric reactivity model AC. The diffusion-reaction equation defined in eq. (2.2) is applied. The only difference lies in the diffusion operator. The anisortropic diffusion operator defined in eq. (2.43) requires two diffusion coefficients and one potential surface. The two diffusion coefficients are calculated from the viscosities parallel and perpendicular to the director, $\eta_{\|}$ and $\eta_{\perp}$, respectively. The potential surface in this case is a function of distance r and angle θ. In this study, we use the spherical coordinate which is derived from the cylindrical symmetry of the diffusion coefficients as discussed in section 2.4.1. The potential surface is calculated from the pair correlation function $g(r, \theta)$ as mentioned in section 3.1.2. The reactivity is exactly the same as mentioned in the IC model. The AA model is the anisotropic diffusion with asymmetric reactivity model AA. The diffusion-reaction equation is defined in eq. (2.44). The diffusion operator is defined exactly the same as in the AC model. The anisotropic reactivity in this model takes the anisotropic reorganization energy as described in section 2.4.2. The anisotropic reorganization energy in eq. (2.47) requires the anisotropic solvent properties and the second order Legendre polynomial function $P_2(\cos\theta)$. This $P_2(\cos\theta)$ fucntion represent the orientation of the liquid crystals molecules or dipole particles in the nematic phase[13].

For a first approximation, we try to obtain good fits between the experiments and three models using different τ_L values. The good fit means a set

of τ_L which gives coherent results between the simulations and three experiments. The Stern-Volmer plots and the $R(t)$ plots are employed to compare the simulations to the experiments. The data extraction for both quantities is performed the same as in the DG mixtures. Both plots of R6G-DMpT and Pe-DMpT in 5CB are shown in fig. 4.20 and fig. 4.21. The simulated results from three models fit equally well to the experiments. The fitting parameters τ_L using in each model are summarized in table 4.5. The comparisons and discussion of the relaxation times obtained from three models are provided in the next paragraph.

Table 4.5: The solvent relaxation times τ_L obtained from the fitting of IC, AC and AA models to the experiments using the same reorganization enregy for both systems

Temperature/K	τ_L/ps					
	IC		AC		AA	
	PD	RD	PD	RD	PD	RD
293.15	25	25	35	35	70	70
303.15	35	10	35	20	50	20
313.15	48	20	48	20	*	*
323.15	30	15	35	15	*	*

NOTE: PD is Pe-DMpT and RD is R6G-DMpT
* the same value as in model AC

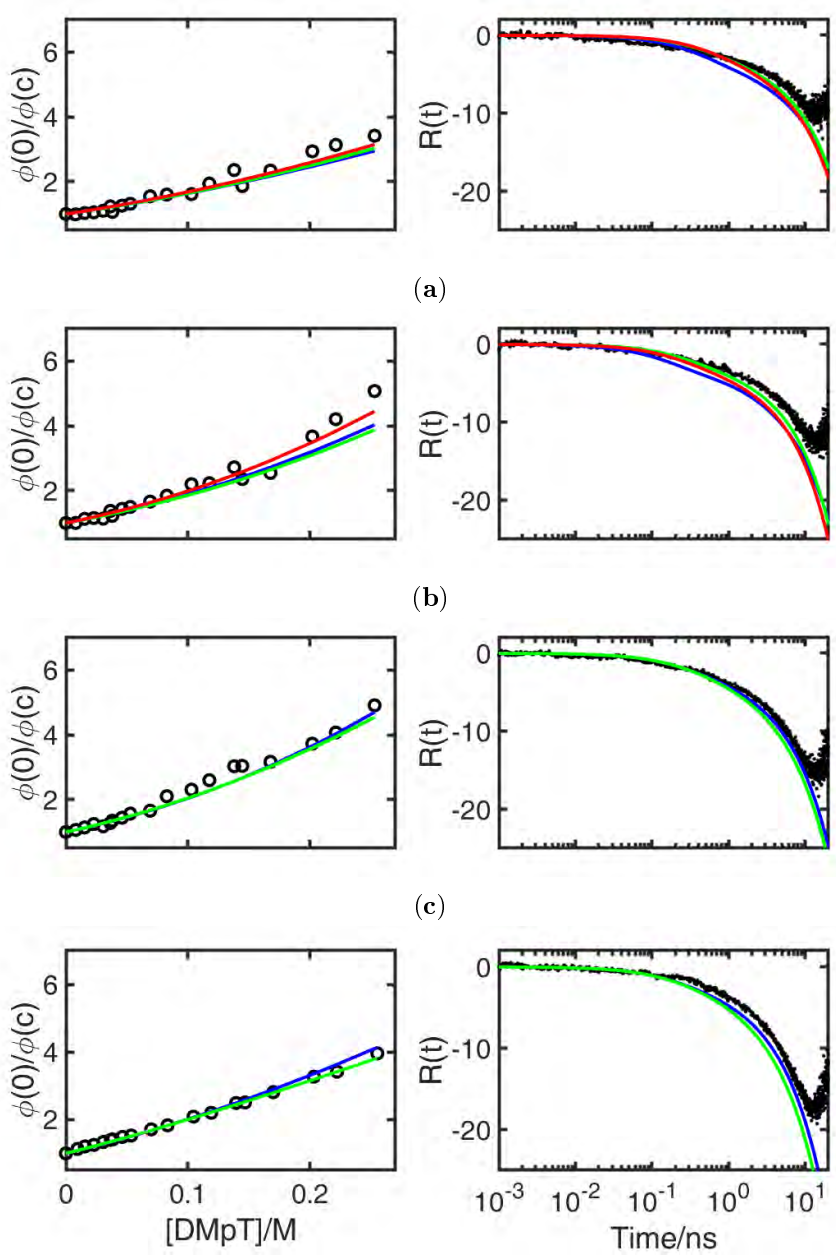

Figure 4.20: (left column) $\phi(0)/\phi(c)$ and (right column) $R(t)$ plots of R6G-DMpT in 5CB obtained from (black circle) the steady state measurements, (blue line) IC simulations, (cyan line) AC simulations and (red line) AA simulations at four temperatures, (a) 293.15 K, (b) 303.15 K, (c) 313.15 K and (d) 323.15 K. Note: Three data points at high quencher concentrations in the SV plot at 303.15 K are removed because the samples are in the isotropic phase.

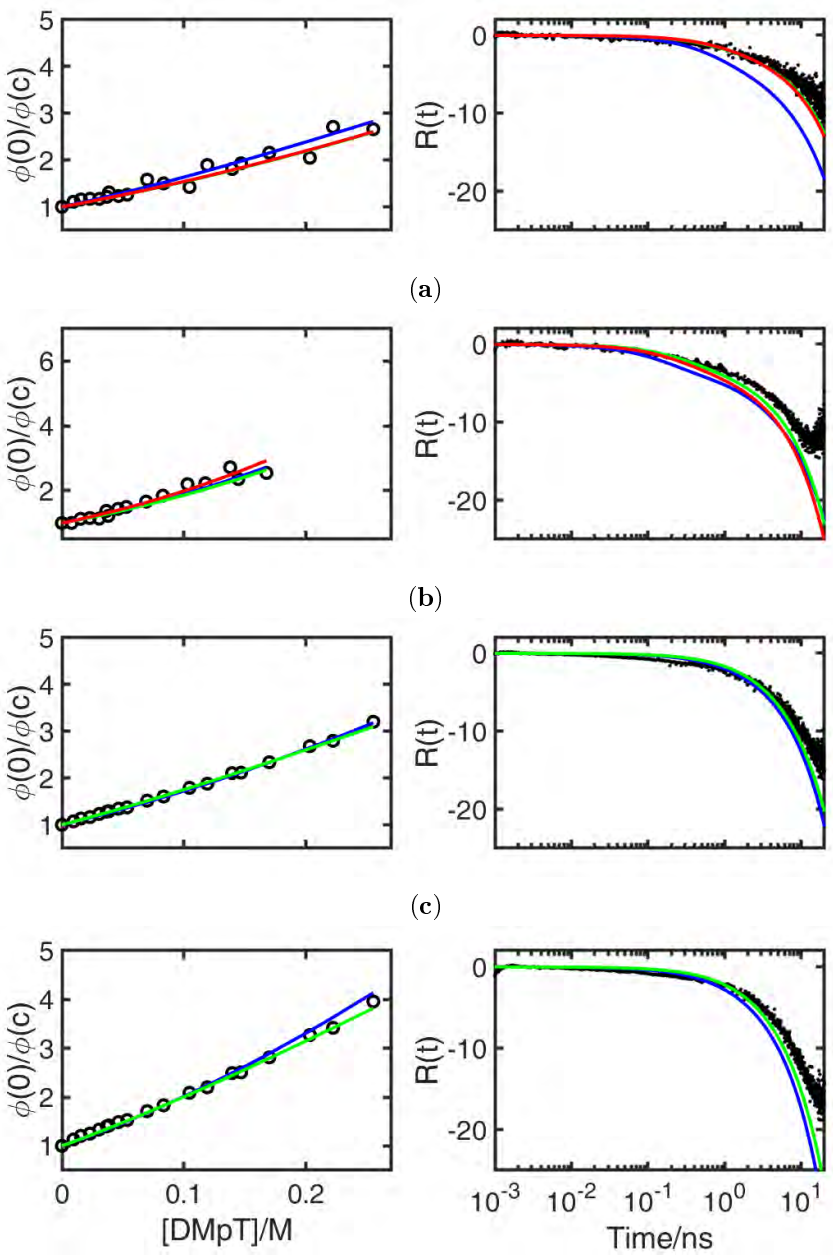

Figure 4.21: (left column) $\phi(0)/\phi(c)$ and (right column) $R(t)$ plots of Pe-DMpT in 5CB obtained from (black circle) the steady state measurements, (blue line) IC simulations, (cyan line) AC simulations and (red line) AA simulations at four temperatures, (a) 293.15 K, (b) 303.15 K, (c) 313.15 K and (d) 323.15 K. Note: Three data points at high quencher concentrations in the SV plot at 303.15 K are removed because the samples are in the isotropic phase.

The discussion of the relaxation times are divided into two parts which are the comparison between the models and within a model. First, the relaxation times obtained from the IC and AC models do not show a correlation with the temperature, while there is a decreasing trend in the AA model. Moreover, the relaxation times from both models are similar. This indicates that the anisotropic diffusions might not be significant for both systems. The dielectric relaxation measurements of 5CB shows a decreasing relaxation time with the temperature[134]. The temperature dependence of the relaxation time is explained by the decreasing order. In the report, the ratio between the relaxation time in the nematic phase to the isotropic phase is ~ 1.4 which is similar to value obtained from the Pe-DMpT in the AA model. The solvent relaxation times in this study are 10 - 70 ps which is coherent with the previous report[47, 25]. The transient grating optical Kerr effect measurements in 5CB near the transition temperature has revealed fast components of the relaxation process which are 1 - 300 ps. Second, the relaxation times obtained from the Pe-DMpT is higher or equal to the ones obtained from the R6G-DMpT regardless of the models. This difference may be originated from the different type of the electron transfer reactions as discussed in section 2.4.2. The ratio of the relaxation times between both systems are 2 - 3. As both systems happen in the same solvent, the relaxation time should be identical and this difference may be compensated by a modification of another property like the reorganization energy.

As both systems occurs in the same solvent, we assume that there is a single solvent relaxation time needed to explain the experiments. In order to do that, a set of the solvent relaxation times obtained from the Pe-DMpT is applied to the R6G-DMpT. Then, the reorganization energy for the latter reaction is left as a free parameter. The fitting results are equally good as in the Pe-DMpT results. The fitting results are listed in table 4.6. It is clear from the results that the reorganization energy in the case of R6G-DMpT deviates from the Pe-DMpT by $\sim 15\%$. As we have seen that the same τ_L can be applied for both systems with a slight modification of the reorganization energy, the introduction of the anisotropic diffusion and reactivity is not necessary to explain the experiments individually. However, as mentioned above the experimental findings about the relaxation times by other means reveal a decrease of this quantity with temperature[134, 47, 136]. In model IC, it does not follow this trend. Model AC neither. Only model AA is coherent with these mentioned data. Therefore the conclusion is straight forward: the anistropic structure, diffusion and reactivity are needed to congruently explain all the results together. The difference in the reorganization energies is discussed later. In order to understand how models with partial or no anisotropy are able to explain isolated measurements, we are now discussing the sensitivity of the AA model to anisotropy.

Table 4.6: The solvent relaxation times τ_L and ratio of the reorganization energy obtained from the fitting of IC, AC and AA models to the experiments

Temperature/K	IC		AC		AA	
	τ_L/ps	λ_s^F	τ_L/ps	λ_s^F	τ_L/ps	λ_s^F
293.15	25	1.00	35	1.00	70	1.00
303.15	35	0.85	35	0.90	50	0.90
313.15	48	0.85	48	0.90	*	*
323.15	30	0.90	35	0.90	*	*

NOTE: λ_s^F is the ratio of the reorganization energy of R6G to Pe
* the same value as in model AC

A qualitative study to estimate the influence of three factors, namely the diffusion coefficient, relaxation time and reorganization energy, is performed using the electron transfer parameters of Pe-DMpT in table 4.3. The anisotropic diffusion effect on the reaction is studied using the AC and AA models. The other two factors are fixed as $\tau_L = 35$ ps and $\lambda_s^F = 1$. The temperature is set at 293.15 K to have the liquid crystal in the nematic phase. Five pairs of diffusion coefficient ratio D_z/D_ρ are selected which are 0.2, 0.5, 1, 2 and 5. The diffusion coefficient are referred to the viscosity along the nematic director which is 28 cP. The diffusion coefficient ratio of 5CB in the nematic phase is ~ 2. The results are shown in fig. 4.22.

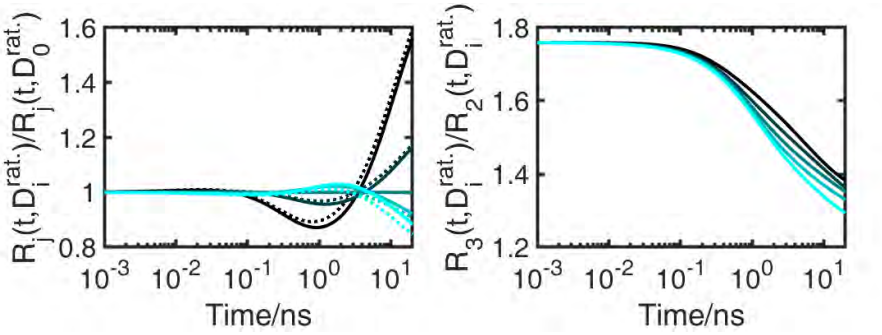

Figure 4.22: Simulated ratios of $R(t)$ obtained for five diffusion coefficient ratio $D_z/D_\rho = 0.2$, 0.5, 1, 2 and 5 with respect to that at 28 cP, D_z. T = 293.15 K, $\tau_L = 35$ ps and $\lambda_s^F = 1$. Left panel: Ratios of $R(t)$ for each model (line: AC, dash: AA) from 0.2 (black) to 5 (cyan) with respect to $D_z = D_\rho$ case. Right panel: The same data as in the left panel, but dividing $R(t)$ from the AA model by $R(t)$ from the AC model.

As the diffusion along the director is fixed, the decreasing D_ρ slows down the reaction rate coefficient only at long times. The same decreasing trend is observed for both models. The deviation of the reaction rate coefficient is ≤ 2,

while the diffusion coefficient ratio is 5. When comparing between two models, the difference lies in the reorganization energy. The reaction rate coefficient obtained from the AA model is always higher than the other one. This is due to the anisotropic reorganization energy. The changes in the diffusion coefficients slightly differ the reaction rate coefficient only after 0.5 ns. Even though, the anisotropic diffusion effect in the nematic phase $D_z/D_\rho \sim 2$ is not very large, it is still noticeable at times longer than 1 ns. Besides, both models provide similar trends in $R(t)$ for various ratios of D_z/D_ρ, which may be compensated simply by changing the reactivity through τ_L as the largest differences are found at short times, when the reaction is mostly influenced by the reactivity.

The effect of the relaxation times on the reaction is studied using the AC and AA models. The other two factors are fixed as $D_z/D_\rho = 2$ and $\lambda_s^F = 1$. The electron transfer parameters and the temperature are identical to the previous paragraph. Five relaxation times are selected which are 1, 10, 35, 70 and 100 ps. These values cover the relaxation times obtained in table 4.5. The results are shown in fig. 4.23. Interestingly, the change of the relaxation times from 1 ps to 100 ps increases the reaction rate coefficient by two orders of magnitude for both models. The reaction rate coefficient is affected more at the short time and less in the long time. When comparing between the AC and the AA models, the same observation like in the previous paragraph is seen. The higher reaction rate coefficient is obtained from the AA model.

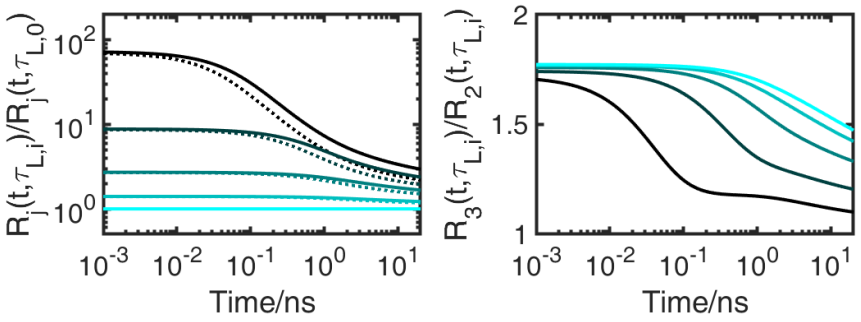

Figure 4.23: Plots of simulated $R(t)$ ratio obtained from five relaxation time which are 1, 10, 35, 70 and 100 ps using the (line) AC and (dash) AA models, T = 293.15 K, $D_z/D_\rho = 2$ and $\lambda_s^F = 1$; (left) the $R(t)$ ratio refers to the slowest time $\tau_{L,0}$ in each model; (right) the $R(t)$ ratio refers to the $R(t)$ in the AC model; j and i denote the model number (2 or 3) and relaxation time τ_L; the relaxation time increases from black to blue lines.

The third factor to be studied is the reorganization energy. This study aims to estimate the influence of the reorganization energy to the reaction rate coefficient without taking the other anisotropy effects. The electron transfer

parameters are identical to the two previous paragraphs. The other two factors are fixed as $\tau_L = 35$ ps and $D_z/D_\rho = 1$. The temperature is set at 323.15 K to have the liquid crystal in the isotropic phase. Only the AC models is employed in this comparison because in the isotropic phase the reorganization energy does not depend on the angle. The results are shown in fig. 4.24. The changes in the organization energy are about 10%, while the changes in the reaction rate coefficient are about 2 times. Moreover, the effect of reorganization energy starts from the short time and decreases with time. As the reorganization energy increases the reaction rate coefficient decreases.

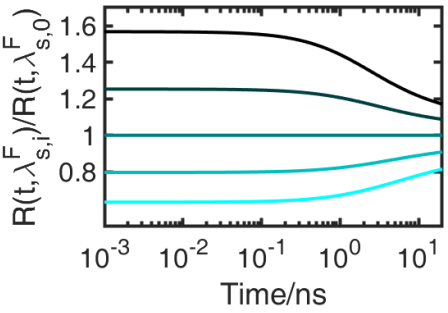

Figure 4.24: Plots of simulated $R(t)$ ratio obtained from five reorganization energy ratios which are 0.90 0.95 1 1.05 and 1.10 using the AC model, T = 323.15 K, $\tau_L = 35$ ps and $D_z/D_\rho = 1$; the $R(t)$ ratio refers to the case of $\lambda_s(\sigma)$ = 0.71 eV; i denote the reorganization energy ratio λ_s^F; the reorganization energy ratio increases from black to blue lines.

These three sets of calculations help us rationalizing how it is possible to explain the individual experiments with any of the three approaches presented: while the effect of anisotropic diffusion is relatively modest for the ratio of D_z/D_ρ in 5CB in the nematic phase, the changes observed when varying τ_L and λ_s are rather important. Moreover, compensation effects are possible as the trends allow for lifting the $R(t)$ dependencies (and in consequence the SV plots) in different time regions by a selection of a given set of parameters. However, and as mentioned above, the application of the least anisotropic models leads to parameters that show incongruent temperature trends.

Chapter 5

Conclusions

Two kinds of electron transfer reactions are employed in order to study the anisotropy effect in liquid crystals which are intramolecular and intermolecular electron transfer reactions. The study is also performed in DG mixtures as isotropic media for comparisons. The measurements have been performed at four temperatures around the transition temperature of 5CB, namely 293.15, 303.15, 313.15 and 323.15 K. Two kinds of the optical techniques are used to investigate the reaction kinetics which are the steady state and time resolved spectroscopy.

The intramolecular electron transfer reaction is studied using PeDMA in many solvents. Two elementary models, GSE and GLE, have been used to explain the experiments in isotropic solvents. The models require the thermodynamics of the system and the non-equilibrium dynamics of the solvation. Both requirements are needed to construct the potential energy surface and time dependent friction function. The models give time evolution of the emission to compare with the experiments. A good agreement between the models and the experiments is found in most of the solvents, though the GLE shows better agreement. In a series of measurements in DG mixtures at large viscosities both models failed. This was interpreted as a failure connected to the extraction of the time dependent friction function from the reference compound. The friction function was measured using C153 which felt different frictions in H-containing solvents, like in rich glycerol mixtures. PeDMA in 5CB samples were measured using the steady state and time resolved techniques. The absorption and emission spectra are similar to those in THF. Unfortunately, results obtained from the fluorescence up-conversion are too low quality. There are many problems related to the dye concentration and the limitations of the technique as mentioned in section 3.2.6. In order to continue on this study, one would need to improve the S/N ratio of this measurement.

The intermolecular electron transfer reaction is studied using R6G and Pe as acceptors and DMA as a donor. The fluorescence quenching in the excited

state is employed to track the reaction kinetics. The study was performed in two solvents and four temperatures as mentioned before, DG mixtures and 5CB. First, both systems are studied in DG mixtures as a reference to have the electron transfer parameters. Three electron transfer parameters are extracted from the measurements in DG mixtures at different temperatures including the contact distant σ, coupling matrix element V_σ and decay length L. The theoretical predictions fit well with the steady state and time resolved experimental results for both systems in 4 DG mixtures, 4 four temperatures and 18 quncher concentrations. This coherence between the two kinds of the experiment validates the parameters.

The study of the fluorescence quenching in liquid crystals was performed in two steps – estimate the anisotropy and explain the results using three models. For the anisotropy of the samples in liquid crystals, the order parameters are 0.21 and 0.26 for R6G and Pe in the nematic phase and become zero in the isotropic phase. In addition, the steady state quenching rate constant k_∞ obtained from the slowest fluorescence decay time in Pe-DMpT is faster in the DG mixture than the nematic solvent at the same viscosity, while there is no difference for the steady state quenching rate constant in R6G-DMpT for both solvents. In order to explain the experimental results in liquid crystals, the anisotropic diffusion model and the anisotropic reactivity are developed together with numerical calculations based on MOL. The electron transfer parameters obtained from the reactions in DG mixtures are applied to the three diffusion-reaction models, namely IC, AC and AA (the description of each model refers to section 4.2.2.2). Due to the diverse values of the reported solvent relaxation times[134, 169, 136, 47], we set it as a free parameter to the models. All the models give an equally good fit to both kinds of the experiments but only the AA model gives physically meaningful values of the relaxation times. The relaxation times obtained from the AA model show a decreasing trend with increasing temperature, while it is not the case for the other two models. This trend is coherent with all the reported relaxation times. On the other hand, the relaxation time obtained from the IC and AC models are similar. This indicates the small influence of the anisotropic diffusion on the reaction kinetics. Moreover, the same relaxation time for both systems can explain the experiments using a modification of the reorganization energy. This difference in the reorganization energy could be originated from the differences in the charges of the solutes[111]. In addition, the comparisons between the AC and AA models in the nematic phase show that the $R(t)$ obtained from the AA model is always higher than the other one. This is due to the anisotropic reactivity. A qualitative study to estimate the influence of the diffusion coefficient, relaxation time and the reorganization energy indicates that the contribution of each factor is in the following order: $\tau_L \gg \lambda_s^F > D_z/D_\rho$. The importance of the relaxation time to the reaction kinetics was also reported in study of the intramolecular electron transfer in liquid crystals[53, 26].

The theoretical predictions obtained from three different level of anisotropy

are able to explain the individual experimental results in liquid crystals because the effect of anisotropic diffusion is relatively modest for 5CB in the nematic phase. Moreover, the diffusion coefficient, relaxation time and reorgnization energy are related through the multiplication and the influence of each factor is in a wide time range. Hence, they are compensated to explain the results.

It can be concluded that the effect of solvent anisotropic structure in the solutes' diffusion is observable though it is not a dominant factor that translates in peculiarities of the chemical kinetics of bimolecular reactions. The success of the diffusion-reaction approach to explain these experimental results reinforces the confidence in them and their applicability to a large variety of environments. This thesis represents a step forward in the generalization of this kind of models to complex media. A clear receipt is provided as how to proceed to adapt models originally thought for homogeneous solutions to systems like cell cytoplasms and membranes, solar cells and others.

Appendices

Appendix A

Numerical Calculations

A.1 Anisotropic diffusion problems

In this section, a partial differential equation PDE for diffusion problems in cylindrical coordinates will be solved by the Method of Lines, MOLs. The symmetry of liquid crystals in the nematic phase is cylindrical and the measured diffusion coefficients showed two values which are equivalent to D_ρ and D_z[170].

$$n_t = \nabla^2 n = \frac{D_\rho}{\rho} n_\rho + D_\rho n_{\rho\rho} + D_\rho \frac{1}{\rho^2} n_{\phi\phi} + D_z n_{zz} \tag{A.1}$$

The pair correlation function is written as $n(\rho, z, t)$ because the problem is symmetric with respect to ϕ and the third term in eq. (A.1) disappears. The PDE for anisotropic Smoluchowski diffusion with an uniaxial symmetry was described in eq. (A.1) [171, 172]. The model for the reactivity and the target shape in this problem is spherical; it is therefore better to express variables in spherical coordinate r, θ and ϕ. The relationship between these two coordinates systems is shown in table A.1.

Table A.1: Coordinate transformation and variable definitions

Cylindrical coordinate		Spherical coordinate	
$\rho = r \sin\theta$	$0 \leq \rho \leq \infty$	$r = \sqrt{\rho^2 + z^2}$	$0 \leq r \leq \infty$
$\phi = \phi$	$0 \leq \phi \leq 2\pi$	$\phi = \phi$	$0 \leq \phi \leq 2\pi$
$z = r \cos\theta$	$-\infty \leq z \leq \infty$	$\theta = \arctan \frac{\rho}{z}$	$-\frac{\pi}{2} \leq \theta \leq \frac{\pi}{2}$

By transformation of variables and using the chain rule for the partial

derivatives, eq. (A.1) can be expressed in spherical coordinates as

$$\begin{aligned} n_t = {} & n_r \frac{D_\rho + D_\rho \cos^2\theta + D_z \sin^2\theta}{r} \\ & + n_\theta \frac{D_\rho - D_\rho 2\sin^2\theta + D_z 2\sin^2\theta}{r^2 \tan\theta} \\ & + n_{r\theta} \frac{2\sin\theta\cos\theta(D_\rho - D_z)}{r} \\ & + n_{rr}(D_\rho \sin^2\theta + D_z \cos^2\theta) \\ & + n_{\theta\theta} \frac{D_\rho \cos^2\theta + D_z \sin^2\theta}{r^2}. \end{aligned}$$

where

$$\begin{aligned} n_\rho &= n_r \sin\theta + n_\theta \frac{\cos\theta}{r} \\ n_{\rho\rho} &= n_{rr}\sin^2\theta + n_r \frac{\cos^2\theta}{r} + n_{r\theta}\frac{2\sin\theta\cos\theta}{r} - n_\theta \frac{2\sin\theta\cos\theta}{r^2} + n_{\theta\theta}\frac{\cos^2\theta}{r^2} \\ n_z &= n_r \cos\theta - n_\theta \frac{\sin\theta}{r} \\ n_{zz} &= n_{rr}\cos^2\theta + n_r \frac{\sin^2\theta}{r} - n_{r\theta}\frac{2\sin\theta\cos\theta}{r} + n_\theta \frac{2\sin\theta\cos\theta}{r} + n_{\theta\theta}\frac{\sin^2\theta}{r^2} \end{aligned} \tag{A.2}$$

This diffusion problem can be solved with help of auxiliary conditions, so called initial and boundary conditions, IC and BC, respectively. Let consider a simple case of diffusion problem, a Smoluchowski model which implies that the reactivity is infinite at the contact distance between reactants. The assumption for this model is expressed in eq. (A.3).

$$\begin{aligned} n(r,\theta,0) &= \begin{cases} 0, & 0 < r \leq \sigma. \\ 1, & \sigma < r \leq \infty. \end{cases} \\ n(\sigma,\theta,t) &= 0 \\ n(\infty,\theta,t) &= 1 \end{aligned} \tag{A.3}$$

To solve this PDE numerically using MOLs, the spatial derivatives in PDE are replaced with algebraic approximations to have a system of ODEs. The system of ODEs with known initial condition can be further integrated in time and give a solution for the PDE. A practical example MATLAB code was well written in Schiesser and Griffiths[108]. To solve eq. (A.3), there are two spatial variables which form a plane defined by r and θ. It is wise to set $0 \leq \theta \leq \frac{\pi}{2}$ because of the symmetry around this axis reducing the number of points in the calculation. Moreover, the variable r expands on several orders of magnitudes from the contact and the changes are rapid close to contact. On the other hand, the angle variable changes gradually from 0 to $\pi/2$. Therefore, the logarithmic scale for r and the linear scale for θ were applied in this study. The numerical

definitions of the derivatives for this particular space can be derived from their Taylor expansion, giving the following result:

$$\begin{aligned}
n_r &= \frac{n_{i+1,j} - 10^{2\Delta L} n_{i-1,j} - (1 - 10^{2\Delta L}) n_{i,j}}{r_i (10^{2\Delta L} - 1)} \\
n_\theta &= \frac{n_{i,j+1} - n_{i,j-1}}{2\Delta\theta} \\
n_{r\theta} &= \frac{n_{i+1,j+1} - n_{i+1,j-1} - 10^{2\Delta L} n_{i-1,j+1} + 10^{2\Delta L} n_{i-1,j-1} - (1 - 10^{2\Delta L})(n_{i,j+1} - n_{i,j-1})}{2\Delta\theta r_i (10^{2\Delta L} - 1)} \\
n_{rr} &= \frac{2(n_{i+1,j} + 10^{\Delta L} n_{i-1,j} - (1 + 10^{\Delta L}) n_{i,j})}{(10^{2\Delta L})(1 - 10^{-\Delta L})} \\
n_{\theta\theta} &= \frac{n_{i,j+1} - 2n_{i,j} + n_{i,j-1}}{\Delta\theta^2}.
\end{aligned} \tag{A.4}$$

The derivatives for non-uniform space was adopted[173] and modified for a decadic logarithmic space. ΔL is equal to $\log_{10}(r_{i+1}/r_i)$. Finite difference approximations for $f(x)$ using Taylor expansion at point $i{+}1$ and $i{-}1$ according to fig. A.1a reads

$$\begin{aligned}
f_{i+1} &= f_i + h_i f_i' + \frac{h_i^2}{2} f_i'' + ... \\
f_{i-1} &= f_i - h_{i-1} f_i' + \frac{h_{i-1}^2}{2} f_i'' + ...
\end{aligned} \tag{A.5}$$

The above equations give rise to

$$\begin{aligned}
f_i' &= \frac{f_{i+1} - 10^{2\Delta L} f_{i-1} - (1 - 10^{2\Delta L}) f_i}{h_i (1 + 10^{\Delta L})} + ... \\
f_i'' &= 2\frac{f_{i+1} + 10^{\Delta L} f_{i-1} - (1 + 10^{\Delta L}) f_i}{h_i h_{i-1} + h_i^2} + ... \\
\text{where } 10^{\Delta L} &= \frac{h_i}{h_{i-1}} = \frac{x_i}{x_{i-1}}.
\end{aligned} \tag{A.6}$$

Let consider a case when x belongs to a decadian logarithmic domain. Then the ratio between two consecutive x members is constant and $10^{\Delta L} = x_i/x_{i-1} = x_{i+1}/x_i$. If $10^{\Delta L} = 1$, eq. (A.6) is reduced to the central finite difference equations for a uniform grid.

$$\begin{aligned}
f_i' &= \frac{f_{i+1} - f_{i-1}}{2h} + ... \\
f_i'' &= \frac{f_{i+1} - 2f_i + f_{i-1}}{h^2} + ...
\end{aligned} \tag{A.7}$$

For a mixed second derivative like $n_{r\theta}$ a scheme in fig. A.1b was applied. This derivative is uniform for θ domain and non-uniform for r domain. The equation

reads

$$\begin{aligned} n_{r\theta} =& \frac{\partial}{\partial\theta}(\frac{\partial n}{\partial r}) \\ =& \frac{(n_\theta)_{i+1,j} - 10^{2\Delta L}(n_\theta)_{i-1,j} - (1-10^{2\Delta L})(n_\theta)_{i,j}}{h_i(1+10^{\Delta L})} \\ =& \frac{n_{i+1,j+1} - n_{i+1,j-1} - cc^2 n_{i-1,j+1} + 10^{2\Delta L} n_{i-1,j+1} + (10^{2\Delta L}-1)(n_{i,j+1} - n_{i,j-1})}{(h_i(1+10^{\Delta L}))2\Delta\theta}. \end{aligned} \tag{A.8}$$

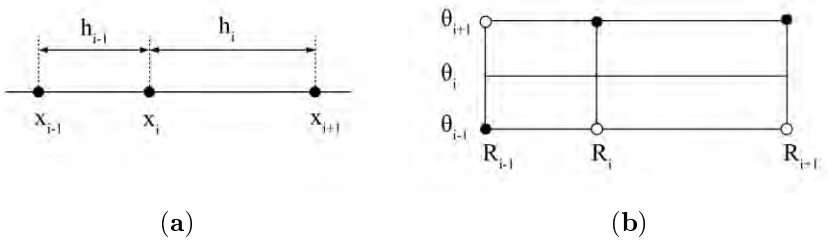

(**a**) (**b**)

Figure A.1: Finite difference schemes with non-uniform intervals for (a) one variable x and (b) two variables r and θ.

There are 4 boundaries in the region calculated. First at the inner and outer boundary conditions, $r = \sigma$, $r = \infty$, the time derivatives equals zero, $n_t = 0$. The summation of all spatial derivatives equals to zeros. Second the reflective boundary conditions, $\theta = 0$ or $\theta = \frac{\pi}{2}$, this leads to no net exchange in these boundaries due to symmetry. Therefore, the mixed derivative is equal to zero because the first derivative with respect to θ equals to zeros. The equations read

$$\begin{aligned} n_\theta &= 0 \\ n_{r\theta} &= 0 \\ n_{\theta\theta} &= 2\frac{n_{i,j+1} - n_{i,j}}{\Delta\theta^2} \text{ at } \theta = 0 \\ n_{\theta\theta} &= 2\frac{n_{i,j} - n_{i,j-1}}{\Delta\theta^2} \text{ at } \theta = \frac{\pi}{2} \end{aligned} \tag{A.9}$$

MATLAB codes applying this are shown in listing A.1. The subroutines for MOL calculation, rate calculation and visualize plot are shown in listing A.2 and A.3.

The analytical reaction rate coefficient for the Smoluchowski model reads $k(t) = 4\pi\sigma D(1 + \frac{\sigma}{\sqrt{\pi Dt}})$. Normally the reaction rate coefficient in the Smoluchowski theory is defined by the first derivative with respect to distance at contact. This definition leads to very bad result for numerical calculations. On the other hand, the integral definition can be derived from the integration

of PDE, assuming that the time integration of $\nabla^2 n$ is zero[174]. The validity of this definition was compared with the numerical calculation for pure spherical problem. The reaction rate coefficient is described in eq. (A.10).

$$k(t) = -\int_0^{\infty}\int_0^{\frac{\pi}{2}} 4\pi r^2 \sin\theta n_t dr d\theta \tag{A.10}$$

The time integration of the reaction rate coefficient $k(t)$ is proportional to $R(t)$ in eq. (4.3) and it is called $\kappa(t)$ in this section. $\kappa(t)$ was used to compare the numerical results. A good agreement between analytical solution and the numerical result is shown in fig. A.2 for isotropic diffusion problems. The deviation at short time is due to the coarsing close to contact radius. This numerical result was obtained from 301 points in r and 46 points in θ and the calculation takes less than one hour for a computer with RAM of 1.53 GB and CPU of 2.2 GHz. Further test was performed for anisotropic diffusion problems when $D_\rho/D_z = 0.1$ or 10. Comparisons for both diffusion coefficient ratios and the number of points in θ are shown in fig. A.3. It is clear that the point density in θ is less sensitive and the optimum spatial point densities are 301 and 46 for r and θ, respectively.

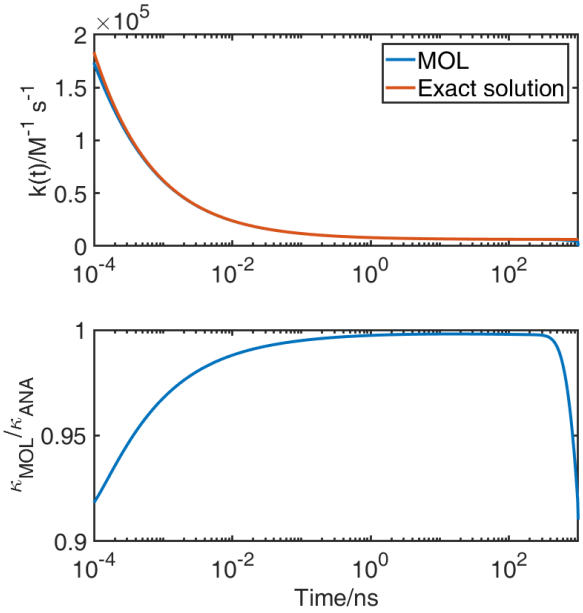

Figure A.2: (top) $k(t)$ obtained from analytical solution (red line) and from MOL (blue dot), the contact radius was 5 Å and diffusion coefficient was 100 $Å^2/ns$, (bottom) ratio of $\kappa(t)$ from MOL to exact solution

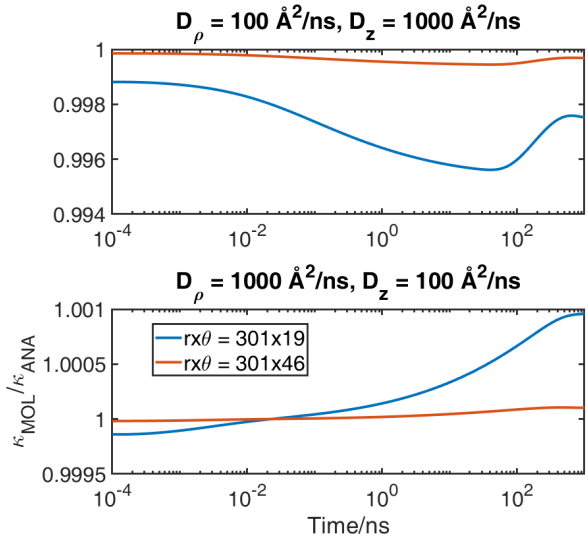

Figure A.3: Comparisons of $\kappa(t)$ obtained from (top) diffusion ratio = 0.1 and (bottom) diffusion ratio = 10, numbers of points in r and θ = (blue) 301, 19 and (red) 301, 46 with respect to $\kappa(t)$ obtained from the same diffusion coefficients and numbers of points for r and θ were 301 and 91, respectively.

The Differential Encounter Theory was also implemented. Within the framework of this theory, a sink term is added to the diffusion equation. The diffusional operator is defined by eq. (A.2). The sink term consists of distance dependence reactivity times population density. Therefore, some population at the contact survives, this is the so called partial reflective boundary. The PDE reads

$$n_t = \nabla^2 n(r,\theta,t) - w(r)n(r,\theta,t) \tag{A.11}$$

$$w(r) = w_0 \exp(\frac{\sigma - r}{L}) \tag{A.12}$$

where w_0 and L are reactivity at contact and tunneling length, respectively. The boundary conditions in eq. (A.9) at the contact has changed to eq. (A.13). The initial condition for DET set the initial population equals to one everywhere, $n(r,\theta,0) = 1$. The outer boundary condition and the reflective boundaries are kept the same.

$$\begin{aligned} n_r = 0,\ n_\theta = 0,\ n_{r\theta} &= 0 \\ n_{\theta\theta} &= \frac{2(n_{(i,j+1)} - n_{(i,j-1)})}{\Delta\theta^2} \\ n_{rr} &= \frac{2(n_{(i,j+1)} - n_{(i,j)})}{r_i(10^{\Delta}L - 1)(1 - 10^{-\Delta L})} \end{aligned} \tag{A.13}$$

A MATLAB code to calculate DET for the pure centrosymmetric problem using the PDE algorithm from the software package are shown in listing A.4 and the associted subroutines are shown in listing A.5.

The results from MOL calculations were compared with pdepe solver from MATLAB for the same problem setting to validate the method. $k(t)$ and $\kappa(t)$ from both calculations were compared in fig. A.4. The calculation takes less than 5 minutes for a computer with RAM of 0.17 GB and CPU of 3.2 GHz because of the slower reactivity at contact and the deviation at long time is just 3%.

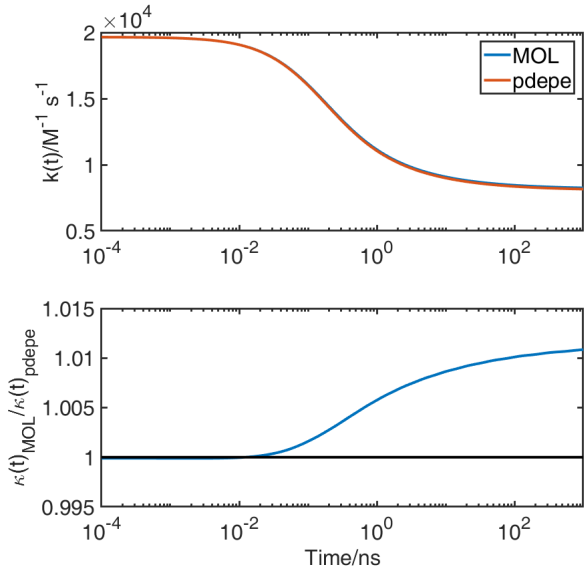

Figure A.4: Reaction rate (top) obtained from pdepe function (red line) and from MOL (blue dot), the contact radius is 5 Å and diffusion coefficient is 100 $Å^2/ns$, ratio of reaction rate from MOL to pdepe function (bottom), number of points for MOL in r and θ were 101 and 46 and for pdepe in r was 101

A.2 Anisotropic diffusion under potential

In presence of potential, the diffusion equation reads

$$n_t = \nabla \cdot D \cdot (e^{-v} \nabla e^{v} n(r,\theta,t)) - w(r) n(r,\theta,t) \tag{A.14}$$

where

$$\begin{aligned} \nabla \cdot D \cdot e^{-v} \nabla e^{v} n &= \nabla \cdot \begin{pmatrix} D^A & D^B \\ D^B & D^A \end{pmatrix} \begin{pmatrix} n_r + n v_r \\ \frac{n_\theta}{r} + n \frac{v_\theta}{r} \end{pmatrix} \begin{pmatrix} \vec{u}_r & \vec{u}_\theta \end{pmatrix} \\ \nabla \cdot D\vec{H} &= \frac{2}{r} DH(r) + DH_r(r) + \frac{\cot\theta}{r} DH(\theta) + \frac{1}{r} DH_\theta(\theta). \end{aligned} \tag{A.15}$$

The diffusion matrix in spherical coordinate is defined as follows.

$$D = \begin{pmatrix} D_\rho \sin^2\theta + D_z \cos^2\theta & (D_\rho - D_z)\sin\theta\cos\theta \\ (D_\rho - D_z)\sin\theta\cos\theta & D_\rho \sin^2\theta + D_z\cos^2\theta \end{pmatrix} = \begin{bmatrix} D^A & D^B \\ D^B & D^A \end{bmatrix} \tag{A.16}$$

Therefore, the diffusion coefficients and their derivatives are as follows.

$$\begin{aligned} D^A &= D_\rho \sin^2\theta + D_z\cos^2\theta \\ D^B &= (D_\rho - D_z)\sin\theta\cos\theta \\ D^A_\theta &= 2(D_\rho - D_z)\sin\theta = 2D^B \\ D^B_\theta &= (D_\rho - D_z)(2\cos^2 - 1) \end{aligned} \tag{A.17}$$

Each term in eq. (A.15) is equal to

$$\begin{aligned} DH(r) &= D^A(n_r + nv_r) + \frac{D^B}{r}(n_\theta + nv_r) \\ DH_r(r) &= D^A(n_r r + nv_r r + n_r v_r) + \frac{D^B}{r^2}(rn_{r\theta} - n_\theta + rnv_{r\theta} + rn_r v_\theta - nv_\theta) \\ DH(\theta) &= D^B(n_r + nv_r) + \frac{D^A}{r}(n_\theta + nv_r) \\ DH_\theta(\theta) &= D^B(n_{r\theta} + nv_{r\theta} + n_\theta v_r) + D^B_\theta(nv_r + n_r) \\ &\quad + \frac{D^A}{r}(n_{\theta\theta} + nv_{\theta\theta} + n_\theta v_\theta) + \frac{D^A_\theta}{r}(nv_\theta + n_\theta) \end{aligned} \tag{A.18}$$

Substituting eq. (A.18) and eq. (A.17) into eq. (A.15) gives

$$\begin{aligned} n_t = &\frac{D^A}{r^2}(2rn_r + 2rnv_r + r^2 n_{rr} + r^2 nv_{rr} + r^2 n_r v_r + n_{\theta\theta} + nv_{\theta\theta} + n_\theta v_\theta) \\ &+ \frac{D^B}{r^2}(n_\theta + nv_\theta + 2rn_{r\theta} + 2rnv_{r\theta} + rn_r v_\theta + rn_\theta v_r) \\ &+ \frac{(D^B_\theta + D^B\cot\theta)}{r}(n_r + nv_r) + \frac{(D^A_\theta + D^A\cot\theta)}{r^2}(n_\theta + nv_\theta) \\ &- w(r)n. \end{aligned} \tag{A.19}$$

The initial condition and boundary conditions for this problem are as follow. Initial condition reads

$$n(r,\theta,0) = g(r,\theta). \tag{A.20}$$

Inner boundary condition reads

$$\begin{aligned}
\vec{u}_r \cdot D \cdot (e^{-v}\nabla e^{v} n(\sigma)) &= 0 \\
DH(\sigma) &= 0 \\
n_t = &\frac{D^A}{\sigma^2}(\sigma^2 n_{rr} + \sigma^2 n v_{rr} + \sigma^2 n_r v_r + n_{\theta\theta} + n v_{\theta\theta} + n_\theta v_\theta) \\
&+ \frac{D^B}{\sigma^2}(2\sigma n_{r\theta} + 2\sigma n v_{r\theta} + \sigma n_r v_\theta - n_\theta - n v_\theta) \\
&+ \frac{(D^B_\theta + D^B \cot\theta)}{\sigma}(n_r + n v_r) + \frac{(D^A_\theta + D^A \cot\theta)}{\sigma^2}(n_\theta + n v_\theta) \\
&- w(\sigma) n.
\end{aligned} \tag{A.21}$$

Outer boundary condition reads

$$n_t = 0. \tag{A.22}$$

Reflective boundary conditions when $\theta = 0$ or $\pi/2$ are taken from eq. (A.9). The MATLAB code for MOL with potential calculation was listed in A.6. There are two sections in the code which are the initialization and the calculation of time derivatives.

The eq. (A.14) is reduced to be eq. (A.11) in the absence of potential and can be written as follows.

$$\begin{aligned}
n_t &= \nabla \cdot D \cdot \nabla n - w(r) n \\
&= \nabla \cdot D\vec{G} - w(r) n \\
&= \frac{2}{r} DG(r) + DG_r(r) + \frac{\cot\theta}{r} DG(\theta) + \frac{1}{r} DG_\theta(\theta)
\end{aligned} \tag{A.23}$$

where

$$\begin{aligned}
DG(r) &= D^A n_r + \frac{D^B}{r} n_\theta \\
DG_r(r) &= D^A n_r r + \frac{D^B}{r^2}(r n_{r\theta} - n_\theta) \\
DG(\theta) &= D^B n_r + \frac{D^A}{r} n_\theta \\
DG_\theta(\theta) &= D^B n_{r\theta} + D^B_\theta n_r + \frac{D^A}{r} n_{\theta\theta} + \frac{D^A_\theta}{r} n_\theta.
\end{aligned} \tag{A.24}$$

Substituting eq. (A.24) and eq. (A.17) into eq. (A.23) gives

$$\begin{aligned}
n_t = &\frac{D^A}{r^2}(2 r n_r + r^2 n_{rr} + n_{\theta\theta}) + \frac{D^B}{r^2}(n_\theta + 2 r n_{r\theta}) \\
&+ \frac{(D^B_\theta + D^B \cot\theta)}{r} n_r + \frac{(D^A_\theta + D^A \cot\theta)}{r^2} n_\theta \\
&- w(r) n.
\end{aligned} \tag{A.25}$$

The initial condition and boundary conditions for this case are identical to the problem under potential except the inner boundary condition. The equation reads

$$\begin{aligned} \vec{u}_r \cdot D \cdot n(\sigma) &= 0 \\ DG(\sigma) &= 0 \\ n_t = \frac{D^A}{\sigma^2}(\sigma^2 n_{rr} + n_{\theta\theta}) + \frac{D^B}{r^2}(2\sigma n_{r\theta} - n_\theta) & \\ + \frac{(D^B_\theta + D^B \cot\theta)}{\sigma} n_r + \frac{(D^A_\theta + D^A \cot\theta)}{\sigma^2} n_\theta & \\ - w(\sigma) n. & \end{aligned} \tag{A.26}$$

The eq. (A.25) was implemented using MOL calculation and compared with pdepe in MATLAB code. The results for the reaction and $\kappa(t)$ ratio from the calculations were shown in fig. A.5.

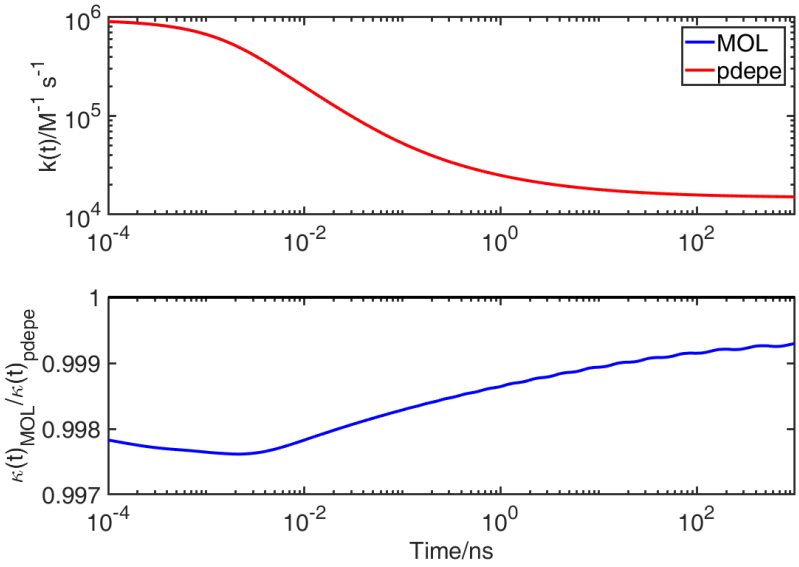

Figure A.5: Reaction rate (top) obtained from pdepe function (red line) and from MOL (blue line) and (bottom) ratio of $\kappa(t)$ from MOL and pdepe calculations

The differences are very small and the deviation is in the limit of the numerical error. This is a check point to compare the new approach to the previous approach. The next step is to compare the result from eq. (A.19) with pdepe with the same potential and diffusion coefficients. A set of variables to test equation A.19 were listed in table A.2. The reaction from the case of $w_0 = 10$ ns^{-1} is shown in fig. A.6. The optimum calculation is obtained with $N_r =$

601 points. This calculation costs approx. 27 minutes using a single node from Topola, ICM. Topola is high performance computer cluster at the Interdisciplinary Center for Mathematical and Computational Modeling, University of Warsaw.

Table A.2: Variables for the centrosymetric diffusion problems

Variables	Values
D_ρ/Å^{2}ns^{-1}	100
D_z/Å^{2}ns^{-1}	100
σ/Å	5.4
w_0/ns^{-1}	0.1, 1, 10, 100, 1000
L/Å	1.5
N_r/points	401, 601, 801, 1001
N_θ/points	19

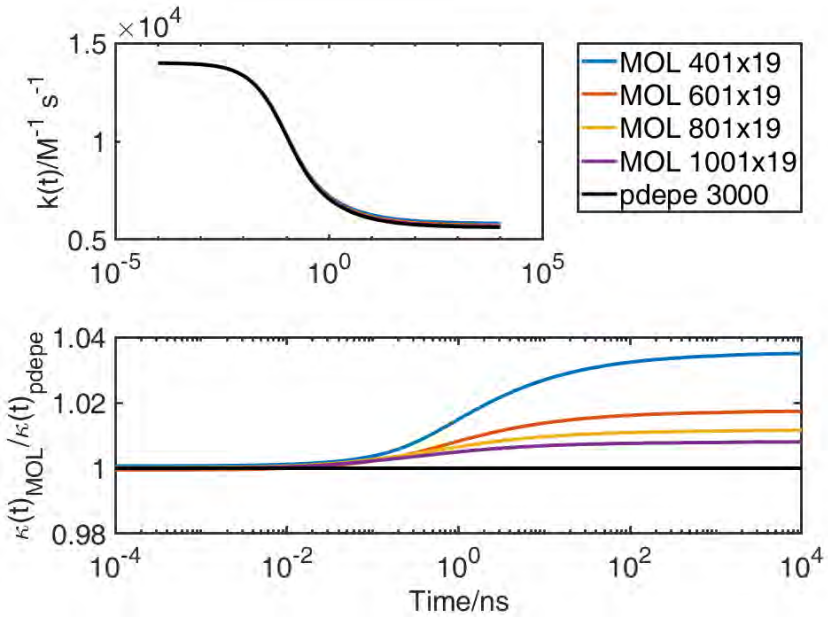

Figure A.6: Reaction rate coefficient (top) obtained from pdepe function (black line) and from MOL and (bottom) ratio of $\kappa(t)$ from MOL and pdepe calculations. The parameters for both calculations are shown in table A.2 except w_0 = 1 ns^{-1}. Both calculations are performed with the same potential.

The asymmetric diffusion problems were also performed using eq. (A.19). A set of variables to test equation A.19 were listed in table A.3. The reaction from the case of w_0 = 100 ns^{-1} are shown in fig. A.7. The optimum calculation is obtained with N_r = 601 points and N_θ = 46 points. This calculation costs

approx. 50 minute using a single node from Topola, ICM.

Table A.3: Variables for the asymmetric diffusion problems

Variables	Values
$D_\rho/\text{Å}^2\text{ns}^{-1}$	100
$D_z/\text{Å}^2\text{ns}^{-1}$	10, 1000
$\sigma/\text{Å}$	5.4
w_0/ns^{-1}	100, 1000, 10000
L/Å	1.5
N_r/points	401
N_θ/points	19, 46, 91

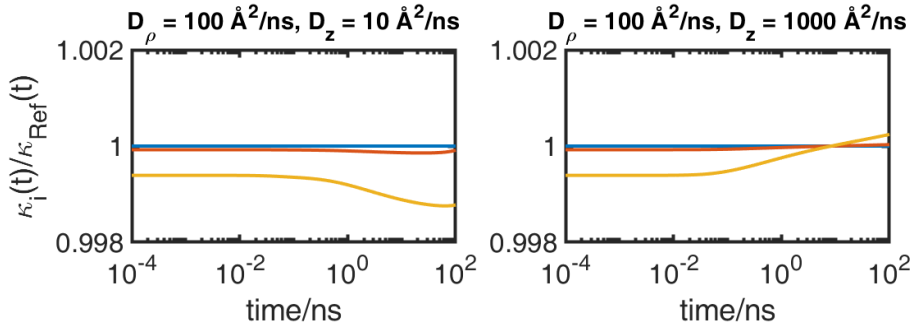

Figure A.7: $\kappa(t)$ ratios obtained the simulations with different N_θ: 19, 46 and 91, yellow, red and blue, respectively. The $\kappa_{ref}(t)$ is the case of $N_\theta = 91$. Two different diffusion coefficient ratios D_ρ/D_z are (left) 10 and (right) 0.1. Both calculations are performed with the same potential. $w_0 = 100$ ns^{-1}.

An alternative definition of the asymmetric diffusion problems under potential is also proposed. Multiplying eq. (A.15) with e^v and defining $m(r,\theta,t) = e^v n(r,\theta,t)$ gives

$$\begin{aligned} m_t = \frac{\partial(e^{-v}n)}{\partial t} &= e^{-v}\nabla\cdot D\cdot(e^{-v}\nabla e^v n) - e^{-v}w(r)n \\ &= e^v(\nabla e^{-v})\cdot(D\nabla m) + \nabla\cdot(D\nabla m) - w(r)m \end{aligned} \tag{A.27}$$

where

$$\begin{aligned} e^v &= \frac{1}{g(r,\theta)} \\ e^v(\nabla e^{-v}) &= \begin{pmatrix} -v_r \\ -\frac{v_\theta}{r} \end{pmatrix} \\ D\nabla m &= \begin{pmatrix} D^A m_r + \frac{D^B}{r} m_\theta \\ D^B m_r + \frac{D^A}{r} m_\theta \end{pmatrix}. \end{aligned} \tag{A.28}$$

Substituting eq. (A.28) into eq. (A.27), the diffusion equation reads

$$\begin{aligned} m_t = &-(v_r D^A + \frac{v_\theta}{r} D^B) m_r - (v_r D^B + \frac{v_\theta}{r} D^A) m_\theta \\ &+ \frac{D^A}{r^2}(2r m_r + r^2 m_{rr} + m_{\theta\theta}) + \frac{D^B}{r^2}(2 m_{r\theta} + m_\theta) \\ &+ \frac{(D^B_\theta + D^B \cot\theta)}{r} m_r + \frac{(D^A_\theta + D^A \cot\theta)}{r^2} m_\theta \\ &- w(r) m. \end{aligned} \tag{A.29}$$

The initial condition and boundary conditions for this case are following. Initial condition reads

$$m(r, \theta, 0) = e^v n(r, \theta, 0) = e^v (g(r, \theta) = 1. \tag{A.30}$$

Inner boundary condition reads

$$\begin{aligned} m_t = &-\frac{v_\theta}{r}(D^B m_r + D^A m_\theta) \\ &+ \frac{D^A}{\sigma^2}(\sigma^2 m_{rr} + m_{\theta\theta}) + \frac{D^B}{\sigma^2}(2\sigma m_{r\theta} - m_\theta) \\ &+ \frac{(D^B_\theta + D^B \cot\theta)}{\sigma} m_r + \frac{(D^A_\theta + D^A \cot\theta)}{\sigma^2} m_\theta \\ &- w(\sigma) m. \end{aligned} \tag{A.31}$$

Outer boundary condition reads

$$m_t = 0. \tag{A.32}$$

Reflective boundary conditions when $\theta = 0$ or $\pi/2$ are taken from eq. (A.9).

Some calculation tests with this alternative formulation revealed that the computational time is not less than with the above presented one. Therefore, we stick to the earlier.

Listing A.1: MATLAB code to solve Smoluchoski equation A.2

```
% coordinate R and theta
sigma=5; % unit angstrom
D0=[1e2 1e2]; % rho and z; unit angstrom^2/ns
ntheta=46;
theta=linspace(0,pi/2,ntheta); % unit radian
thetad=linspace(0,90,ntheta); % unit degree
rmax=2e2*sigma; nr=30; % unit angstrom
rspace=logspace(log10(sigma),log10(rmax),nr);
tmin=1e-4; tmax=1e3; nt=200; % unit ns
```

```
tspace=[0,logspace(log10(tmin),log10(tmax),nt-1)];

% set IC
u0=zeros(nr,ntheta);
for i=1:nr
    for j=1:ntheta
        if i == 1
            u0(i,j)=0;
        else
            u0(i,j)=1;
        end
    end
end

reltol=1.0e-06; abstol=1.0e-06;
options=odeset('RelTol',reltol,'AbsTol',abstol,'Stat','on');
[t,u02]=ode15s(@(t,u) MOLrthetanonuniforgrid(t,u,rspace,thetad,D0,
    sigma),tspace,u0(:),options);
umol2=reshape(u02,nt,nr,ntheta);
% plot k(t) and n(r,theta,t)
[kt,ktexact]=ktMOL(umol2,tspace,rspace,thetad,sigma,D0,'rtheta');
figure
semilogx(tspace,kt,'.',tspace,ktexact,'-')
plotMOL(umol2,tspace,(1:nt),rspace,(1:nr),thetad,(1:ntheta),'
    surface-time');
```

Listing A.2: Subroutine for MOL calculation with non-uniform grid as describe in equation A.3

```
%% MOL method with nonuniformgrid
% PDE   nt =
% + nr*(Drho+Drho*cos(theta)^2+Dz*sin(theta)^2)/r
% + ntheta*(Drho-Drho*2*sin(theta)^2+Dz*2*sin(theta)^2)/(r^2*tan(
    theta))
% + nrtheta*(2*sin(theta)*cos(theta)/r*(Drho-Dz))
% + nrr*(Drho*sin(theta)^2+Dz*cos(theta)^2)
% + ntheta2*(Drho*cos(theta)^2+Dz*sin(theta)^2)/r^2
% 0 <= rspace <= rmax,  0 <= theta <= 90
% derivative definition was taken from SUNDQVIST and VERONIS,
    Tellus, 1969
function ut2 = MOLrthetanonuniforgrid(t,uin,rspace,theta,D0,sigma)
nr=length(rspace);
ntheta=length(theta);
Drho=D0(1); Dz=D0(2);
```

```
14 u=reshape(uin,nr,ntheta);
15
16 delr=rspace(2)/rspace(1); % delr = 10^delta
17 deltheta=(theta(2)-theta(1));
18 delatheta2=deltheta^2;
19 term1=zeros(nr,ntheta); % nr
20 term2=zeros(nr,ntheta); % ntheta
21 term3=zeros(nr,ntheta); % nrtheta
22 term4=zeros(nr,ntheta); % nrr
23 term5=zeros(nr,ntheta); % ntheta2
24 ut1=zeros(nr,ntheta);
25
26 for i=1:nr
27     for j=1:ntheta
28         if i == 1 || i == nr % inner BC, n(r,theta,t)=0; and
               outter BC, n(r,theta,t)=1;
29             term1(i,j)=0; term2(i,j)=0; term3(i,j)=0; term4(i,j)
                   =0; term5(i,j)=0;
30         elseif j == 1 || j == ntheta && i > 1 && i < nr
31             % reflective BC at alpha =0 and pi/2, ntheta=0;
                   nrtheta=0;
32             term1(i,j)=(Drho+Drho*cosd(theta(j))^2+Dz*sind(theta(j
                   ))^2)/rspace(i)* ...
33                 (u(i+1,j)-delr^2*u(i-1,j)-(1-delr^2)*u(i,j))/(
                       rspace(i)*(delr^2-1));
34             term2(i,j)=0;
35             term3(i,j)=0;
36             term4(i,j)=(Drho*sind(theta(j))^2+Dz*cosd(theta(j))^2)
                   * ...
37                 2/rspace(i)^2/(delr^2-1)/(1-1/delr)*(u(i+1,j)+delr
                       *u(i-1,j)-(1+delr)*u(i,j));
38             if j == 1
39                 term5(i,j)=(Drho*cosd(theta(j))^2+Dz*sind(theta(j)
                       )^2)/rspace(i)^2* ...
40                     2*(u(i,j+1)-u(i,j))/delatheta2;
41             else
42                 term5(i,j)=(Drho*cosd(theta(j))^2+Dz*sind(theta(j)
                       )^2)/rspace(i)^2* ...
43                     2*(u(i,j)-u(i,j-1))/delatheta2;
44             end
45         else
46             term1(i,j)=(Drho+Drho*cosd(theta(j))^2+Dz*sind(theta(j
                   ))^2)/rspace(i)* ...
47                 (u(i+1,j)-delr^2*u(i-1,j)-(1-delr^2)*u(i,j))/(
```

```
                    rspace(i)*(delr^2-1));
48              term2(i,j)=(Drho-Drho*2*sind(theta(j))^2+Dz*2*sind(
                    theta(j))^2)/(rspace(i)^2*tand(theta(j)))* ...
49                  (u(i,j+1)-u(i,j-1))/2/deltheta;
50              term3(i,j)=(2*sind(theta(j))*cosd(theta(j))/rspace(i)
                    *(Drho-Dz))*...
51                  (u(i+1,j+1)-u(i+1,j-1)-delr^2*u(i-1,j+1)+delr^2*u(
                        i-1,j-1)+(delr^2-1)*(u(i,j+1)-u(i,j-1)))/ ...
52                  (2*deltheta*rspace(i)*(delr^2-1));
53              term4(i,j)=(Drho*sind(theta(j))^2+Dz*cosd(theta(j))^2)
                    * ...
54                  2/rspace(i)^2/(delr^2-1)/(1-1/delr)*(u(i+1,j)+delr
                        *u(i-1,j)-(1+delr)*u(i,j));
55              term5(i,j)=(Drho*cosd(theta(j))^2+Dz*sind(theta(j))^2)
                    /rspace(i)^2* ...
56                  (u(i,j+1)-2*u(i,j)+u(i,j-1))/delatheta2;
57          end
58          % PDE formation
59          ut1(i,j)=term1(i,j)+term2(i,j)+term3(i,j)+term4(i,j)+term5
                (i,j);
60      end
61  end
62  ut2=ut1(:);
63  end
```

Listing A.3: Subroutines for rate calculation and visualize the result from MOL

```
1   % To plot the solution from MOL
2   % Three types are 'surface-time', 'space1-time', 'space2-time'
3   % nsol is sorted by tindex, sindex1, sindex2
4   % tindex, sindex1 and sindex2 are indices of the corresponding
        tspace,
5   % space1 and space2
6   function plotMOL(nsol,tspace,tindex,space1,sindex1,space2,sindex2,
        flag,marker)
7   if nargin <= 8
8       marker='-';
9   end
10  figure
11  if strcmp(flag,'surface-time')
12      for c=1:length(tindex)
13          pt=tindex(c);
14          surf(space2(sindex2),space1(sindex1),reshape(nsol(pt,
                sindex1,sindex2),length(sindex1),length(sindex2)))
```

```
15          text1=sprintf('t = %2.2d',tspace(pt));
16          title(text1)
17          pause(0.1)
18      end
19      zlim([0 1]);
20      ang=char(197);
21      xlabel(['space2/',ang])
22      ylabel(['space1/',ang])
23      zlabel('n(space1,space2,t)')
24  elseif strcmp(flag,'space1-time')
25      for c=1:length(tindex)
26          pt=tindex(c);
27          if ~isscalar(sindex2)
28              error('sindex2 has to be scalar.')
29          end
30          semilogx(space1(sindex1),reshape(nsol(pt,sindex1,sindex2),
                length(sindex1),length(sindex2)),marker)
31          hold on
32      end
33      text1=sprintf('cut at %2.2d',space2(sindex2));
34      title(text1)
35      hold off
36      ylim([0 1]);
37      ang=char(197);
38      xlabel(['space1/',ang])
39      ylabel('n(space1,space2,t)')
40  elseif strcmp(flag,'space2-time')
41      for c=1:length(tindex)
42          pt=tindex(c);
43          if ~isscalar(sindex1)
44              error('sindex2 has to be scalar.')
45          end
46          semilogx(space2(sindex2),reshape(nsol(pt,sindex1,sindex2),
                length(sindex1),length(sindex2)),marker)
47          hold on
48      end
49      text1=sprintf('cut at %2.2d',space2(sindex1));
50      title(text1)
51      hold off
52      ylim([0 1]);
53      ang=char(197);
54      xlabel(['space2/',ang])
55      ylabel('n(space1,space2,t)')
56  else
```

```
57      error('Request is no recognized.')
58  end
59
60  end
61  %% To calculate kt from spatial matrix resulted from MOL
62  function [kt,ktexact]=ktMOL(nsol,tspace,space1,space2,sigma,D0,
        flag,vis)
63  if nargin <=6
64      flag = 'rtheta';
65      vis = 0;
66  elseif nargin == 7
67      vis = 0;
68  else
69      error('Too many inputs')
70  end
71  if ~isrow(tspace) && ~isvector(tspace)
72      error('tspace has to be a row vector.')
73  end
74  if ~isscalar(sigma) && ~isscalar(D0)
75      error('sigma, D0 and normfactor have to be scalars.')
76  end
77
78  nt=length(tspace);
79  ns1=length(space1);
80  ns2=length(space2);
81  if size(nsol)~= [nt, ns1, ns2]
82      error('size of nsol need to follow size of (tspace, space1 and
            space2).')
83  end
84      if strcmp(flag,'rz')
85          rspace=space1;
86          zspace=space2;
87      elseif strcmp(flag,'rtheta')
88          rspace=space1;
89          theta=space2*pi/180;
90      else
91      error('Coordinate is not registered.')
92      end
93  kt=zeros(nt,1);
94  ut=zeros(size(nsol));
95  ut(1:end-1,:,:)=diff(nsol,1,1)./diff(tspace)';
96  for k=1:nt
97      mesh1=reshape(ut(k,:,:),ns1,ns2);
98      if strcmp(flag,'rz')
```

```
99      kt(k,1)=-2*trapz(zspace,trapz(rspace,2*pi*rspace.*mesh1,1));
100     elseif strcmp(flag,'rtheta')
101     kt(k,1)=-trapz(rspace,rspace'.^2.*(trapz(theta,4*pi.*sin(theta
            ).*mesh1,2)));
102     else
103     end
104 end
105
106 dummy1=4*pi*sigma*D0(1)*(1+sigma./sqrt(pi*D0(1).*tspace));
107 ktexact=interp1(tspace(2:end),dummy1(2:end),tspace,'pchip');
108 if vis == 1
109     figure
110     semilogx(tspace,kt,'.',tspace,ktexact,'-')
111     xlabel('Time/ns')
112     ylabel('Rate of reaction/M^{-1} s^{-1}')
113     legend('MOL','Exact solution')
114 end
115 end
```

Listing A.4: MATLAB code to solve DET PDE in eq. (A.11) and eq. (A.12)

```
1  % coordinate R and theta
2  sigma=5; % unit angstrom
3  D0=[1e2 1e2]; % Drho and Dz; unit angstrom^2/ns
4  w0=1e1; l0=sigma/2;
5  ntheta=46;
6  theta=linspace(0,pi/2,ntheta); % unit radian
7  thetad=linspace(0,90,ntheta); % unit degree
8  rmax=2e2*sigma; nr=31; % unit angstrom
9  rspace=logspace(log10(sigma),log10(rmax),nr);
10 tmin=1e-4; tmax=1e3; nt=200; % unit ns
11 tspace=[0,logspace(log10(tmin),log10(tmax),nt-1)];
12
13 % set IC n(r,theta,0)=1;
14 u0=zeros(nr,ntheta);
15 for i=1:nr
16     for j=1:ntheta
17         u0(i,j)=1;
18     end
19 end
20 wr=w0*exp((sigma-rspace)/l0);
21 reltol=1.0e-06; abstol=1.0e-06;
22 options=odeset('RelTol',reltol,'AbsTol',abstol,'Stat','on');
23 [t,u02]=ode15s(@(t,u) MOLDET(t,u,rspace,thetad,D0,wr),tspace,u0(:)
```

```
    ,options);
umol2=reshape(u02,nt,nr,ntheta);
% pdepe
m = 2;
sol = pdepe ( m, @pdeRTheta, @icRTheta, @bcRTheta, rspace, tspace,
     [], D0(1),w0,l0,sigma);
u = sol(:,:,1);

% calculate kt
% pdepe
% kt=4*pi*int(wr*n*r^2)dr
% MOL r,theta
% kt=4*pi*int(wr*n*r^2*sin(theta))dr dtheta
ktpde=trapz(rspace,4*pi*rspace.^2.*wr.*u,2);
ktmol=zeros(nt,1);
for k=1:nt
    mesh=reshape(umol2(k,:,:),nr,ntheta);
    ktmol(k,1)=trapz(theta,sin(theta).*trapz(rspace',4*pi*rspace
        '.^2.*wr'.*mesh,1));
end
% compare kt_MOL/kt_pdepe
krat=zeros(nt,1);
for k=2:nt
    krat(k,1)=trapz(tspace(1:k),ktmol(1:k))./trapz(tspace(1:k),
        ktpde(1:k));
end
figure
subplot(2,1,1);semilogx(tspace,ktmol,'.',tspace,ktpde,'-')
ylabel('Reaction rate/M^{-1} s^{-1}')
legend('MOL','pdepe')
subplot(2,1,2);semilogx(tspace,krat,'.',tspace,ones(nt,1),'-k')
ylabel('kt_{MOL}/kt_{pdepe}')
xlabel('Time/ns')
```

Listing A.5: Subroutines for MOL and pdepe calculation follow eq. (A.4) and eq. (A.13).

```
%% pdepe solver, standard method
function [ c, f, s ] = pdeRTheta ( x, t, u, DuDx, D0,w0,l0,sigma)
% set PDE
c=1;
f=D0.*DuDx;
wr=w0*exp((sigma-x)/l0);
s=-wr.*u;
```

```
8  end
9  function u0 = icRTheta ( x ,D0,w0,l0,sigma)
10 u0=1; % set IC n(r,0)=1
11 end
12 function [ pl, ql, pr, qr ] = bcRTheta ( xl, ul, xr, ur, t,D0,w0,
       l0,sigma )
13 % set BC
14 pl = 0; ql = 4*pi*xl^2;
15 pr = ur(1)-1; qr = 0;
16 end
17 %% MOL method with DET nonuniformgrid
18 % PDE   nt =
19 % + nr*(Drho+Drho*cos(theta)^2+Dz*sin(theta)^2)/r
20 % + ntheta*(Drho-Drho*2*sin(theta)^2+Dz*2*sin(theta)^2)/(r^2*tan(
       theta))
21 % + nrtheta*(2*sin(theta)*cos(theta)/r*(Drho-Dz))
22 % + nrr*(Drho*sin(theta)^2+Dz*cos(theta)^2)
23 % + ntheta2*(Drho*cos(theta)^2+Dz*sin(theta)^2)/r^2
24 % - wr*n
25 % 0 <= rspace <= rmax,  0 <= theta <= 90
26 function ut2 = MOLDET(t,uin,rspace,thetad,D0,wr)
27
28 nr=length(rspace);
29 ntheta=length(thetad);
30 Drho=D0(1); Dz=D0(2);
31 u=reshape(uin,nr,ntheta);
32
33 delr=rspace(2)/rspace(1); % delr = 10^del
34 deltheta=(thetad(2)-thetad(1));
35 delatheta2=deltheta^2;
36 term1=zeros(nr,ntheta); % nr
37 term2=zeros(nr,ntheta); % ntheta
38 term3=zeros(nr,ntheta); % nrtheta
39 term4=zeros(nr,ntheta); % nrr
40 term5=zeros(nr,ntheta); % ntheta2
41 ut1=zeros(nr,ntheta);
42 for i=1:nr
43     for j=1:ntheta
44         if i == 1 % inner BC flux with respect to theta = 0
45             term1(i,j)=0; term2(i,j)=0; term3(i,j)=0;
46             term4(i,j)=(Drho*sind(thetad(j))^2+Dz*cosd(thetad(j))
                   ^2)* ...
47                  2/rspace(i)/(delr-1)/(1-1/delr)*(u(i+1,j)-u(i,j));
48             if j == 1
```

```
49          term5(i,j)=(Drho*cosd(thetad(j))^2+Dz*sind(thetad(j))
                ^2)/rspace(i)^2* ...
50              2*(u(i,j+1)-u(i,j))/delatheta2;
51          elseif j == ntheta
52          term5(i,j)=(Drho*cosd(thetad(j))^2+Dz*sind(thetad(j))
                ^2)/rspace(i)^2* ...
53              2*(u(i,j)-u(i,j-1))/delatheta2;
54          else
55          term5(i,j)=(Drho*cosd(thetad(j))^2+Dz*sind(thetad(j))
                ^2)/rspace(i)^2* ...
56              (u(i,j+1)-2*u(i,j)+u(i,j-1))/delatheta2;
57          end
58      elseif i == nr % outer BC n(r,theta,t)=1
59          term1(i,j)=0; term2(i,j)=0; term3(i,j)=0; term4(i,j)
                =0; term5(i,j)=0;
60      elseif j == 1 || j == ntheta && i > 1 && i < nr %
            reflective BC at alpha =0 and pi/2
61          term1(i,j)=(Drho+Drho*cosd(thetad(j))^2+Dz*sind(thetad
                (j))^2)/rspace(i)* ...
62              (u(i+1,j)-delr^2*u(i-1,j)-(1-delr^2)*u(i,j))/(
                    rspace(i)*(delr^2-1));
63          term2(i,j)=0;
64          term3(i,j)=0;
65          term4(i,j)=(Drho*sind(thetad(j))^2+Dz*cosd(thetad(j))
                ^2)* ...
66              2/rspace(i)^2/(delr^2-1)/(1-1/delr)*(u(i+1,j)+delr
                    *u(i-1,j)-(1+delr)*u(i,j));
67          if j == 1
68              term5(i,j)=(Drho*cosd(thetad(j))^2+Dz*sind(thetad(
                    j))^2)/rspace(i)^2* ...
69                  2*(u(i,j+1)-u(i,j))/delatheta2;
70          else
71              term5(i,j)=(Drho*cosd(thetad(j))^2+Dz*sind(thetad(
                    j))^2)/rspace(i)^2* ...
72                  2*(u(i,j)-u(i,j-1))/delatheta2;
73          end
74      else
75          term1(i,j)=(Drho+Drho*cosd(thetad(j))^2+Dz*sind(thetad
                (j))^2)/rspace(i)* ...
76              (u(i+1,j)-delr^2*u(i-1,j)-(1-delr^2)*u(i,j))/(
                    rspace(i)*(delr^2-1));
77          term2(i,j)=(Drho-Drho*2*sind(thetad(j))^2+Dz*2*sind(
                thetad(j))^2)/(rspace(i)^2*tand(thetad(j)))* ...
78              (u(i,j+1)-u(i,j-1))/2/deltheta;
```

```
79              term3(i,j)=(2*sind(thetad(j))*cosd(thetad(j))/rspace(i
                    )*(Drho-Dz))*...
80                  (u(i+1,j+1)-u(i+1,j-1)-delr^2*u(i-1,j+1)+delr^2*u(
                        i-1,j-1)+(delr^2-1)*(u(i,j+1)-u(i,j-1)))/ ...
81                  (2*deltheta*rspace(i)*(delr^2-1));
82              term4(i,j)=(Drho*sind(thetad(j))^2+Dz*cosd(thetad(j))
                    ^2)* ...
83                  2/rspace(i)^2/(delr^2-1)/(1-1/delr)*(u(i+1,j)+delr
                        *u(i-1,j)-(1+delr)*u(i,j));
84              term5(i,j)=(Drho*cosd(thetad(j))^2+Dz*sind(thetad(j))
                    ^2)/rspace(i)^2* ...
85                  (u(i,j+1)-2*u(i,j)+u(i,j-1))/delatheta2;
86          end
87          % PDE   nt = A*nr + B*ntheta + C*nrtheta + D*nrr + E*
                ntheta2 - wr*n
88          % PDE formation
89          ut1(i,j)=term1(i,j)+term2(i,j)+term3(i,j)+term4(i,j)+term5
                (i,j)-wr(i)*u(i,j);
90      end
91  end
92  ut2=ut1(:);
93  end
```

Listing A.6: A MATLAB code for MOL with potential calculation follow eq. (A.19) and the auxiliary conditions

```
1  kb=1.3806e-23;% boltzmann constant J/K
2  NA=6.022e23;
3  convFac=6.022e-4;
4
5  % coordinate R and theta
6  rf=8.99; rq=3.13; % unit angstrom
7  sigma=rf;
8  ntheta=11;
9  theta=linspace(0,pi/2,ntheta); % unit radian
10 thetad=linspace(0,90,ntheta); % unit degree
11 rmax=1e4*sigma; nr=201; % unit angstrom
12 rspace=logspace(log10(sigma),log10(rmax),nr);
13 tmin=1e-4; tmax=1e4; nt=1000; % unit ns
14 tspace=[0,logspace(log10(tmin),log10(tmax),nt-1)];
15 sigmarq=rf+rq;
16 D0=[100 100];
17 w0=1e3; l0=1.5;
18 wrt0=w0*exp((sigma-rspace)/l0)';
```

```
19 [gRtheta,VRtheta,Vr,Vrr,Vtheta,Vtt,Vrtheta]=CBgRtheta(rspace,
       thetad);
20 % MOL
21 % set IC n(r,theta,0)=1;
22 u0=zeros(nr,ntheta);
23 for i=1:nr
24     for j=1:ntheta
25         u0(i,j)=gRtheta(i,j);
26 %         u0(i,j)=1;
27     end
28 end
29 reltol=1.0e-06; abstol=1.0e-06;
30 options=odeset('RelTol',reltol,'AbsTol',abstol,'Stat','on');
31 [t,u02]=ode15s(@(t,u) MOLDETgr5(t,u,rspace,thetad,D0,wrt0,Vr,Vrr,
       Vtheta,Vtt,Vrtheta),tspace,u0(:),options);
32 umol2=reshape(u02,nt,nr,ntheta);
33 % calculate kt
34 % MOL r,theta
35 % kt=4*pi*int(wr*n*r^2*sin(theta))dr dtheta
36 ktmol=zeros(nt,1);
37 for k=1:nt
38     mesh=reshape(umol2(k,:,:),nr,ntheta);
39     ktmol(k,1)=trapz(theta,sin(theta).*trapz(rspace',4*pi*rspace
           '.^2.*wrt0.*mesh,1));
40 end
41 %% MOL method with DET nonuniformgrid
42 % new difinition
43 % PDE   nt =
44 % + DA/r^2*(2*r*nr+2*r*n*Vr+r^2*nrr+r^2*n*Vrr+r^2nr*Vr+ntt+n*Vtt+
       ntheta*Vtheta)
45 % + DB/r^2(ntheta+n*Vtheta+2*r*nrtheta+2*r*n*Vrtheta+r*nr*Vtheta+r
       *ntheta*Vtheta)
46 % + (DBtheta+DBcot(theta))/r*(nr+n*Vr)
47 % + (DAtheta+DAcot(theta))/r^2*(ntheta+n*Vtheta)
48 % - wr*n
49 % 0 <= rspace <= rmax,  0 <= theta <= 90
50 function ut2 = MOLDETgr5(t,uin,rspace,thetad,D0,wrt0,Vr,Vrr,Vtheta
       ,Vtt,Vrtheta)
51
52 nr=length(rspace);
53 ntheta=length(thetad);
54 DA=D0(1).*sind(thetad).^2+D0(2).*cosd(thetad).^2;
55 DB=(D0(1)-D0(2)).*sind(thetad).*cosd(thetad);
56 DAtheta=2.*DB;
```

```
57 DBtheta=(D0(1)-D0(2)).*(2*cosd(thetad).^2-1);
58 DAcot=interp1(thetad(2:end),DA(2:end).*cotd(thetad(2:end)),thetad,
       'pchip','extrap');
59 DBcot=(D0(1)-D0(2)).*cosd(thetad).^2;
60 % Drho=D0(1); Dz=D0(2);
61 u=reshape(uin,nr,ntheta);
62
63 delr=rspace(2)/rspace(1); % delr = 10^del
64 deltheta=(thetad(2)-thetad(1));
65 delatheta2=deltheta^2;
66 ut1=zeros(nr,ntheta);
67 for i=1:nr
68 for j=1:ntheta
69
70         if i == 1 % inner BC flux with respect to theta = 0
71             n_r=(u(i+1,j)-u(i,j))/(rspace(i+1)-rspace(i));
72             n_rr=2/rspace(i)^2/(delr-1)/(1-1/delr)*(u(i+1,j)-u(i,j
                   ));
73             if j == 1
74             n_theta=0;
75             n_rtheta=0;
76             n_tt=2*(u(i,j+1)-u(i,j))/delatheta2;
77             elseif j == ntheta
78             n_theta=0;
79             n_rtheta=0;
80             n_tt=2*(u(i,j)-u(i,j-1))/delatheta2;
81             else
82             n_theta=(u(i,j+1)-u(i,j-1))/2/deltheta;
83             n_rtheta=(u(i+1,j+1)-u(i,j+1)-u(i+1,j-1)+u(i,j-1))/(2*
                   rspace(i)*(delr-1)*deltheta);
84             n_tt=(u(i,j+1)-2*u(i,j)+u(i,j-1))/delatheta2;
85             end
86             ut1(i,j)=DA(j)/rspace(i)^2*(rspace(i)^2*n_rr+rspace(i)
                   ^2*u(i,j)*Vrr(i,j)+rspace(i)^2*n_r*Vr(i,j)+n_tt+u(
                   i,j)*Vtt(i,j)+n_theta*Vtheta(i,j)) ...
87                 + DB(j)/rspace(i)^2*(2*rspace(i)*n_rtheta+2*rspace
                       (i)*u(i,j)*Vrtheta(i,j)+rspace(i)*n_r*Vtheta(i
                       ,j)-n_theta-u(i,j)*Vtheta(i,j)) ...
88                 + (DBtheta(j)+DBcot(j))/rspace(i)*(n_r+u(i,j)*Vr(i
                       ,j)) ...
89                 + (DAtheta(j)+DAcot(j))/rspace(i)^2*(n_theta+u(i,j
                       )*Vtheta(i,j)) ...
90                 - wrt0(i)*u(i,j);
91         elseif i == nr % outer BC n(r,theta,t)=1
```

```
92              ut1(i,j)=0;
93          elseif j == 1 || j == ntheta && i > 1 && i < nr %
                reflective BC at alpha =0 and pi/2
94              n_r=(u(i+1,j)-delr^2*u(i-1,j)-(1-delr^2)*u(i,j))/(
                    rspace(i)*(delr^2-1));
95              n_rr=2/rspace(i)^2/(delr^2-1)/(1-1/delr)*(u(i+1,j)+
                    delr*u(i-1,j)-(1+delr)*u(i,j));
96              if j == 1
97              n_tt=2*(u(i,j+1)-u(i,j))/delatheta2;
98              else
99              n_tt=2*(u(i,j)-u(i,j-1))/delatheta2;
100             end
101             ut1(i,j)=DA(j)/rspace(i)^2*(2*rspace(i)*n_r+2*rspace(i
                    )*u(i,j)*Vr(i,j)+rspace(i)^2*n_rr+rspace(i)^2*u(i,
                    j)*Vrr(i,j)+rspace(i)^2*n_r*Vr(i,j)+n_tt+u(i,j)*
                    Vtt(i,j)) ...
102                 + DB(j)/rspace(i)^2*(u(i,j)*Vtheta(i,j)+2*rspace(i
                        )*u(i,j)*Vrtheta(i,j)+rspace(i)*n_r*Vtheta(i,j
                        )) ...
103                 + (DBtheta(j)+DBcot(j))/rspace(i)*(n_r+u(i,j)*Vr(i
                        ,j)) ...
104                 + (DAtheta(j)+DAcot(j))/rspace(i)^2*(u(i,j)*Vtheta
                        (i,j)) ...
105                 - wrt0(i)*u(i,j);
106         else
107             n_r=(u(i+1,j)-delr^2*u(i-1,j)-(1-delr^2)*u(i,j))/(
                    rspace(i)*(delr^2-1));
108             n_theta=(u(i,j+1)-u(i,j-1))/2/deltheta;
109             n_rtheta=(u(i+1,j+1)-u(i+1,j-1)-delr^2*u(i-1,j+1)+delr
                    ^2*u(i-1,j-1)+(delr^2-1)*(u(i,j+1)-u(i,j-1)))/ ...
110                  (2*deltheta*rspace(i)*(delr^2-1));
111             n_rr=2/rspace(i)^2/(delr^2-1)/(1-1/delr)*(u(i+1,j)+
                    delr*u(i-1,j)-(1+delr)*u(i,j));
112             n_tt=(u(i,j+1)-2*u(i,j)+u(i,j-1))/delatheta2;
113
114             ut1(i,j)=DA(j)/rspace(i)^2*(2*rspace(i)*n_r+2*rspace(i
                    )*u(i,j)*Vr(i,j)+rspace(i)^2*n_rr+rspace(i)^2*u(i,
                    j)*Vrr(i,j)+rspace(i)^2*n_r*Vr(i,j)+n_tt+u(i,j)*
                    Vtt(i,j)+n_theta*Vtheta(i,j)) ...
115                 + DB(j)/rspace(i)^2*(n_theta+u(i,j)*Vtheta(i,j)+2*
                        rspace(i)*n_rtheta+2*rspace(i)*u(i,j)*Vrtheta(
                        i,j)+rspace(i)*n_r*Vtheta(i,j)+rspace(i)*
                        n_theta*Vr(i,j)) ...
116                 + (DBtheta(j)+DBcot(j))/rspace(i)*(n_r+u(i,j)*Vr(i
```

```
                    ,j)) ...
117                 + (DAtheta(j)+DAcot(j))/rspace(i)^2*(n_theta+u(i,j
                    )*Vtheta(i,j)) ...
118                 - wrt0(i)*u(i,j);
119
120         end
121 end
122 end
123 ut2=ut1(:);
124 end
```

A.3 Bimolecular reaction simulations

The bimolecular reactions are studied using a Molecular Dynamics simulation sotfware, LAMMPS. The MD simulation provides several possibilities to study the diffusion problems, i.e. the effect of reactant shapes, the effect of quencher-quencher excluded volume, the effect of distance dependence reactivity and the kinetics beyond the target model. The idea of this study lies on a model of particle collisions with known shapes, known potential field, known reactivity, isothermal bath, implicit solvent and their behaviors dictated by Langevin dynamics. For a first approximation, a Smoluchowski diffusion model is applied and the kinetics are compared with the analytical solution. The simulations are divided into two steps including the system equilibration and the generation of trajectories. A set of simulation parameters are shown in table A.4. A psuedo hard-sphere potential [175] was applied for the particle interaction, so called Mie potential, with well depth, $\epsilon = 0.8k_BT$.

Table A.4: MD simulation parameters for bimolecular reactions study

Parameters	Fluorophore	Quencher
σ/Å	4.8	4.0
Mw/g/mol	220	151
N/particles	1	5000
Concentration/mM	0.1	500
	Simulation box	
Length/Å	255.1	
Volume/Å^3	1.667x10^7	
Temperature/K	298.15	
Viscosity/cP	2	

A.3.1 System equilibration

The particles are randomly placed in the box, then the energy of the system is minimized at a constant temperature and pressure. The temperature and pressure are sampled after the equilibration and plotted against time as shown in fig. A.8. The mean squared displacement MSD of the particles is extracted from the particle trajectories and compared with the diffusion coefficients from Stokes-Einstien equation as shown in fig. A.9.

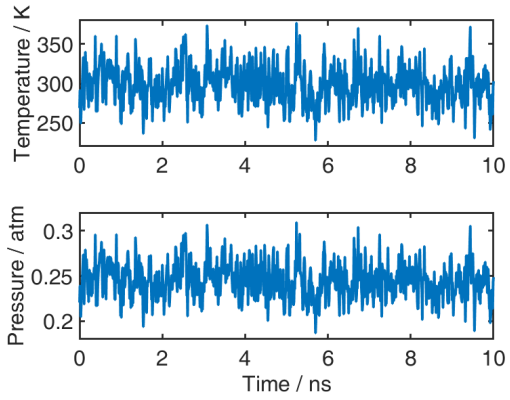

Figure A.8: Temperature and pressure of the simulation box as a function of time

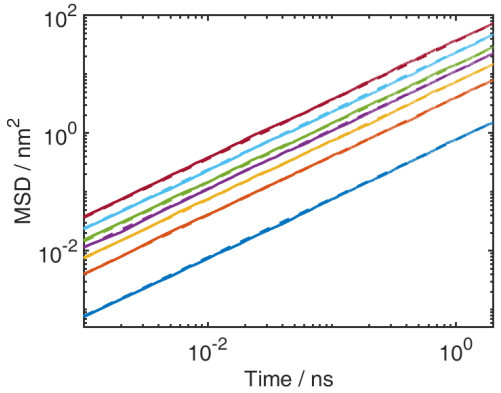

Figure A.9: MSD obtained from (solid) MD simulations and (dash) the Stokes-Eistein equation

A.3.2 Bimolecular reaction simulations and kinetics

The equilibrated configuration is performed under the isothermal condition, implicit solvent and Langevin dynamics. The bimolecular reaction simulation starts from step 3 as shown in fig. A.11. The particles are set to move according

to the Lagevin dynamics under the isothermal condition until there is a pair of particles in the contact distance between the fluorophore and quenchers. Then the reaction stops. If no contact is achieved between fluorophore and quenchers within a given time (t_{end}), the reaction is terminated as well. After the reaction finished, the time at which a reaction occurred or terminated is registered to the histogram. Then, the reaction simulation is repeated at Step 3 until the number of simulations reaches a given value.

The examples of LAMMPS input and output files for bimolecular kinetics are listed in A.7, A.8 and A.9. There are two input files which are FQ.in and generateInput.sh. The FQ.in is an input file for LAMMPS to create an initial particle configuration file and the generateInput.sh is a shell bash script to generate a set of input files for bimolecular reaction simulations as well as submitting the jobs to the cluster. The shell bash script consists of 4 sections – create a new directory, write a LAMMPS input file, write a job file and submit a job file. The output was organized as follows: a header section and a data section. The header contains simulation parameters like box size, particle number, diffusion coefficient, time step and reaction radius. The data section has three columns – Event, Time and Flag. Event means the index of collision event. Time means the time which collision occurs. Flag posses two values, -1 when there was no collision during the trajectory and 1 when there was a collision during the trajectory.

The simulation outputs are the time when the two reactants distance are less than or equal to the reaction radius. A histogram of the output file is shown in fig. A.10. The quantity $E(t)$ represents the number of collisions happening at a given time bin. The last time bin is an artifact because the reaction time window was limited and the unreacted reactants were put in the last bin.

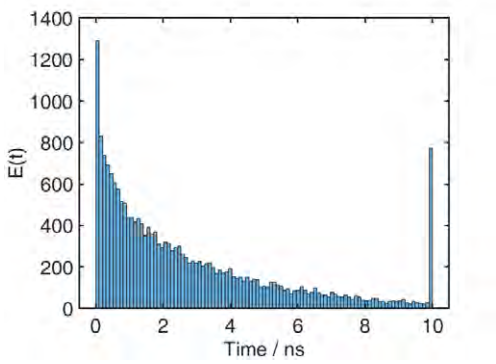

Figure A.10: A histogram of collision number against time from the bimolecular reaction simulations using LAMMPS

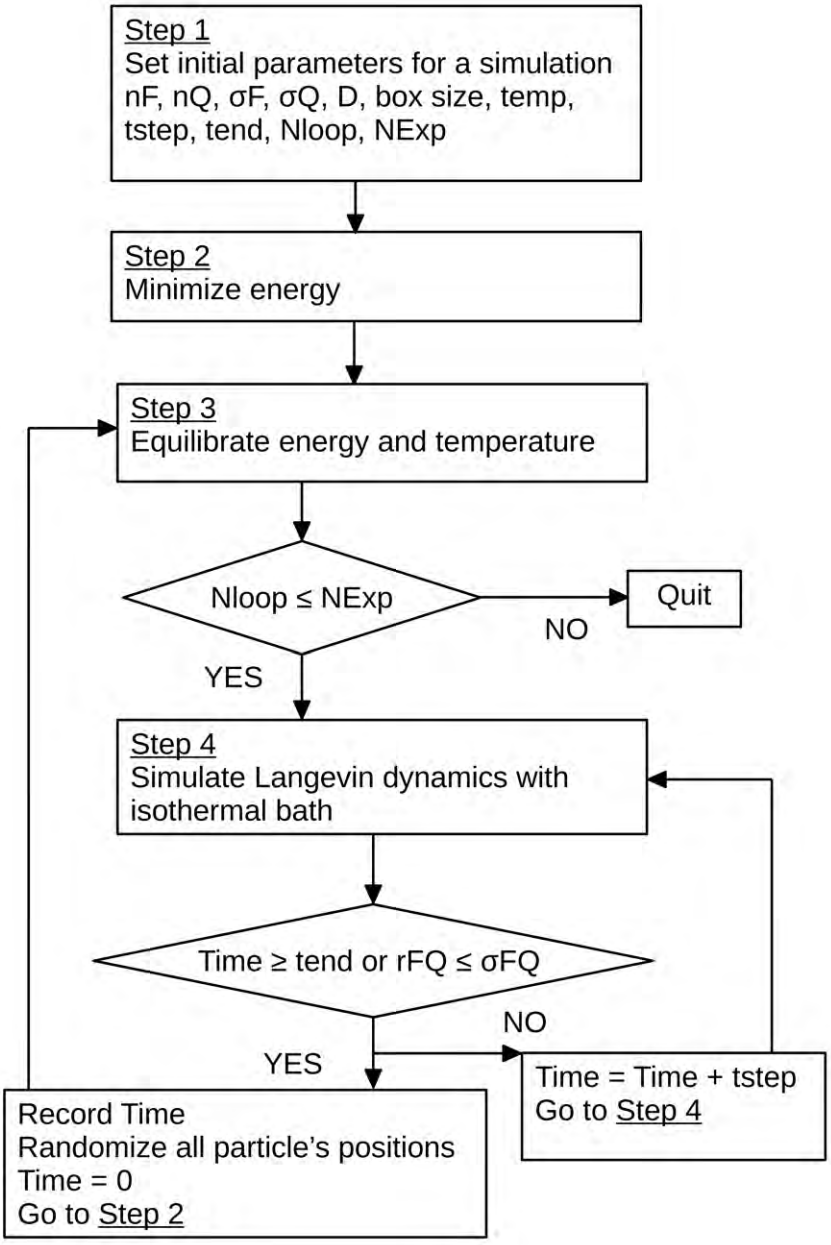

Figure A.11: A calculation flow chart for bimolecular reaction simulations using LAMMPS

The reaction rate coefficient $k(t)$ from this simulation is following:

$$\begin{aligned}
\frac{d[F^*](t)}{dt} &= -\,k(t)[Q][F^*](t) \\
k(t) &= -\,\frac{1}{c}\frac{1}{[F^*]}\frac{d[F^*]}{dt} \\
\text{Let } N_0 &= \sum_{t=0}^{t=\infty} E(t) \\
\text{and } N(t) &= N_0 - \sum_{t=0}^{t} E(t) \\
k(t) &= \frac{1}{c2\Delta t}\ln\left(\frac{N_0 - \sum_{t=0}^{t+\Delta t} E(t)}{N_0 - \sum_{t=0}^{t-\Delta t} E(t)}\right)
\end{aligned} \tag{A.33}$$

The discretized rate coefficient equation in eq. (A.33) is applied to calculate the bimolecular rate cofficient from the simulation outputs. Many parameters are varied to find limits of the simulations. Sets of simulation parameters are summarized in table A.5. The five variables are time windows, equilibration times, diffusion coefficients, quencher radius and quencher concentrations. The kinetics obtained from four time windows are shown in fig. A.12. The shorter time window shows the better statistic. All simulations costed the same calculation time and memory. The equilibration time is the simulation time in Step 3, fig. A.11. The kinetics from three equilibration times are shown in fig. A.13. Too short equilibration time shows deviation at short time because the system does not relax completely and the quencher distribution was not homogeneous around fluorophore. Hence the kinetic at short time is faster. Next is the kinetics from different diffusion coefficients. The kinetics as shown in fig. A.14 are smaller than the Smoluchowski equation at high diffusion coefficients. In this simulation the quencher-quencher interaction was set to zero. This means there was no distance dependence potential or gradient to drive the collision at short time. Another interesting variable is the reactant radii. In this study the fluorophore radius is constant and the quencher radii are varied. The bigger quencher radius is the faster kinetic and the larger deviation from the Smoluchowski equation as shown in fig. A.15. Last variable is the quencher concentration. The kinetics of four quencher concentrations were shown in fig. A.16. The simulated kinetics were aligned well upto 100 mM. The kinetic at 500 mM showed slight deviation at short time but the kinetic finished earlier than the Smoluchowski equation. It is difficult to conclude a limitation from these simulations because there are more aspects needed to be explored like when the quencher-quencher interaction is not zero, the fluorophore diffusion is not zero, the implicit solvent molecules, not infinite reactivity at contact, not spherical fluorophore and quencher shapes and the dipole-dipole molecular

potential. A fair conclusion to be drawn from this study was a set of parameters for a well fit between the simulation and the Smoluchowski equation is as written in table A.5, the last column. The approximated calculation time was 120 hours with 6 x 2.1 GHz of CPU, 5 GB of RAM and 10 nodes in the Topola cluster from ICM.

Table A.5: Common parameters for the simulations are following. σ_F = 4.8 Å, σ_Q = 0.4 Å, [F] = 0.1 mM, [Q] = 100 mM, Box volume = 1.67x10^7 Å^3, Temperature = 293.15 K, Time window = 0.1 ps - 10 ns, Equilibration time = 1.0 ns, D_F = 0 Å^2 ns^{-1}, $\epsilon_{QQ} = 0$, $\epsilon_{FQ} = 0.8k_BT$

Simulation	Variable	Value					D_Q/Å^2 ns^{-1}
fig. A.12	Start time/ps	0.1	0.2	0.5	1.0		55
	End time/ns			10			
	Fit	No	No	Yes	Yes		
fig. A.13	Eq. time/ns	0.02	0.20	1.00			55
	Fit	No	No	Yes			
fig. A.14	D_QÅ^2 ns^{-1}	10	100	300	500		
	Fit	No	Yes	No	No		
fig. A.15	σ_QÅ	0.1	2.0	4.0	8.0	16.0	100
	Fit	No	Yes	No	No	No	
fig. A.16	[Q]/mM	10	50	100	500		150
	Fit	No	Yes	Yes	No		

Table A.6: A set of parameters to obtain the well fit simulation

Parameter	Value	Parameter	Value
Box volume/Å^3	1.67x10^7	Temperature/K	293.15
σ_F/Å	4.8	σ_Q/Å	4.0
[F]/mM	0.1	[Q]/mM	100
Eq. time/ns	1.0	Time window/ns	0.0001 - 10
D_FÅ^2 ns^{-1}	0	D_QÅ^2 ns^{-1}	55
ϵ_{FQ}	0	ϵ_{QQ}	$0.8k_BT$

In order to improve the simulations, one would need to understand the flow chart of the LAMMPS operation. The simulation procedure used here takes outputs to calculate the contact distance on every step, then the simulation is reset. This costs a lot of time which is not used for the reaction calculation. A better way could be writing a function in LAMMPS to perform the bimolecular reaction and return a histogram of the reaction events. As mentioned in the introduction the simulations were intended to supply with a means to understand the reactions in LCs in case of failing with the reaction-diffusion model. As a good agreement was obtained they were no longer necessary. However,

the questions posed in here remain of interest by themselves.

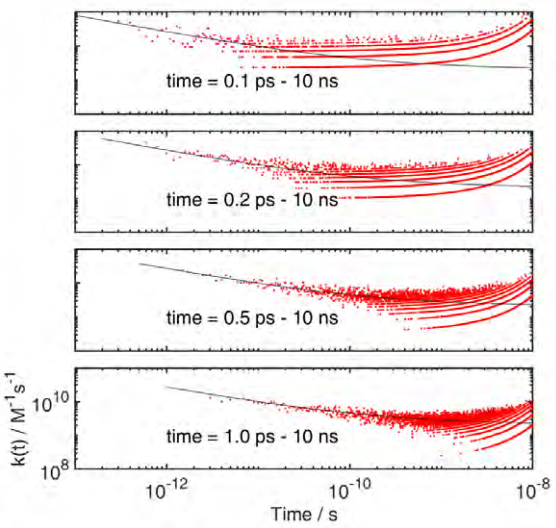

Figure A.12: Kinetics of bimolecular reactions obtained from (solid) Smoluchowski equation and (dot) LAMMPS simulations with the time windows mentioned in table A.5

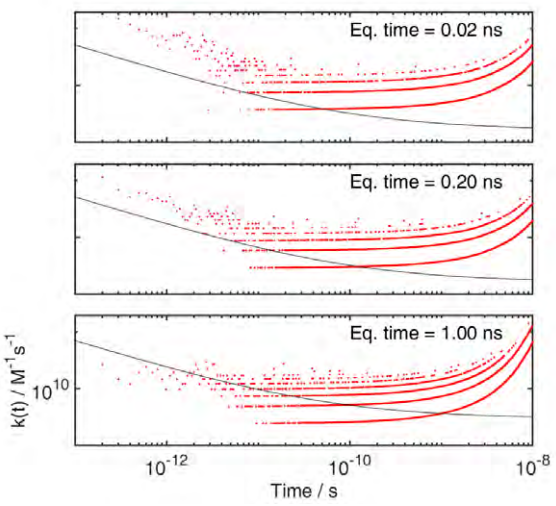

Figure A.13: Kinetics of bimolecular reactions obtained from (solid) Smoluchowski equation and (dot) LAMMPS simulations with the equilibration times mentioned in table A.5

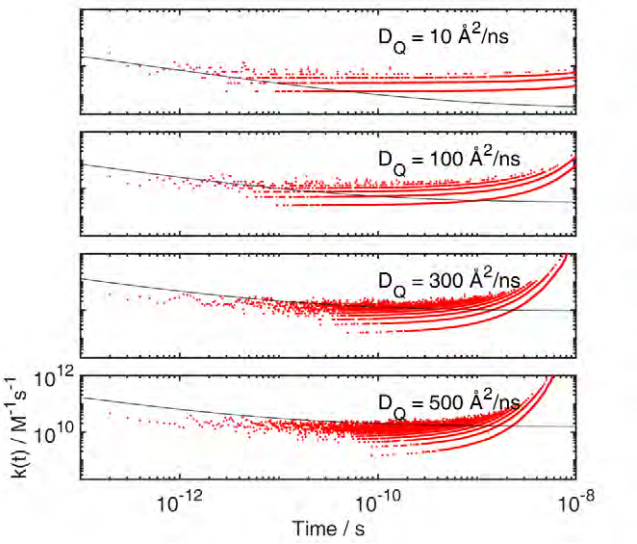

Figure A.14: Kinetics of bimolecular reactions obtained from (solid) Smoluchowski equation and (dot) LAMMPS simulations with the diffusion coefficients mentioned in table A.5

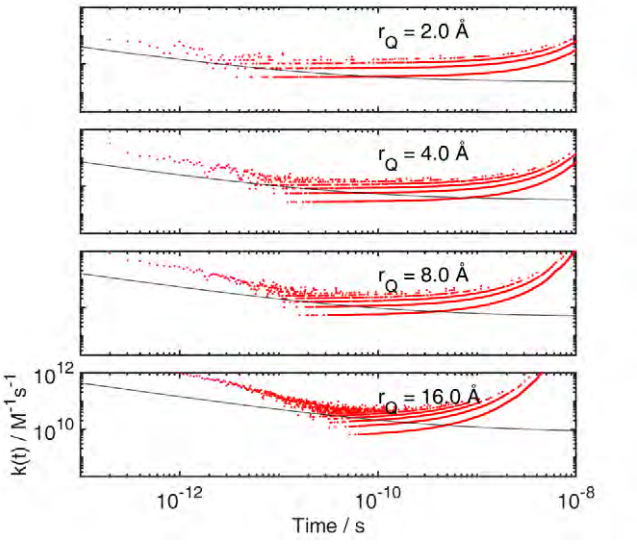

Figure A.15: Kinetics of bimolecular reactions obtained from (solid) Smoluchowski equation and (dot) LAMMPS simulations with the quencher radii mentioned in table A.5

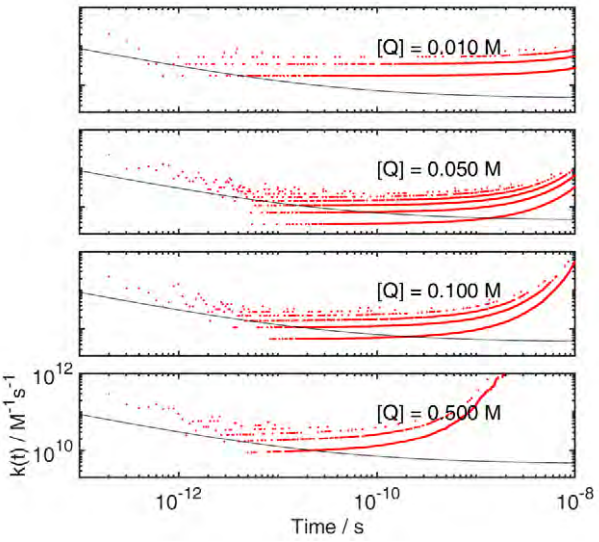

Figure A.16: Kinetics of bimolecular reactions obtained from (solid) Smoluchowski equation and (dot) LAMMPS simulations with the quencher concentrations mentioned in table A.5

Listing A.7: Subroutines for rate calculation and visualize the result from MOL

```
# define numbers of processors
processors 2 2 2

units nano

# 3D system
dimension 3

# Periodic boundary conditions
boundary p p p

# atoms like particles without charge
atom_style atomic
atom_modify map array

# Start the definition of the simulation box
#box size will be 1.66e7 cubic angstrom (Vbox)
#densities F = 1/Vbox Q=5000/Vbox
# S=141000/Vbox

#a numerical variable l is definer
```

```
22 variable l equal 25.51
23 # a cubic region between 0 and l is created
24 region boxid block 0.0 ${l} 0.0 ${l} 0.0 ${l}
25 # a box inside the region, with three types of atoms
26 create_box 2 boxid
27
28 # atomos are placed in the box
29 create_atoms 1 random 1 9879 boxid
30 create_atoms 2 random 100 811987 boxid
31
32 group 1 type 1
33 group 2 type 2
34 group 4 type 1 2
35
36 #   define mass in atto gram/particle
37 # mass of atom type
38 # massF =220g/mol
39 # massQ =151g/mol
40 mass 1 25.000e-5
41 mass 2 25.000e-5
42
43 # To fix atom type1 in space with zero force and zero velocity
44 #fix freeze group-ID setforce 0.0 0.0 0.0
45 #fix freeze 1 setforce 0.0 0.0 0.0
46 # velocity set vx vy vz
47 #velocity 1 set 0.0 0.0 0.0
48 #initial velocity. I think we do need for Brownian. T = 298.0K
49 velocity all create 298.0 4928459 dist gaussian
50
51 #  specify interaction potential pairwise interaction via the Mie
       potential with a cut-off at 3*sigmaF lj-sigma
52 pair_style mie/cut 2.5
53
54 #specify parameters between atoms of type i with an atom of type i
55 #epsilon, sigma, gammaR=50, gammaA=49, cutoff = 3*sigmaF
56 #epsilon at T*=1.25=kBT/eps
57 # epsilon = 329.14e-23J
58 #       the interaction between Q Q is zero because it is assume
       to be point-like particle to avoid the effect of correlation
59 variable eps equal 3.0
60 pair_coeff 1 1 ${eps}   0.40 50 49 2.5
61 pair_coeff 2 2 0.00     0.40 50 49 2.5
62 pair_coeff 1 2 ${eps}   0.40 50 49 2.5
63
```

```
# add long-range tail correction and arithmetic average of epsilon
    and distance
pair_modify tail yes

thermo_style custom step pe ke etotal temp press density
#print out every 0.2 angstrom
thermo 100000
thermo_modify norm no

# minimize total energy to local minimum
minimize 1e-4 1e-6 1000 10000

# to equillibrate system with NVE
timestep 1e-6
fix 1 all nve
run 2000000
unfix 1

timestep 1e-6
fix 4 all nvt temp 298.0 298.0 1e-5
run 1000000
unfix 4
write_restart reaction.save
```

Listing A.8: Subroutines for rate calculation and visualize the result from MOL

```
#!/bin/bash

for i in {01..20}
do
        DIRECTORY="$i"
if [ ! -d "$DIRECTORY" ]; then
        mkdir $DIRECTORY
fi
echo "$DIRECTORY has been created."
cd $DIRECTORY
cp ../*.save ./
#-----------------------------------
#write input for Lammps
cat > reaction.in << EOL
# define numbers of processors
processors 2 2 2
read_restart reaction.save

```

```
group 1 type 1
group 2 type 2
group 4 type 1 2

##########################################
variable magic equal random(0,1,4646${i})
variable drand equal v_magic*25.51/2

variable dt equal 1e-6
variable rz equal 0.40

# cutoff cannot be bigger than rcut in pair coefficient
compute coord all coord/atom cutoff \${rz} 1
compute red all reduce max c_coord
variable ngroup equal c_red
##########################################
compute msdF 1 msd com yes
compute msdQ 2 msd com yes
##########################################
thermo_style custom step pe ke etotal temp press density c_red
#print out every 0.2 angstrom
thermo 10000
thermo_modify norm no
##########################################

variable boxx equal lx
variable boxy equal ly
variable boxz equal lz
variable nf equal count(1)
variable nq equal count(2)
variable w0 equal 1.0
variable trun equal 100
variable dumpdt equal v_dt*v_trun
variable steps equal step

########################################
variable nevent         equal 5000
variable e loop \${nevent}
variable nsearch        equal 100000
#variable s loop \${nsearch}
variable tlast          equal v_nsearch*v_trun*v_dt
################################
print """
input parameter for this system
```

```
63 box: \${boxx} \${boxy} \${boxz} nm
64 nf: \${nf} nq: \${nq}
65 D: 150 Angstrom2/ns
66 reaction radius: \${rz} nm      w0:\${w0}
67 lammps dt: \${dt} ns    dump dt: \${dumpdt} ns
68 Time window: \${dumpdt} - \${tlast} ns
69 Total event: \${nevent}
70 """ file reaction.log
71 ################################
72
73 print """
74 input parameter for this system
75 box: \${boxx} \${boxy} \${boxz} nm
76 nf: \${nf} nq: \${nq}
77 D: 150 Angstrom2/ns
78 reaction radius:\${rz} nm       w0: \${w0}
79 lammps dt: \${dt} nm    dump dt: \${dumpdt} nm
80 Time window: \${dumpdt} - \${tlast} ns
81 Total event: \${nevent}
82 Event           Time            Flag
83 """ file reaction.out
84 ####################################
85 displace_atoms 2 random \${drand} \${drand} \${drand} 1238${i}
86 ################################
87 label start
88
89 # minimize total energy to local minimum
90 minimize 1e-4 1e-6 1000 10000
91
92 # to equillibrate system with NVE
93 timestep \${dt}
94 fix 1 2 nve
95 run 1000000
96 unfix 1
97
98 timestep \${dt}
99 fix 4 2 nvt temp 298.0 298.0 1e-5
100 run 1000000
101 unfix 4
102
103 timestep \${dt}
104 reset_timestep 0
105 print "Start $e step \${steps}" append reaction.log
106 ################################
```

```
fix 6 2 bd 298.0 91.148e-6 21646${i}

label search
run \${trun}

variable s loop \${nsearch}
variable tbin           equal v_s*v_trun*v_dt
if "(\${ngroup} > 0) && (\${magic} <= \${w0})" then &
"print '\$e,            \${tbin},               \${ngroup}' append
    reaction.out" &
"print 'TRUE \$e event, \$s search,     tbin \${tbin},  ngroup \${
   ngroup},      magic \${magic}' append reaction.log" &
"jump SELF BREAK"

print "FALSE \$e event, \$s search,     tbin \${tbin},  ngroup \${
   ngroup},      magic \${magic}}" append reaction.log
next s
jump reaction.in search

################################
print "\$e,             \${tlast},              -1" append
   reaction.out
label BREAK
variable s delete

displace_atoms all random \${drand} \${drand} \${drand} 5438${i}
unfix 6
next e
jump reaction.in start

################################
EOL

#--------------------------------
#write queue job

cat > r.q << EOL
#!/bin/bash -l
#SBATCH -J f${i}nq0100
#SBATCH -N 1
#SBATCH --ntasks-per-node 8
#SBATCH --mem 1000
#SBATCH --time=168:00:00
#SBATCH -A G72-17
```

```
#SBATCH -p  topola
#SBATCH --output="r.q.out"
#SBATCH --error  "r.q.err"

module load common/mpi/openmpi/1.10.1
mpirun -np 8 lmp_mod_mpi < reaction.in > r.out -echo both
EOL
#---------------------------------
sbatch r.q
cd ..
echo "$DIRECTORY copy success."
done
```

Listing A.9: Subroutines for rate calculation and visualize the result from MOL

```
 input parameter for this system box: 25.51 25.51 25.51 nm
nf: 1 nq: 100
D: 150 Angstrom2/ns
reaction radius:0.4 nm  w0: 1
lammps dt: 1e-06 nm     dump dt: 0.0001 nm
Time window: 0.0001 - 10 ns
Total event: 5000
Event           Time            Flag

1,              10,             -1
2,              6.6203,         1
3,              10,             -1
4,              10,             -1
5,              10,             -1
6,              10,             -1
7,              10,             -1
8,              10,             -1
9,              10,             -1
10,             10,             -1
11,             10,             -1
12,             10,             -1
13,             10,             -1
14,             2.1809,         1
15,             1.1033,         1
16,             3.626,          1
17,             10,             -1
18,             8.8064,         1
19,             10,             -1
```

Appendix B

Miscellaneous results

B.1 Effect of DC field on the guest-host systems

This section is devoted to the study of DC electric field effect on the dye bleaching in liquid crystal cells. It is well known that LC alignment can be controlled by the electric filed but there were no systemtic study on the dye bleaching with electric field. Five experiments have been done with dyes in 5CB including (I) Absorption spectra of R6G in 5CB at different temperatures and DC fileds, (II) Chemical stability of R6G mixture under DC filed, (III) Cell conductivity after electrodeposition and (IV) dye degradation under DC fields. The samples in this were prepared in 20 μm thick cells from the Wojskowa Akademia Techniczna or Military University of Technology, WAT. The LC cells from were custom made as shown in fig. B.1. The sample holder for temperature and DC field controller was also custom made as shown in fig. B.1.

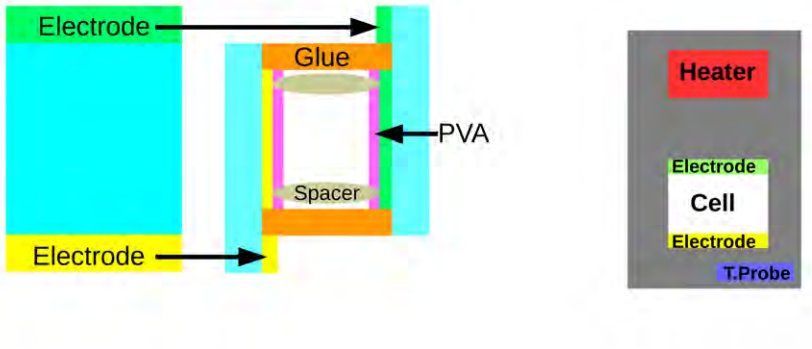

(**a**) (**b**)

Figure B.1: (a) A LC cell from WAT front view and side view and (b) a LC cell sample holder for temperature and DC filed controller
NOTE: T.Probe stands for a temperature probe. Grey represents heat conducting metal.

B.1.1 Absorption spectra of R6G in 5CB at different temperatures and DC fields

R6G in 5CB mixtures have been filled in 20 μm thick cells and measured the absorption spectra at different temperatures and DC fields. The absorption spectra were acquired from Shimadzu UV2700. The results are shown in fig. B.2.

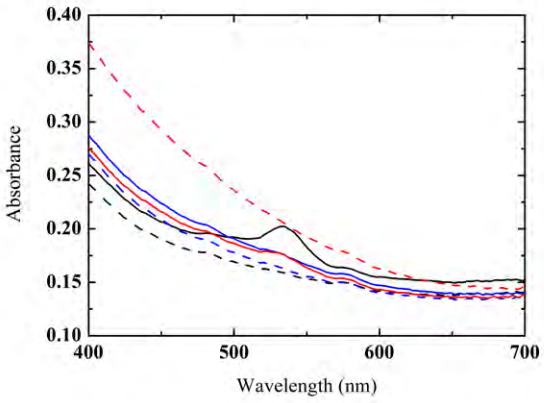

Figure B.2: Absorption spectra of R6G in 5CB at (black) 22, (blue) 40 and (red) 60°C and (solid) 0 or (dash) 6 kV/cm DC fields

The measurements were done from one cell started from 22°C and 0 kV/cm DC field. The absorption of R6G appeared around 450 - 550 nm. The LC cells in this experiment were coated with PVA for planar alignment[140]. Therefore, R6G molecules should align parallel to the substrate surface. After the application of 6 kV/cm DC field, R6G band disappeared. It is interesting that the absorption band of R6G also disappear in other experiments with zero field at 40 and 60°C. This is an indication of the bleaching by the DC field.

B.1.2 Chemical stability of R6G mixture under DC filed

R6G mixtures of 5CB, DMA and ACN with different concentrations are prepared and filled in the cells. The description of each cells were explained in table B.1. All cells were applied with 12 kV/cm DC field for 5 minutes. The results showed that R6G became bleached or changed to brown or black as shown in fig. B.3. This is an indication of chemical reaction due to the DC field. The reaction depends solely on the R6G not the coating layers or other chemical additives.

Table B.1: R6G mixtures and preparation conditions

Sample3	R6G 0.1 mM in 5CB, no PVA coating
Sample4	R6G 0.1 mM in 5CB + DMA 5 μM + ACN 10 μM, no PVA coating
Sample5	R6G 0.1 mM in 5CB + DMA 0.125 mM, no PVA coating
Sample6	R6G 0.1 mM in ACN, no PVA coating, no PVA coating
Sample7	R6G 0.1 mM in 5CB + DMA 5 μM + ACN 10 μM
Sample8	R6G 0.1 mM in 5CB + DMA 0.125 mM
Sample9	R6G 0.1 mM in 5CB
Sample10	R6G 0.1 mM in 5CB + DMA 5 μM
Sample11	R6G 0.1 mM in 5CB + DMA 0.125 mM
Sample14	R6G 5 mM in 5CB

Figure B.3: A photograph of R6G samples after 12 kV/cm DC field for 5 minutes

B.1.3 Cell conductivity after electrodeposition

In this part, the current measurements were used to estimate the cell conductivity after DC field application. The aim is to verify that the reaction gives rise of species which have higher conductivity. The LC cells from section B.1.2 were measured using a multimeter, Sanwa, model PC7000 and compared with the cell with pure 5CB under 12 kV/cm DC field. The measurement set up is displayed in fig. B.4. The measured current from all samples were in microampere. The currents measured for the cells which contained dyes in all cases were a factor 3-5 larger that the cells filled just with 5CB. This increasing conductivity after electric field is similar to that found in previous reports [51, 52, 176, 10]. From this part, one can conclude that R6G is not suitable for quenching studies under DC field because of the poor chemical stability.

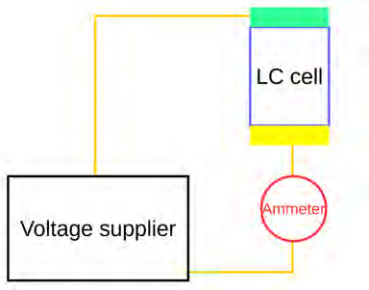

Figure B.4: A current measurement diagram for LC cells

B.2 Dye degradation under DC fields

A set of laser dyes from Lambdachrome were dissolved in ethanol or ACN and tested under 12 kV/cm DC field for 5 minutes. A list of dyes and solvents in this experiment were listed in table B.2. All the cells after DC field application became bleached or changed to black or brown as shown in fig. B.5. Even the neutral dyes were also turned to be black after the DC field application. Therefore, it is impossible to study fluorescence quenching under the electric filed with the dye in LCs at least with this kind of cells. Therefore this experimental strategy was abandoned.

Table B.2: A list of dyes and solvents

Dye	Solvent	Number
Rhodamine B chloride	ethanol	1
Rhodamine 101 perchlorate	ethanol	2
Rhodamine 110 chloride	ethanol	3
Rhodamine 6G chloride	ACN	4
Rhodamine 6G chloride	ethanol	4.2
sulfoRhodamine B	ethanol	1.2
Coumarin 2	ethanol	
Coumarin 7	ethanol	
POPOP	ethanol	

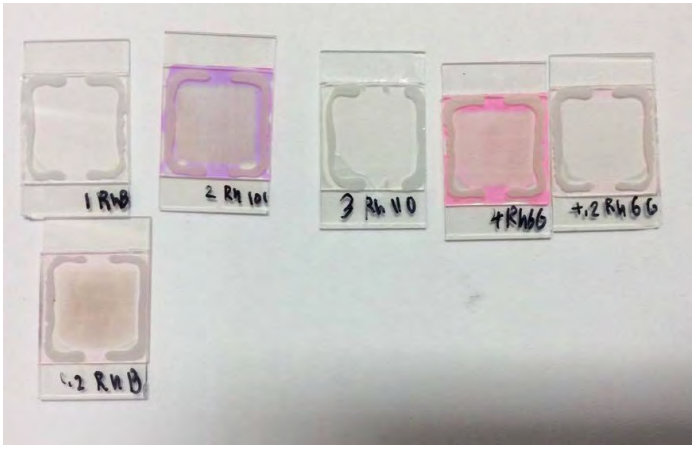

Figure B.5: A photograph of some LC cells after DC field application left to right; 1, 2, 3, 4, 4.2 and 1.2

B.3 Fitting results in DG mixtures

Comparisons of simulated $R(t)$ obtained from R6G-DMpT against temperatures or molar fraction of glycerol are collected below. Later, the fitting results to the experiments of R6G-DMpT and Pe-DMpT in DG mixtures at different temperatures are shown.

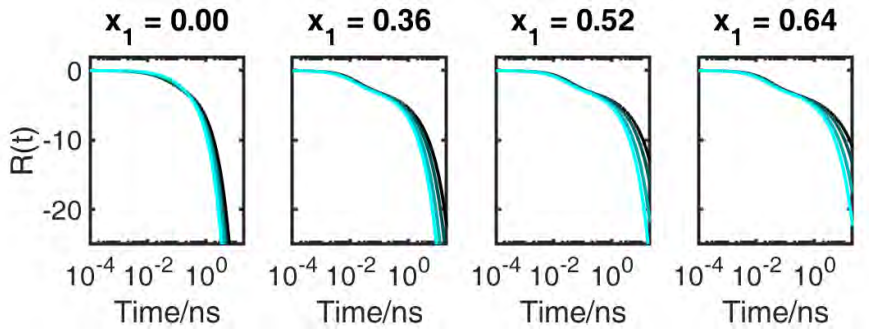

(**a**)

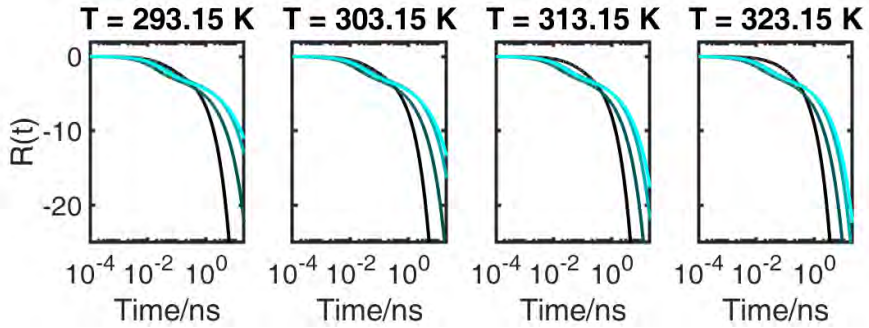

(**b**)

Figure B.6: $R(t)$ obtained from the calculations of R6G-DMpT in DG mixtures at different temperatures and molar fractions of glycerol (x_1); From black to blue lines represent the (a) increasing temperature and (b) increasing molar fraction of glycerol.

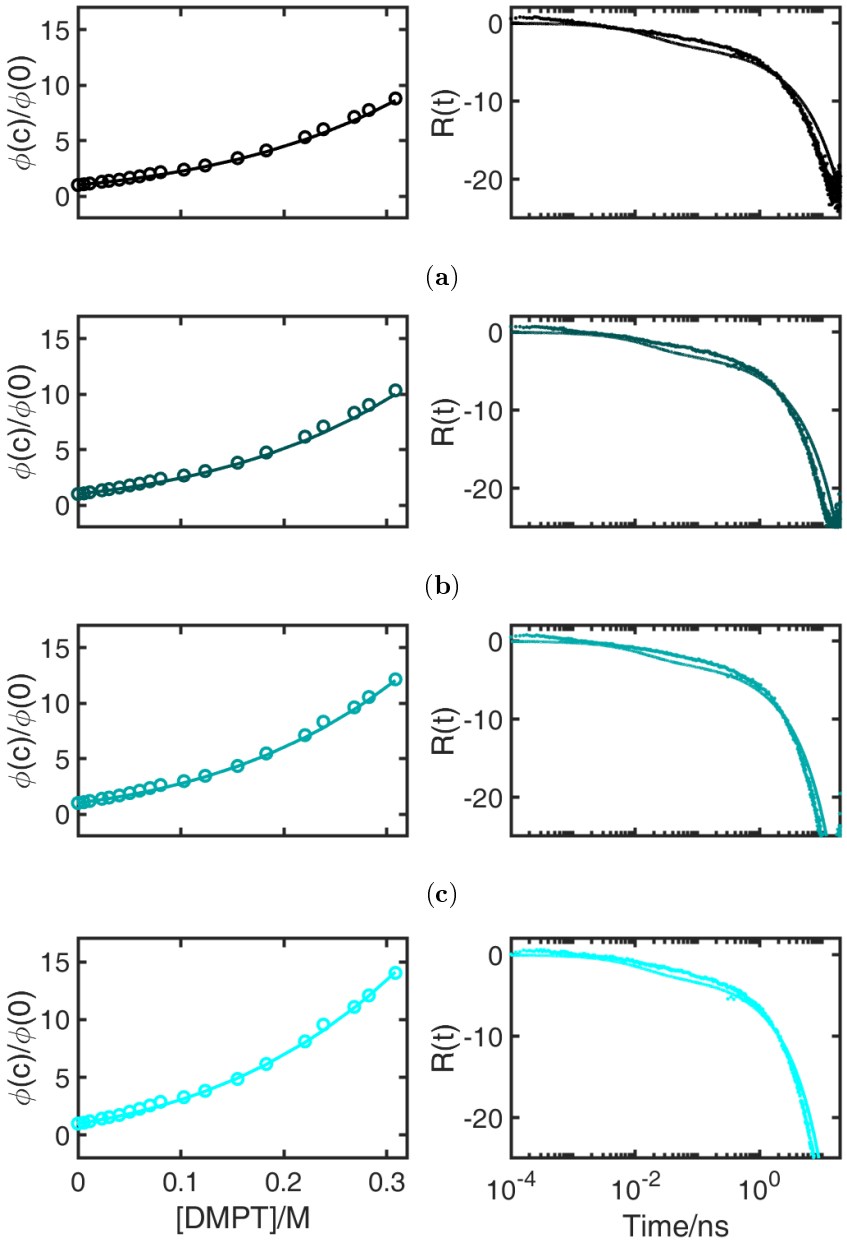

Figure B.7: Comparison between (circle) experiments and (line) calculations using (left column) SV plots and $R(t)$ functions for R6G-DMpT quenching in DG mixture ($x_1 = 0.36$) at four temperatures, increasing temperature from black to blue.

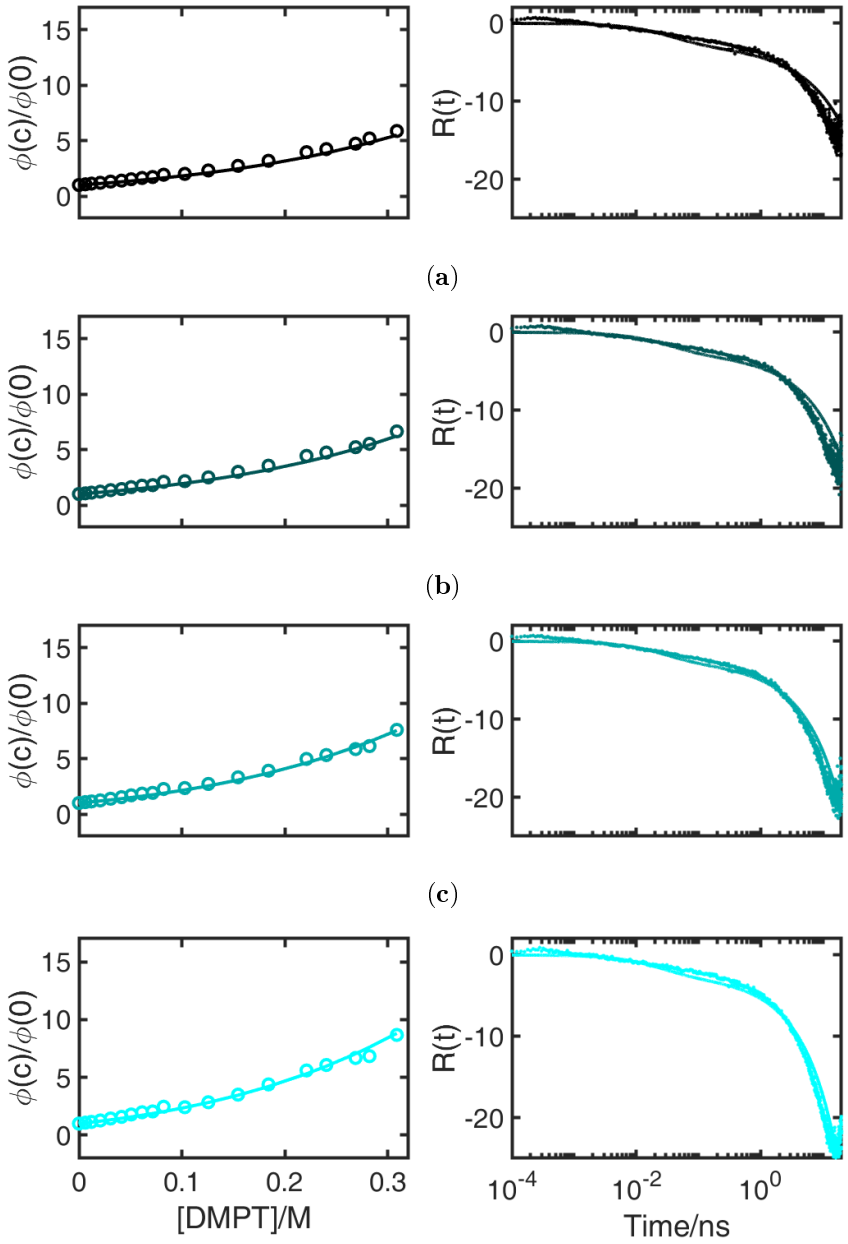

Figure B.8: Comparison between (circle) experiments and (line) calculations using (left column) SV plots and $R(t)$ functions for R6G-DMpT quenching in DG mixture ($x_1 = 0.51$) at four temperatures, increasing temperature from black to blue.

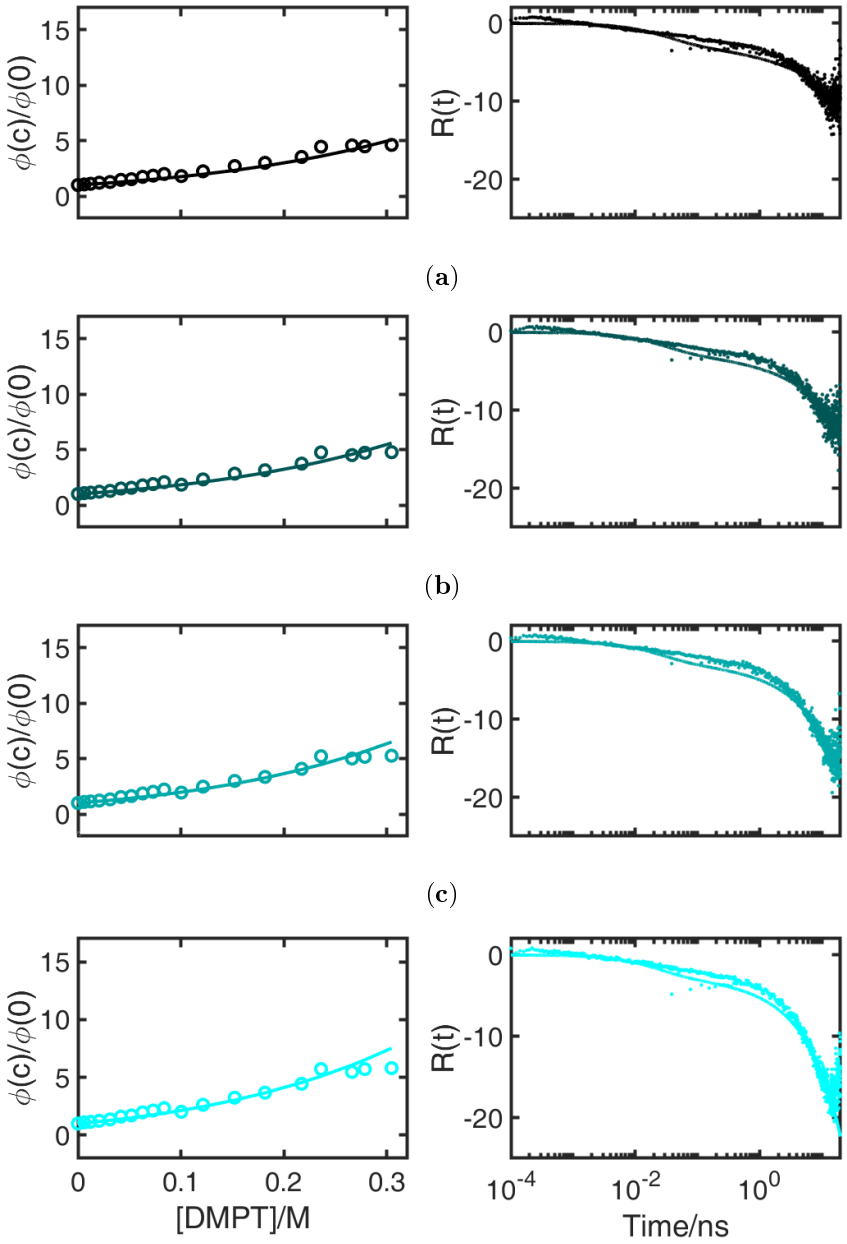

Figure B.9: Comparison between (circle) experiments and (line) calculations using (left column) SV plots and $R(t)$ functions for R6G-DMpT quenching in DG mixture ($x_1 = 0.63$) at four temperatures, increasing temperature from black to blue.

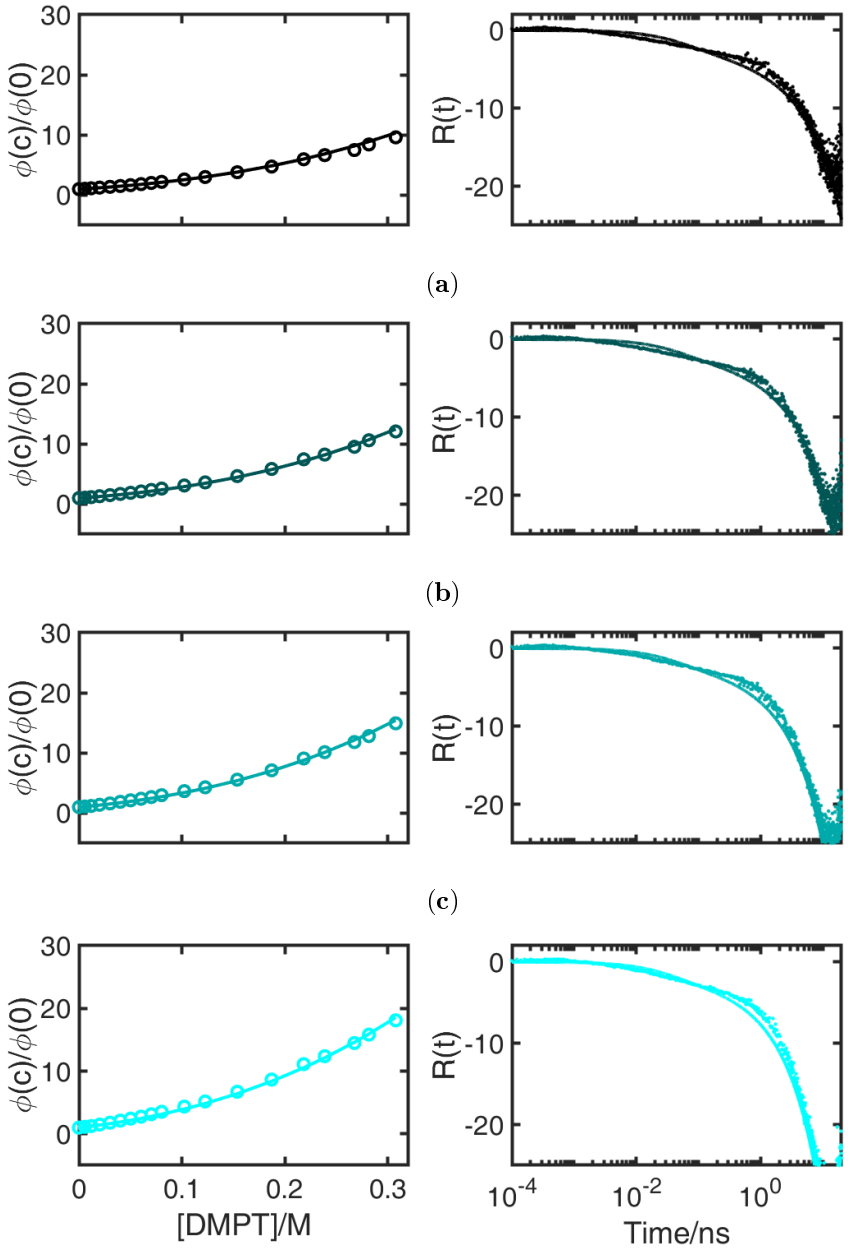

Figure B.10: Comparison between (circle) experiments and (line) calculations using (left column) SV plots and $R(t)$ functions for Pe-DMpT quenching in DG mixture ($x_1 = 0.36$) at four temperatures, increasing temperature from black to blue.

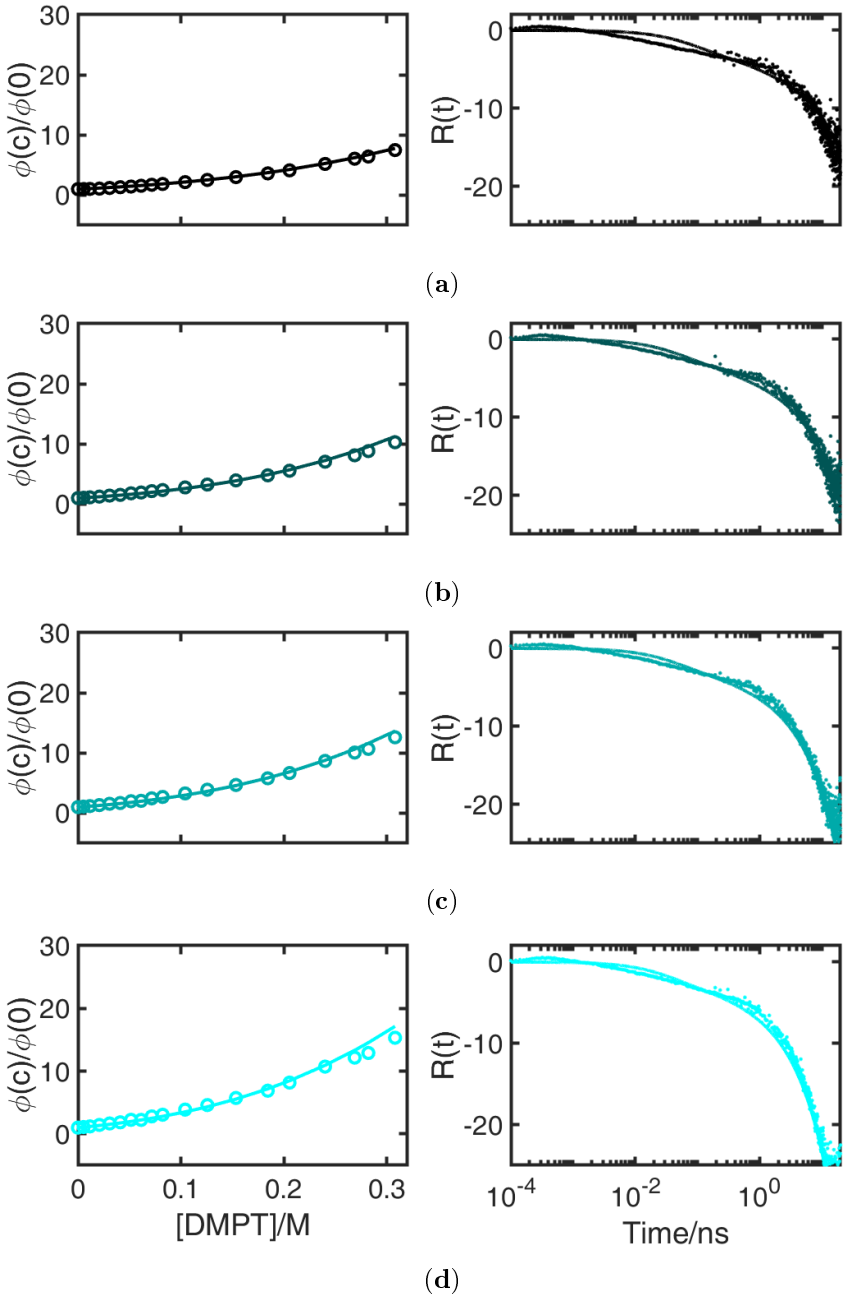

Figure B.11: Comparison between (circle) experiments and (line) calculations using (left column) SV plots and $R(t)$ functions for Pe-DMpT quenching in DG mixture ($x_1 = 0.52$) at four temperatures, increasing temperature from black to blue.

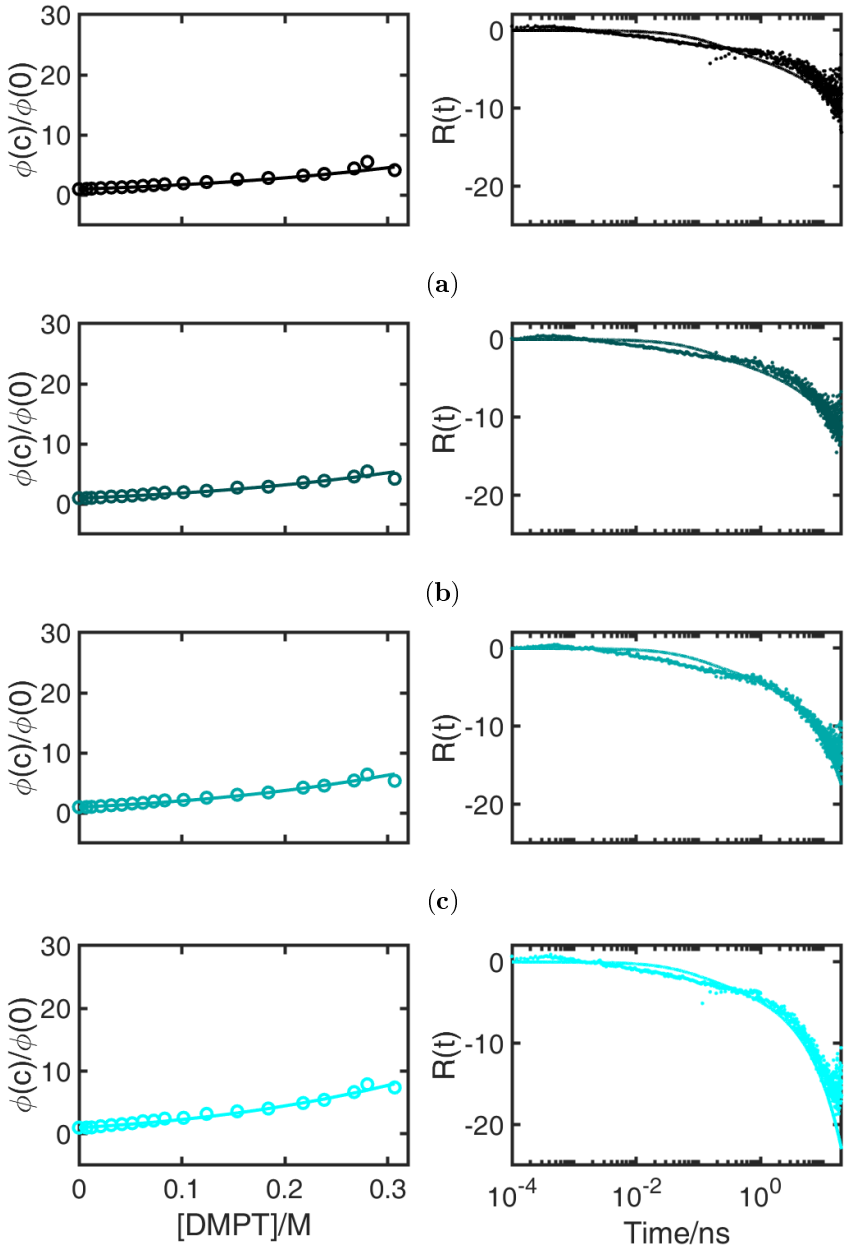

Figure B.12: Comparison between (circle) experiments and (line) calculations using (left column) SV plots and $R(t)$ functions for Pe-DMpT quenching in DG mixture ($x_1 = 0.64$) at four temperatures, increasing temperature from black to blue.

Bibliography

[1] K. Shobatake, Y. T. Lee, and S. A. Rice. Reactions of f atoms and aromatic and heterocyclic molecules: Energy distribution in the reaction complex. *The Journal of Chemical Physics*, 59(3):1435–1448, 1973.

[2] S. K. Gray, S. A. Rice, and M. J Davis. Bottlenecks to unimolecular reactions and an alternative form for classical rrkm theory. *The Journal of Physical Chemistry*, 90(16):3470–3482, 1986.

[3] F. H. Constable. Surface adsorption and the velocity of chemical action at gas-solid interfaces. *Mathematical Proceedings of the Cambridge Philosophical Society*, 23(5):593–606, 1927.

[4] F. H. Constable and W. J. Pope. The mechanism of catalytic decomposition. *Proceedings of the Royal Society of London. Series A, Containing Papers of a Mathematical and Physical Character*, 108(746):355–378, 1925.

[5] E. Rabinowitch and W. C. Wood. The collison mechanism and the primary photochemical process in solutions. *Trans. Faraday Soc.*, 32:1381–1387, 1936.

[6] J. Kolm, A. Engdahl, O. Schrems, and B. Nelander. A spectroscopic and photoisomerisation study of bromine dioxides in argon matrices. *Chemical Physics*, 214(2):313–319, 1997.

[7] M. E. Jacox. The reaction of F atoms with methane in an argon matrix. *Chemical Physics*, 42:133 – 148, 1979.

[8] T. Rosenberg and W. Wilbrandt. The kinetics of membrane transports involving chemical reactions. *Experimental Cell Research*, 9(1):49 – 67, 1955.

[9] J Gutknecht and D. C. Tosteson. Diffusion of weak acids across lipid bilayer membranes: Effects of chemical reactions in the unstirred layers. *Science*, 182(4118):1258–1261, 1973.

[10] G. P. Wiederrecht, B. A. Yoon, and M. R. Wasielewski. High Photorefractive Gain in Nematic Liquid Crystals Doped with Electron Donor and Acceptor Molecules. *Science*, 270(5243):1794–1797, 1995.

[11] S. Soh, M. Byrska, K. Kandere-Grzybowska, and B. A. Grzybowski. Reaction-Diffusion Systems in Intracellular Molecular Transport and Control. *Angewandte Chemie International Edition*, 49(25):4170–4198, 2010.

[12] Bartosz A. Grzybowski. *Chemistry in Motion: Reaction-Diffusion Systems for Micro- and Nanotechnology*. John Wiley and Sons, 2009.

[13] W. J. Leigh and M. S. Workentin. Applications: Liquid Crystals as Solvents for Spectroscopic, Chemical Reaction, and Gas Chromatographic Applications. In *Handbook of Liquid Crystals*, pages 839–895. Wiley-Blackwell, 2008.

[14] Y. B. Amerik and B. A. Krentsel. Polymerization of certain vinyl monomers in liquid crystals. *Journal of Polymer Science Part C: Polymer Symposia*, 16(3):1383–1392, 2007.

[15] B. Samori and L. Fiocco. Liquid crystalline catalysis: reactivity induced by smectic solvents. *Journal of the American Chemical Society*, 104(9):2634–2636, 1982.

[16] A. Nunez, T. Hollebeek, and M. M. Labes. Chemical reactions in liquid crystalline solvents: anti-Arrhenius behavior as a consequence of nematic-smectic A-reentrant nematic phase transitions. *Journal of the American Chemical Society*, 114(12):4925–4926, 1992.

[17] P. De Maria, A. Lodi, B. Samori, F. Rustichelli, and G. Torquati. Liquid crystalline catalysis. 2. Sulfonate ester rearrangements induced in solution by the ordered structure of a smectic B solvent. *Journal of the American Chemical Society*, 106(3):653–656, 1984.

[18] C. A. Emeis and P. L. Fehder. Microscopic mechanism for diffusion and the rates of diffusion-controlled reactions in simple liquid solvents. *Journal of the American Chemical Society*, 92(8):2246–2252, 1970.

[19] W. J. Leigh, D. T. Frendo, and P. J. Klawunn. Organic reactions in liquid crystalline solvents. 1. The thermal cis–trans isomerization of a bulky olefin in cholesteric liquid crystalline solvents. *Canadian Journal of Chemistry*, 63(8):2131–2138, 1985.

[20] W. J. Leigh and D. S.. Mitchell. Organic reactions in liquid crystalline solvents. 6. Regiochemical control of bimolecular chemical reactivity in smectic and cholesteric liquid crystals. *Journal of the American Chemical Society*, 110(4):1311–1313, 1988.

[21] W. J. Leigh. Organic reactions in liquid crystalline solvents. 2. An investigation into the use of liquid crystalline solvents to effect stereochemical control in the Diels–Alder reaction. *Canadian Journal of Chemistry*, 63(10):2736–2741, 1985.

[22] M. J. Fuller and M. R. Wasielewski. Photorefractivity in Nematic Liquid Crystals Using a Donor-Acceptor Dyad with a Low-Lying Excited Singlet State for Charge Generation. *The Journal of Physical Chemistry B*, 105(30):7216–7219, 2001.

[23] G. P. Wiederrecht, B. A. Yoon, W. A. Svec, and M. R. Wasielewski. Photorefractivity in Nematic Liquid Crystals Containing Electron Donor-Acceptor Molecules That Undergo Intramolecular Charge Separation. *Journal of the American Chemical Society*, 119(14):3358–3364, 1997.

[24] G. P. Wiederrecht, W. A. Svec, and M. R. Wasielewski. Differential Control of Intramolecular Charge Separation and Recombination Rates Using Nematic Liquid Crystal Solvents. *Journal of the American Chemical Society*, 119(26):6199–6200, 1997.

[25] L. E. Sinks and M. R. Wasielewski. Effects of Solvent and Structural Dynamics on Electron Transfer Reactions of 4-Aminonaphthalene-1,8-dicarboximide Donor-Acceptor Molecules in Nematic Liquid Crystals and Isotropic Solvents. *The Journal of Physical Chemistry A*, 107(5):611–620, 2003.

[26] L. Sinks, M. J. Fuller, W. Liu, M. J. Ahrens, and M. R. Wasielewski. Photoinduced electron transfer in a donor–acceptor dyad oriented by an aligned nematic liquid crystal solvent. *Chemical Physics*, 319(1):226–234, 2005.

[27] M. S. Zakerhamidi, M. Moghadam, A. Ghanadzadeh, and S. Hosseini. Anisotropic and isotropic solvent effects on the dipole moment and photophysical properties of rhodamine dyes. *Journal of Luminescence*, 132:931–937, 2012.

[28] M. S. Zakerhamidi, M. Keshavarz, H. Tajalli, A. Ghanadzadeh, S. Ahmadi, M. Moghadam, S. H. Hosseini, and V. Hooshangi. Isotropic and anisotropic environment effects on the UV/vis absorption spectra of three disperse azo dyes. *Journal of Molecular Liquids*, 154:94–101, 2010.

[29] M. Bixon and J. Jortner. Electron transfer—from isolated molecules to biomolecules. *Advances in Chemical Physics: Electron Transfer—from Isolated Molecules to Biomolecules. Part 1*, 106:35–202, 1999.

[30] Vincenzo Balzani. *Electron transfer in chemistry*. Vch Verlagsgesellschaft Mbh, 2001.

[31] K. Dahl, R. Biswas, N. Ito, and M. Maroncelli. Solvent dependence of the spectra and kinetics of excited-state charge transfer in three (alkylamino)benzonitriles. *The Journal of Physical Chemistry B*, 109(4):1563–1585, 2005.

[32] A. Rosspeintner, G. Angulo, and E. Vauthey. Bimolecular photoinduced electron transfer beyond the diffusion limit: The rehm–weller experiment revisited with femtosecond time resolution. *Journal of the American Chemical Society*, 136(5):2026–2032, 2014.

[33] K. L. Ivanov, N. N. Lukzen, A. B. Doktorov, and A. I. Burshtein. Integral encounter theories of multistage reactions. i. kinetic equations. *The Journal of Chemical Physics*, 114(4):1754–1762, 2001.

[34] M. v Smoluchowski. Versuch einer mathematischen theorie der koagulationskinetik kolloider lösungen. *Zeitschrift für physikalische Chemie*, 92(1):129–168, 1918.

[35] S.A. Rice. *Diffusion-Limited Reactions*. ISSN. Elsevier Science, 1985.

[36] A. I. Burshtein. *Non-Markovian Theories of Transfer Reactions in Luminescence and Chemiluminescence and Photo- and Electrochemistry*, chapter 3, pages 105–418. John Wiley and Sons, Ltd, 2004.

[37] G. Wilemski and M. Fixman. General theory of diffusion-controlled reactions. *The Journal of Chemical Physics*, 58(9):4009–4019, 1973.

[38] K. Lindenberg, R. Metzler, and G. Oshanin. *Chemical Kinetics: Beyond The Textbook*. World Scientific Publishing Company, 2019.

[39] H. L. Friedman. A hydrodynamic effect in the rates of diffusion-controlled reactions1. *The Journal of Physical Chemistry*, 70(12):3931–3933, 1966.

[40] J. M. Deutch and B. U. Felderhof. Hydrodynamic effect in diffusion-controlled reaction. *The Journal of Chemical Physics*, 59(4):1669–1671, 1973.

[41] S. H. Northrup and J. T. Hynes. Short range caging effects for reactions in solution. i. reaction rate constants and short range caging picture. *The Journal of Chemical Physics*, 71(2):871–883, 1979.

[42] A. G. Chmielewski. Viscosity Coefficients of Some Nematic Liquid Crystals. *Molecular Crystals and Liquid Crystals*, 132(3-4):339–352, 1986.

[43] J. Jadżyn, R. Dabrowski, T. Lech, and G. Czechowski. Viscosity of the homologous series of n-alkylcyanobiphenyls. *Journal of Chemical & Engineering Data*, 46(1):110–112, 2001.

[44] L. Léger and A. Martinet. VISCOSITY MEASUREMENTS IN THE NEMATIC AND SMECTIC A PHASES OF A LIQUID CRYSTAL CRITICAL BEHAVIOUR. *Le Journal de Physique Colloques*, 37:C3–89–C3–97, 1976.

[45] S. F. Swallen, Kristin Weidemaier, H. L. Tavernier, and M. D. Fayer. Experimental and Theoretical Analysis of Photoinduced Electron Transfer: Including the Role of Liquid Structure. *The Journal of Physical Chemistry*, 100:8106–8117, 1996.

[46] D. A. Dunmur, M. R. Manterfield, W. H. Miller, and J. K. Dunleavy. The dielectric and optical properties of the homologous series of cyanoalkyl-biphenyl liquid crystals. *Molecular Crystals and Liquid Crystals*, 45(1-2):127–144, 1978.

[47] F.W. Deeg and M.D. Fayer. Dynamics in the pretransitional isotropic phase of pentylcyanobiphenyl studied with subpicosecond transient grating experiments. *Chemical Physics Letters*, 167(6):527 – 534, 1990.

[48] A. Bogi and S. Faetti. Elastic, dielectric and optical constants of 4'-pentyl-4-cyanobiphenyl. *Liquid Crystals*, 28(5):729–739, 2001.

[49] M. Lilichenko and D. V. Matyushov. Reorganization energy of intermolecular electron transfer in solvents near isotropic/nematic transition. *The Journal of Chemical Physics*, 119(3):1559–1568, 2003.

[50] V. Kapko and D. V. Matyushov. Dynamical arrest of electron transfer in liquid crystalline solvents. *The Journal of Physical Chemistry B*, 110(26):13184–13194, 2006.

[51] F. Jones and T. J. Reeve. Orientation of dyes in liquid crystalline media. *Journal of the Society of Dyers and Colourists*, 95(10):352–359, 1979.

[52] M. G. Pellatt, I. H. C. Roe, and J. Constant. Photostable anthraquinone pleochroic dyes. *Molecular Crystals and Liquid Crystals*, 59(3-4):299–316, 1980.

[53] G. P. Wiederrecht, W. A. Svec, and M. R. Wasielewski. Controlling the Adiabaticity of Electron-Transfer Reactions Using Nematic Liquid-Crystal Solvents. *The Journal of Physical Chemistry B*, 103:1386–1389, 1999.

[54] M. Smoluchowski. The kinetic theory of brownian molecular motion and suspensions. *Annalen der Physik*, 21:756–780, 1906.

[55] A. Einstein. Über die von der molekularkinetischen theorie der wärme geforderte bewegung von in ruhenden flüssigkeiten suspendierten teilchen. *Annalen der Physik*, 322(8):549–560, 1905.

[56] P. Langevin. Sur la théorie du mouvement brownien. *Comptes Rendus de l'Academie des Sciences (Paris)*, 146:530–533, 1908.

[57] T. Förster. Zwischenmolekulare Energiewanderung und Fluoreszenz. *Annalen der Physik*, 437:55–75, 1948.

[58] I. Z. Steinberg and E. Katchalski. Theoretical analysis of the role of diffusion in chemical reactions, fluorescence quenching, and nonradiative energy transfer. *The Journal of Chemical Physics*, 48(6):2404–2410, 1968.

[59] K. Seki, M. Wojcik, and M. Tachiya. Diffusion-mediated geminate reactions under excluded volume interactions. *Physical Review E*, 85:011131, 2012.

[60] K. Lindenberg, R. Metzler, and G. Oshanin. *Chemical Kinetics: Beyond the Textbook*. World scientific, 2019.

[61] R. Zwanzig. Dielectric Friction on a Moving Ion. II. Revised Theory. *The Journal of Chemical Physics*, 52, 1970.

[62] A. Spernol and K. Wirtz. Zur Mikroreibung in Flússigkeiten. *Zeitschrift fúr Naturforschung A*, 8:522–532, 1953.

[63] P. Debye. *Polar molecules*. Chemical Catalog Company, Incorporated, 1929.

[64] B. Valeur and M. N. Berberan-Santos. *Molecular Fluorescence: Principles and Applications*. John Wiley and Sons, May 2012.

[65] R. A. Marcus. On the theory of oxidation-reduction reactions involving electron transfer. i. *The Journal of Chemical Physics*, 24(5):966–978, 1956.

[66] R. A. Marcus and N. Sutin. Electron transfers in chemistry and biology. *Biochimica et Biophysica Acta (BBA) - Reviews on Bioenergetics*, 811:265–322, 1985.

[67] A. Weller. Mechanism and Spindynamics of Photoinduced Electron Transfer Reactions. *Zeitschrift für physikalische Chemie*, 130(2):129–138, 1982.

[68] S. Pekar. Local quantum states of electrons in an ideal ion crystal. *Zhurnal Eksperimentalnoi I Teoreticheskoi Fiziki*, 16(4):341–348, 1946.

[69] M. Dinpajooh, M. D. Newton, and D. V. Matyushov. Free energy functionals for polarization fluctuations: Pekar factor revisited. *The Journal of Chemical Physics*, 146(6):064504, 2017.

[70] L. D. Zusman. Outer-sphere electron transfer in polar solvents. *Chemical Physics*, 49:295–304, 1980.

[71] M. D. Newton and N. Sutin. Electron transfer reactions in condensed phases. *Annual Review of Physical Chemistry*, 35(1):437–480, 1984.

[72] I. R. Gould, R. H. Young, R. E. Moody, and S. Farid. Contact and solvent-separated geminate radical ion pairs in electron-transfer photochemistry. *The Journal of Physical Chemistry*, 95(5):2068–2080, 1991.

[73] G. Angulo, A. Rosspeintner, B. Lang, and E. Vauthey. Optical transient absorption experiments reveal the failure of formal kinetics in diffusion assisted electron transfer reactions. *Phys. Chem. Chem. Phys.*, 20:25531–25546, 2018.

[74] G. Angulo, M. Brucka, M. Gerecke, G. Grampp, D. Jeannerat, J. Milkiewicz, Y. Mitrev, C. Radzewicz, A. Rosspeintner, E. Vauthey, and P. Wnuk. Characterization of dimethylsulfoxide/glycerol mixtures: a binary solvent system for the study of "friction-dependent" chemical reactivity. *Physical Chemistry Chemical Physics*, 18(27):18460–18469, 2016.

[75] H. A. Kramers. Brownian motion in a field of force and the diffusion model of chemical reactions. *Physica*, 7:284–304, 1940.

[76] A. V. Barzykin, P. A. Frantsuzov, K. Seki, and M. Tachiya. *Solvent Effects in Nonadiabatic Electron-Transfer Reactions: Theoretical Aspects*, chapter 9, pages 511–616. John Wiley and Sons, Ltd, 2003.

[77] H. Sumi and R. A. Marcus. Dynamical effects in electron transfer reactions. *The Journal of Chemical Physics*, 84:4894–4914, 1986.

[78] S. Thallmair, M. Kowalewski, J. P. P. Zauleck, M. K. Roos, and R. de Vivie-Riedle. Quantum dynamics of a photochemical bond cleavage influenced by the solvent environment: A dynamic continuum approach. *The Journal of Physical Chemistry Letters*, 5(20):3480–3485, 2014.

[79] R. F. Grote and J. T. Hynes. The stable states picture of chemical reactions. ii. rate constants for condensed and gas phase reaction models. *The Journal of Chemical Physics*, 73(6):2715–2732, 1980.

[80] A. Nitzan. *Chemical Dynamics in Condensed Phases: Relaxation, Transfer and Reactions in Condensed Molecular Systems*. OUP Oxford, 2006.

[81] M. Maroncelli and G. R. Fleming. Picosecond solvation dynamics of coumarin 153: The importance of molecular aspects of solvation. *The Journal of Chemical Physics*, 86(11):6221–6239, 1987.

[82] A. Rosspeintner, G. Angulo, C. Onitsch, M. Kivala, F. Diederich, G. Grampp, and G. Gescheidt. Photophysics of two prototypical molecular-wire building blocks: Solvent-induced conformational dynamics? *ChemPhysChem*, 11(8):1700–1710, 2010.

[83] V. Karunakaran, M. Pfaffe, I. Ioffe, T. Senyushkina, S. A. Kovalenko, R. Mahrwald, V. Fartzdinov, H. Sklenar, and N. P. Ernsting. Solvation oscillations and excited-state dynamics of 2-amino- and 2-hydroxy-7-nitrofluorene and its 2'-deoxyriboside. *The Journal of Physical Chemistry A*, 112(18):4294–4307, 2008.

[84] K. Tominaga, G. C. Walker, W. Jarzeba, and P. F. Barbara. Ultrafast charge separation in adma: experiment, simulation, and theoretical issues. *The Journal of Physical Chemistry*, 95(25):10475–10485, 1991.

[85] D. A. Cherepanov, L. I. Krishtalik, and A. Y. Mulkidjanian. Photosynthetic Electron Transfer Controlled by Protein Relaxation: Analysis by Langevin Stochastic Approach. *Biophysical Journal*, 80:1033–1049, 2001.

[86] W. Min, G. Luo, B. J. Cherayil, S. C. Kou, and X. S. Xie. Observation of a power-law memory kernel for fluctuations within a single protein molecule. *Phys. Rev. Lett.*, 94:198302, 2005.

[87] T. Jong Kang, W. Jarzeba, P. F. Barbara, and T. Fonseca. A photodynamical model for the excited state electron transfer of bianthryl and related molecules. *Chemical Physics*, 149:81–95, 1990.

[88] J. T. Hynes. Outer-sphere electron-transfer reactions and frequency-dependent friction. *The Journal of Physical Chemistry*, 90(16):3701–3706, 1986.

[89] R Kubo. The fluctuation-dissipation theorem. *Reports on Progress in Physics*, 29(1):255–284, 1966.

[90] D. Chandler. Statistical mechanics of isomerization dynamics in liquids and the transition state approximation. *The Journal of Chemical Physics*, 68(6):2959–2970, 1978.

[91] D. R. Kattnig, A. Rosspeintner, and G. Grampp. Magnetic field effects on exciplex-forming systems: the effect on the locally excited fluorophore and its dependence on free energy. *Phys. Chem. Chem. Phys.*, 13:3446–3460, 2011.

[92] G. Van der Zwan and J. T. Hynes. Time-dependent fluorescence solvent shifts, dielectric friction, and nonequilibrium solvation in polar solvents. *The Journal of Physical Chemistry*, 89(20):4181–4188, 1985.

[93] W. Liptay. Die Beeinflussung der optischen Absorption von Molekülen durch ein äußeres elektrisches Feld: III. Berücksichtigung der direkten Feldstärkeabhängigkeit des Übergangsmoments und des inneren Feldes in einer Lösung. *Zeitschrift für Naturforschung A*, 20:272–289, 1965.

[94] R. Mannella. Integration of stochastic differential equations on a computer. *International Journal of Modern Physics C*, 13(09):1177–1194, 2002.

[95] G. Angulo, J. Jedrak, A. Ochab-Marcinek, P. Pasitsuparoad, C. Radzewicz, P. Wnuk, and A. Rosspeintner. How good is the generalized langevin equation to describe the dynamics of photo-induced electron transfer in fluid solution? *The Journal of Chemical Physics*, 146(24):244505, 2017.

[96] M. L. Horng, J. A. Gardecki, A. Papazyan, and M. Maroncelli. Subpicosecond measurements of polar solvation dynamics: Coumarin 153 revisited. *The Journal of Physical Chemistry*, 99(48):17311–17337, 1995.

[97] Friedel, G. Les états mésomorphes de la matière. *Annales de Physique*, 9(18):273–474, 1922.

[98] Dunmur, D. A. and Miller, W. H. Volumetric studies of the homologous series of alkyl-cyano-biphenyl liquid crystals. *J. Phys. Colloques*, 40:C3–141–C3–146, 1979.

[99] M. K. Das and R. Paul. Determination of bend to splay elastic constant ratio (k 3 /k 1) of several nematogens and applicability of spherocylindrical model. *Molecular Crystals and Liquid Crystals Science and Technology. Section A. Molecular Crystals and Liquid Crystals*, 259(1):13–21, 1995.

[100] D. Frenkel. Computer simulation of hard-core models for liquid crystals. *Molecular Physics*, 60:1–20, 1987.

[101] C. Zannoni. On the Description of Ordering in Liquid Crystals. In *The Molecular Dynamics of Liquid Crystals*, NATO ASI Series, pages 11–40. Springer Netherlands, 1994.

[102] S. C. McGrother, D. C. Williamson, and G. Jackson. A re-examination of the phase diagram of hard spherocylinders. *The Journal of Chemical Physics*, 104(17):6755–6771, 1996.

[103] S. Hess, D. Frenkel, and M.P. Allen. On the anisotropy of diffusion in nematic liquid crystals: test of a modified affine transformation model via molecular dynamics. *Molecular Physics*, 74(4):765–774, 1991.

[104] M. P Allen, G. T Evans, D. Frenkel, and B. M. Mulder. Hard convex body fluids. *Advances in chemical physics*, 86:1–166, 1993.

[105] G. J. Krüger. Diffusion in thermotropic liquid crystals. *Physics Reports*, 82:229–269, 1982.

[106] T. Kawai, A. Kubota, K. Kawamura, H. Tsumatori, and T. Nakashima. Single molecule fluorescence autocorrelation measurement on anisotropic molecular diffusion in nematic liquid crystal. *Thin Solid Films*, 516:2666–2669, 2008.

[107] M. Pumpa and F. Cichos. Slow Single-Molecule Diffusion in Liquid Crystals. *The Journal of Physical Chemistry B*, 116:14487–14493, 2012.

[108] W. E. Schiesser and G. W. Griffiths. *A Compendium of Partial Differential Equation Models: Method of Lines Analysis with Matlab*. Cambridge University Press, 2009.

[109] K. Hasharoni and H. Levanon. Attenuation of Intramolecular Electron Transfer Rates in Liquid Crystals. *The Journal of Physical Chemistry*, 99(14):4875–4878, 1995.

[110] K. Hasharoni, H. Levanon, J. von Gersdorff, H. Kurreck, and K. Möbius. Photo-induced electron transfer in covalently linked donor–acceptor assemblies in liquid crystals. Time-resolved electron paramagnetic resonance. *The Journal of Chemical Physics*, 98:2916–2926, 1993.

[111] D. V. Matyushov. Electron transfer in nonpolar media. *Phys. Chem. Chem. Phys.*, 22:10653–10665, 2020.

[112] N. Banerji, G. Angulo, I. Barabanov, and E. Vauthey. Intramolecular charge-transfer dynamics in covalently linked perylene-dimethylaniline and cyanoperylene-dimethylaniline. *The Journal of Physical Chemistry A*, 112(40):9665–9674, 2008.

[113] M. A Gidley and D Stubley. Phase diagrams of some mixtures of (a nematic liquid crystal + an ordinary liquid). *The Journal of Chemical Thermodynamics*, 14:785–790, 1982.

[114] K. P. Sigdel and G. S. Iannacchione. Evolution of the isotropic to nematic phase transition in binary mixtures of octylcyanobiphenyl and n-hexane. *The Journal of Chemical Physics*, 133:044513, 2010.

[115] C. David and D. Baeyens-volant. Absorption and Fluorescence Spectra of 4-Cyanobiphenyl and 4'-Alkyl- or 4'-Alkoxy-Substituted Liquid Crystalline Derivatives. *Molecular Crystals and Liquid Crystals*, 59:181–196, 1980.

[116] T. Slanina and T. Oberschmid. Rhodamine 6g radical: A spectro (fluoro) electrochemical and transient spectroscopic study. *ChemCatChem*, 10(18):4182–4190, 2018.

[117] A. Wiśniewska, K. Sozański, T. Kalwarczyk, K. Kędra-Królik, C. Pieper, S. A. Wieczorek, S. Jakieła, J. Enderlein, and R. Hołyst. Scaling of activation energy for macroscopic flow in poly(ethylene glycol) solutions: Entangled – Non-entangled crossover. *Polymer*, 55:4651–4657, 2014.

[118] L. Grunberg and Alfred H. Nissan. Mixture Law for Viscosity. *Nature*, 164:799–800, 1949.

[119] S. M. Puranik, A. C. Kumbharkhane, and S. C. Mehrotra. Dielectric study of dimethyl sulfoxide–water mixtures using the time-domain technique. *J. Chem. Soc., Faraday Trans.*, 88:433–435, 1992.

[120] O. Ciocirlan and O. Iulian. Vapor pressure, density, viscosity and refractive index of dimethyl sulfoxide + 1, 4-dimethylbenzene system. *Hungarian Journal of Industry and Chemistry*, 31(1), 2003.

[121] R.J. Sengwa, V. Khatri, S. Choudhary, and S. Sankhla. Temperature dependent static dielectric constant and viscosity behaviour of glycerol–amide binary mixtures: Characterization of dominant complex structures in dielectric polarization and viscous flow processes. *Journal of Molecular Liquids*, 154(2):117 – 123, 2010.

[122] A. P. Gregory and R. N. Clarke. Tables of the complex permittivity of dielectric reference liquids at frequencies up to 5 GHz. NPL report, September 2001.

[123] P. Pacak. Polarizability and molecular radius of dimethyl-sulfoxide and dimethylformamide from refractive index data. *Journal of Solution Chemistry*, 16:71–77, 1987.

[124] L. F. Hoyt. New table of the refractive index of pure glycerol at 20°c. *Industrial & Engineering Chemistry*, 26(3):329–332, 1934.

[125] O. Redlich and A. T. Kister. Algebraic representation of thermodynamic properties and the classification of solutions. *Industrial & Engineering Chemistry*, 40(2):345–348, 1948.

[126] M. Flämig, L. Gabrielyan, R. Minikejew, S. Markarian, and E. A. Rössler. Dielectric relaxation and proton field-cycling nmr relaxometry study of dimethyl sulfoxide/glycerol mixtures down to glass-forming temperatures. *Physical Chemistry Chemical Physics*, 22:9014–9028, 2020.

[127] M. S. Wertheim. Exact solution of the percus-yevick integral equation for hard spheres. *Physical Review Letters*, 10:321–323, 1963.

[128] L. Tsang, J. A. Kong, K.-H. Ding, and C. O. Ao. *Scattering of Electromagnetic Waves, Numerical Simulations.* John Wiley and Sons, 2004.

[129] N. W. Ashcroft and David C. Langreth. Structure of binary liquid mixtures. i. *Phys. Rev.*, 156:685–692, 1967.

[130] U. Onthong, T. Megyes, I. Bakó, T. Radnai, T. Grósz, K. Hermansson, and M. Probst. X-ray and neutron diffraction studies and molecular dynamics simulations of liquid DMSO. *Physical Chemistry Chemical Physics*, 6:2136–2144, 2004.

[131] S.-T. Wu. Absorption measurements of liquid crystals in the ultraviolet, visible, and infrared. *Journal of Applied Physics*, 84(8):4462–4465, 1998.

[132] T. Bezrodna, V. Melnyk, V. Vorobjev, and G. Puchkovska. Low-temperature photoluminescence of 5CB liquid crystal. *Journal of Luminescence*, 130:1134–1141, 2010.

[133] B.a. Belyaev, N.a. Drokin, V.f. Shabanov, and V.a. Baranova. Dielectric Properties of Liquid Crystals of the Cyano Derivative Compounds with Different Fragments in the Molecular Core. *Physics of the Solid State*, 46:574–578, 2004.

[134] S. Urban, B. Gestblom, and A. Würflinger. Comparison of the Dielectric Relaxation Data for the Isotropic and Nematic Phases of Three Homologous Series: nCb, nOCB and nPCH, (n =5÷8). *Molecular Crystals and Liquid Crystals Science and Technology. Section A. Molecular Crystals and Liquid Crystals*, 331(1), 1999.

[135] A. Buka and A. H. Price. Dielectric relaxation and order parameters in the nematic and smectic phases of 4-n-octyl-4'-cyanobiphenyl (8cb). *Molecular Crystals and Liquid Crystals*, 116(3-4):187–195, 1985.

[136] M. R. Panda, S. Koley, K. Mishra, and S. Ghosh. Probing of Reorganization Dynamics within the Different Phases of Themotropic Liquid Crystals. *ChemistrySelect*, 3(5):1551–1560, 2018.

[137] P. Bolhuis and D. Frenkel. Tracing the phase boundaries of hard spherocylinders. *The Journal of Chemical Physics*, 106(2):666–687, 1997.

[138] A. Cuetos, B. Martinez-Haya, L. F. Rull, and S. Lago. Monte carlo study of liquid crystal phases of hard and soft spherocylinders. *The Journal of Chemical Physics*, 117(6):2934–2946, 2002.

[139] Birefringent Crystals in Polarized Light - Java Tutorial | Olympus Life Science.

[140] K. Artyushkova, J. E. Fulghum, and Y. Reznikov. Orientation of 5cb molecules on aligning substrates studied by angle resolved x-ray photoelectron spectroscopy. *Molecular Crystals and Liquid Crystals*, 438(1):205/[1769]–213/[1777], 2005.

[141] T. D O'Leary, J. L Badenoch, and R. Bais. Optical methods for monitoring temperature in spectrophotometric analysers. *Annals of Clinical Biochemistry*, 20(3):153–157, 1983.

[142] G. Angulo, G. Grampp, and A. Rosspeintner. Recalling the appropriate representation of electronic spectra. *Spectrochimica Acta Part A: Molecular and Biomolecular Spectroscopy*, 65:727–731, 2006.

[143] T. Martyński, E. Mykowska, and D. Bauman. Spectral properties of fluorescent dyes in nematic liquid crystals. *Journal of Molecular Structure*, 325:161–167, 1994.

[144] J. A. Gardecki and M. Maroncelli. Set of secondary emission standards for calibration of the spectral responsivity in emission spectroscopy. *Appl. Spectrosc.*, 52(9):1179–1189, 1998.

[145] *Operation Manual*. Horiba, g edition, May 2014. Part number J81014.

[146] A. Spanos. *Probability Theory and Statistical Inference: Econometric Modeling with Observational Data*. Cambridge University Press, Cambridge, 1999.

[147] O. Bräm, F. Messina, A. M. El-Zohry, A. Cannizzo, and M. Chergui. Polychromatic femtosecond fluorescence studies of metal–polypyridine complexes in solution. *Chemical Physics*, 393:51–57, 2012.

[148] P. Wnuk, G. Burdziński, M. Sliwa, M. Kijak, A. Grabowska, J. Sepioł, and J. Kubicki. From ultrafast events to equilibrium – uncovering the unusual dynamics of ESIPT reaction: the case of dually fluorescent diethyl-2,5-(dibenzoxazolyl)-hydroquinone. *Physical Chemistry Chemical Physics*, 16(6):2542–2552, 2014.

[149] M. Bardhan, P. Mandal, A. De, A. Kumar De, J. Chowdhury, and T. Ganguly. Steady-state and time-resolved spectroscopic investigations on intramolecular electron transfer processes within a synthesized methoxynaphthalene dyad by using a nematic liquid crystal medium. *Journal of Luminescence*, 130:932–940, 2010.

[150] M. Kubista, R. Sjöback, S. Eriksson, and B. Albinsson. Experimental correction for the inner-filter effect in fluorescence spectra. 119:417–419, 1994.

[151] H. Du, R.-C. A. Fuh, J. Li, L. A. Corkan, and J. S. Lindsey. Photochemcad‡: A computer-aided design and research tool in photochemistry. *Photochemistry and Photobiology*, 68(2):141–142, 1998.

[152] D. A. Hinckley, P. G. Seybold, and D. P. Borris. Solvatochromism and thermochromism of rhodamine solutions. *Spectrochimica Acta Part A: Molecular Spectroscopy*, 42:747–754, 1986.

[153] J. E. Selwyn and J. I. Steinfeld. Aggregation of equilibriums of xanthene dyes. *The Journal of Physical Chemistry*, 76(5):762–774, 1972.

[154] E. G. Baranova. Study of the association of rhodamine 6g in ethanol and glycerol solutions. *Optics and Spectroscopy*, 13:452, 1962.

[155] N. Nizamov, U. Zakhidov, and A. K. Atakhodzhaev. Temperature-dependence of electron-spectra of rhodamine c and 6g in strong bases. *IZVESTIYA AKADEMII NAUK SSSR SERIYA FIZICHESKAYA*, 42(3):579–583, 1978.

[156] I. Renge. Refractive index dependence of solvatochromism. *Journal of Photochemistry and Photobiology A: Chemistry*, 353:433–444, 2018.

[157] Q.-H. Xu, G. D. Scholes, M. Yang, and G. R. Fleming. Probing Solvation and Reaction Coordinates of Ultrafast Photoinduced Electron-Transfer Reactions Using Nonlinear Spectroscopies: Rhodamine 6G in Electron-Donating Solvents. *The Journal of Physical Chemistry A*, 103(49):10348–10358, 1999.

[158] M. Montalti, A. Credi, L. Prodi, and M.T. Gandolfi. *Handbook of Photochemistry*. CRC Press, 2006.

[159] N. Matsuda, T. Kakitani, T. Denda, and N. Mataga. Examination of the viability of the Collins-Kimball model and numerical calculation of the time-dependent energy gap law of photoinduced charge separation in polar solution. *Chemical Physics*, 190:83 – 95, 1995.

[160] D. W. Small, D. V. Matyushov, and G. A. Voth. The theory of electron transfer reactions: What may be missing? *Journal of the American Chemical Society*, 125(24):7470–7478, 2003.

[161] D. V. Matyushov. Solvent reorganization energy of electron-transfer reactions in polar solvents. *The Journal of Chemical Physics*, 120(16):7532–7556, 2004.

[162] A. Rosspeintner, D.-R. Kattnig, G. Angulo, S. Landgraf, G. Grampp, and A. Cuetos. On the coherent description of diffusion-influenced fluorescence quenching experiments. *Chemistry – A European Journal*, 13(22):6474–6483, 2007.

[163] G. Angulo, D.-R. Kattnig, A. Rosspeintner, G. Grampp, and E. Vauthey. On the Coherent Description of Diffusion-Influenced Fluorescence Quenching Experiments-II: Early Events. *Chemistry – A European Journal*, 16(7), 2010.

[164] H. L. Tavernier and M. D. Fayer. Solute–solute spatial distribution in hydrogen bonding liquids probed with time-dependent intermolecular electron transfer. *The Journal of Chemical Physics*, 114(10):4552–4564, 2001.

[165] V. O. Saik, A. A. Goun, and M. D. Fayer. Photoinduced electron transfer and geminate recombination for photoexcited acceptors in a pure donor solvent. *The Journal of Chemical Physics*, 120(20):9601–9611, 2004.

[166] D. Frenkel, H. N. W. Lekkerkerker, and A. Stroobants. Thermodynamic stability of a smectic phase in a system of hard rods. *Nature*, 332:822–823, 1988.

[167] M. S. Zakerhamidi, M. Moghadam, A. Ghanadzadeh, and S. Hosseini. Anisotropic and isotropic solvent effects on the dipole moment and photophysical properties of rhodamine dyes. *Journal of Luminescence*, 132:931–937, 2012.

[168] T. Shim, S. Kim, D. Kim, and M. Oh-e. Fluorescence enhancement of dye-doped liquid crystal by dye-induced alignment effect. *Journal of Applied Physics*, 110:063532, 2011.

[169] B.A. Belyaev, N.A. Drokin, V.F. Shabanov, and V.A. Baranova. Dielectric Properties of Liquid Crystals of the Cyano Derivative Compounds with Different Fragments in the Molecular Core. *Physics of the Solid State*, 46(3):574–578, 2004.

[170] S. V. Dvinskikh, I. Furó, H. Zimmermann, and A. Maliniak. Anisotropic self-diffusion in thermotropic liquid crystals studied by ^{1}H and ^{2}H pulse-field-gradient spin-echo NMR. *Physical Review E*, 65(6):061701, 2002.

[171] J. Crank and E.P.J. Crank. *The Mathematics of Diffusion*. Oxford science publications. Clarendon Press, 1979.

[172] E. B. Watson, K. H. Wanser, and K. A. Farley. Anisotropic diffusion in a finite cylinder, with geochemical applications. *Geochimica et Cosmochimica Acta*, 74(2):614–633, 2010.

[173] Hilding S. and George V. A simple finite-difference grid with non-constant intervals. *Tellus*, 22(1):26–31, 1970.

[174] V. S. Gladkikh, A. I. Burshtein, H. L. Tavernier, and M. D. Fayer. Influence of diffusion on the kinetics of donor-acceptor electron transfer

monitored by the quenching of donor fluorescence. *The Journal of Physical Chemistry A*, 106(30):6982–6990, 2002.

[175] J. Jover, A. J. Haslam, A. Galindo, G. Jackson, and E. A. Muller. Pseudo hard-sphere potential for use in continuous molecular-dynamics simulation of spherical and chain molecules. *The Journal of Chemical Physics*, 137(14):144505, 2012.

[176] N. Basturk, J. Cognard, and T. Hieu Phan. Ester-substituted anthraquinone dyes soluble in nematic liquid crystal mixtures. *Molecular Crystals and Liquid Crystals*, 95(1-2):71–89, 1983.